THESIS FOR THE DEGREE OF DOCTOR OF PHILOSOPHY

Solids Flow Characterization in Bubbling Fluidized Beds with Induced Horizontal Circulation

MUNAVARA FARHA

Department of Space, Earth, and Environment

CHALMERS UNIVERSITY OF TECHNOLOGY

Gothenburg, Sweden 2025

Solids Flow Characterization in Bubbling Fluidized Beds with Induced Horizontal Circulation

MUNAVARA FARHA

ISBN 978-91-8103-344-1

Doktorsavhandlingar vid Chalmers tekniska högskola

Ny serie nr 5801

ISSN 0346-718X

DOI: https://doi.org/10.63959/chalmers.dt/5801

Department of Space, Earth and Environment

Division of Energy Technology

Chalmers University of Technology

SE-412 96 Gothenburg

Sweden

Cover:

Schematic and CFD simulation result illustrating solids crossflow in a bubbling fluidized bed with induced horizontal circulation. Upper left: cutaway of an industrial fluidized bed boiler (figure used with permission from Bioshare AB); experiments were performed in a fluid-dynamically downscaled model. Upper right: zoomed region where the solids crossflow is established and analyzed. Lower panel: CFD simulation showing flow structure in the analysis region, with parula streamlines for bulk-phase solids and red trajectories for lean-phase solids.

Printed by Chalmers Digitaltryck

Gothenburg, Sweden 2025

''The arrival time of a space probe traveling to Saturn can be predicted more accurately than the behavior of a fluidized bed chemical reactor!''

- Geldart, 1986

Abstract

Bubbling fluidized beds with horizontal solids crossflow can be broadly grouped according to function: 1) those designed for solids looping, as in indirect pyrolysis or gasification, and chemical or calcium looping; and 2) those employed in high-throughput solids processing, such as drying, iron ore reduction, and pharmaceutical manufacturing. Despite their widespread industrial application and the growing demand for their use in new process designs, there remains a lack of a detailed understanding of the flow characteristics in fluidized beds with horizontal solids throughput. This knowledge gap represents a major challenge for optimizing reactor design and advancing industrial implementation.

This thesis aims to develop a mechanistic understanding of how forced horizontal convection of solids in a bubbling fluidized bed influences the solids flow characteristics. The main research objectives are to: (i) assess experimental methods for quantifying the solids circulation rate; (ii) evaluate the efficiencies of different mechanisms to induce horizontal convection of solids; (iii) characterize bed solids transport—specifically, the interrelated effects of solids convection and dispersion—and the resulting fluidization quality; (iv) investigate how the solids crossflow influences overall flow structures; (v) examine the influences of frictional losses on bed solids flow, including the rheological properties of the dense suspension; and (vi) explore how the solids crossflow affects the mixing of a secondary solids phase consisting of large, light particles.

Experiments were conducted in a cold-flow model that comprised a closed-loop system in which solids were circulated horizontally via a solids-conveying module. The apparatus was designed and operated according to Glicksman's simplified scaling laws. In this cold model, fine bronze particles are fluidized with ambient air to fluid-dynamically resemble conditions representative of industrial-scale thermochemical fuel conversion applications. The industrial unit being modeled features a bed channel with a cross-sectional width of 0.92 m and a transport loop length of 10.35 m, in which coarse, sand-like (Geldart B-type) particles are fluidized with flue gas at approximately 800°C.

Four measurement methods for quantifying solids circulation were evaluated—namely, integral mass accumulation, differential mass accumulation, thermal tracing, and magnetic solids tracing—with the latter proving to be the most precise and robust. Using this method, five solids-conveying configurations based on different fluid-dynamical mechanisms were tested: (a) free solids splashing, which relies on bubble bursts to eject particles; (b) confined solids splashing, whereby turbulent fluidization creates particle transport that is dominated by eddies and bubble buoyancy; (c) slugging, whereby gas slugs drive particle movement in vertical ducts; (d) solids entrainment, which is achieved by elutriation at high gas velocities; and (e) directed gas injection, which imparts lateral momentum through angled nozzles. Conveying solids under a controlled bubbling fluidization regime was found to be the most efficient configuration for promoting horizontal transport of solids in the system.

The horizontal solids flow established in the channel was evaluated under various operational conditions using a combination of experimental and modeling approaches, ranging from

reduced-order descriptions to Eulerian–Eulerian computational fluid dynamics (CFD) simulations. A positive linear relationship was observed between the solids dispersion coefficient and the mean solids velocity, both evaluated in the streamwise direction. This was further explained by the CFD simulations, which indicated that at low crossflow rates, the solids flow organizes into coherent, counter-rotating vortices along the bubble paths. In contrast, at high crossflow rates, these structures are disrupted, resulting in less streamlined (stronger mixing) and more elongated (longer characteristic lengths) flow patterns. In addition, microscale dispersion was found to be dominated by bubble- and eddy-induced mixing, rather than by random particle motion or collisions. Rheological analysis revealed that the bed exhibits shear-thinning behavior and that single-phase models for non-circular open-flow channels underestimate the influence of geometry on gas-solids flows.

Analysis of the transport behavior of large, light particles added to the bed as a lean phase showed that, similar to bulk solids, a positive correlation exists between dispersion and convection, with sensitivity strongly dependent on the degree of fluidization. The dispersion of the lean particles was greater than that of the bulk solids; it remained at a similar level for both low and high fluidization velocities. However, compared to the bulk solids, the lean particles were transported at lower convection velocities under high fluidization levels. In contrast, at low fluidization levels, the particles formed a layer above the dense bed and were conveyed in a plug-like manner, exhibiting much higher horizontal velocities than the bulk solids.

Keywords: Bubbling fluidized bed, Solids mixing, Solids convection, Magnetic solids tracing, Frictional loss, Eulerian-Eulerian model, Lagrangian particle tracking

List of publications

The thesis is based on the following appended papers, which are referred to in the text by their assigned Roman numerals:

I. Farha, M., Guío-Pérez, D. C., Aronsson, J., Johnsson, F., & Pallarès, D. (2023). Assessment of experimental methods for measurements of the horizontal flow of fluidized solids under bubbling conditions. *Fuel*, *348*, *128515*. https://doi.org/10.1016/j.fuel.2023.128515

II. Farha, M., Guío-Pérez, D. C., Johnsson, F., & Pallarès, D. (2025). Comparison of solids conveying mechanisms in fluidized bed systems – Alternatives to riser. *Chemical Engineering Science*, *317*, 122000. https://doi.org/10.1016/j.ces.2025.122000

III. Farha, M., Guío-Pérez, D. C., Johnsson, F., & Pallarès, D. (2024). Characterization of the solids crossflow in a bubbling fluidized bed. *Powder Technology*, *443*, *119967*. https://doi.org/10.1016/j.powtec.2024.119967

IV. Farha, M., Ström, H., Guío-Pérez, D. C., & Pallarès, D. (2025). Spatially-resolved characterization of the flow structure in a bubbling fluidized bed with solids crossflow. Submitted for publication.

V. Farha, M., Guío-Pérez, D. C., Johnsson, F., & Pallarès, D. (2025). Frictional losses in a bubbling fluidized bed with horizontal flow of solids. *International Journal of Multiphase Flow*, *189*, 105192. https://doi.org/10.1016/j.ijmultiphaseflow.2025.105192

Author contributions:

Munavara Farha is the principal researcher for all the papers. Research Specialist Diana Carolina Guío-Pérez contributed to the discussion and review of **Papers I–V**, providing guidance on the setup of the experimental apparatus. Professor David Pallarès contributed to the discussion and review of **Papers I–V**, providing guidance with the modelling techniques used in the work. Professor Henrik Ström contributed to the discussion and review of **Paper IV**, providing guidance on the CFD model used. Professor Filip Johnsson contributed to the discussion and review of **Papers I–III and Paper V**. Jesper Aronsson contributed to the discussion of **Paper I**.

Conference contributions:

- Farha, M., Guío-Pérez, D. C., Aronsson, J., Pallarès, D., & Johnsson, F. (2022). Comparison of two measurement methods of horizontal solids flow in a bubbling fluidized bed.
  24th International Conference on Fluidized Bed Conversion (Gothenburg, Sweden).
- Farha, M., Guío-Pérez, D. C., Johnsson, F., & Pallarès, D. (2023). Analysis of Horizontal Solids Convection and Dispersion in Fluidized Beds.
  Fluidization XVII (Edinburgh, UK).
- Farha, M., Guío-Pérez, D. C., Nimvari, M. I., Pallarès, D., & Johnsson, F. (2023). Bed-Wall Frictional Loss in a Bubbling Bed with Horizontal Flow of Solids.
  Fluidization XVII (Edinburgh, UK).
- Farha, M., Guío-Pérez, D. C., Johnsson, F., & Pallarès, D. (2023). Investigation on Conveying Mechanisms for Forcing Solids Horizontal Circulation Under Bubbling Fluidized Bed Conditions.
  Fluidization XVII (Edinburgh, UK).
- Farha, M., Guío-Pérez, D. C., & Pallarès, D. (2025). Comparison of solids conveying mechanisms in fluidized-bed systems – alternatives to riser.
  90th Meeting of the IEA Technology Collaboration Program on Fluidized Bed Conversion (Nanjing, China).
- Farha, M., Guío-Pérez, D. C., Ström, H., & Pallarès, D. (2025). Numerical study of fluid-dynamics in a bubbling fluidized bed with solids crossflow.
  25th International Conference on Fluidized Bed Conversion (Nanjing, China).

Acknowledgements

This PhD journey has been both incredibly fun and deeply challenging. Time truly flies when you're having fun, and yet, here I am, writing this after five amazing years that somehow felt both endless and fleeting.

First and foremost, I owe my deepest gratitude to my supervisors, David and Carolina. Both of you have been instrumental in shaping not just my development as a researcher, but also as a person. David, thank you for giving me the chance to join the Fluidization Group. When I started, it felt like a whole new world, but your support and encouragement quickly made it feel like home. Carolina, my mentor, thank you for teaching me the art of patience and showing me what it means to be a true superwoman! Even after five years, it's still a mystery to me how you manage to do ten things at once. Your guidance has been invaluable, and I couldn't have asked for a better team of supervisors. I am truly grateful.

Henrik, even though you joined during the final year of my PhD, I have learned so much from you. The world of CFD was completely new to me, but your patience and clarity in explaining things made a huge difference. Thank you for that.

Thank you to Filip, my examiner, for your valuable feedback, even at the last moment, which brought fresh perspectives to my work. I appreciate your insights.

A special thanks to Rustan. Without your constant support in the lab, half of my experimental work would not have been possible. I am deeply grateful for all your help. Thank you to Anna, Katarina, and Marie for keeping the office running smoothly and always saving the day.

To my friends in the division, you made this journey so much more enjoyable. From colleagues, you have all become close friends and an essential part of this chapter in my life. Thank you, Aaron, Anh, Azka, Chahat, Henrik, Hyunkyo, Jing, Maria, Nasrin, Sina, Tharun, and Xiaoyun. And to my officemates, Kushagra and Rosa, thanks for making our office so quiet that even the coffee machine felt awkward making noise.

Thank you to my best friends, Estrella, Pranavi, and Ramya, for your unwavering support. Knowing that I can always rely on you, no matter what, has meant the world to me.

A special mention to my fluffballs, Freja and Mimi, you have made this journey so much easier with your cuddles and chaos… especially chaos.

Finally, to my mom and sisters - Sana and Aliya: your love and unwavering support have been my greatest strength. Mom, you inspire me every day to work hard and be strong. I love you all deeply.

Thank you to everyone who has been part of this journey.

Munavara Farha

Gothenburg, 8th December 2025

Notes

This work was supported by the Swedish Energy Agency within the framework of the project *Thermochemical poly-generation in heat and power plants* (project no. 51182-1). The contribution of RISE Sensor Systems, which enabled the development of the Magnetic Solids Tracing system used in this work, is also acknowledged. Computations using ANSYS Fluent were made possible by resources provided by the National Academic Infrastructure for Supercomputing in Sweden (NAISS), partially funded by the Swedish Research Council through grant agreement no. 2022-06725.

Table of Contents

This page intentionally left blank.

1. Introduction

1.1. Background

Fluidization refers to the phenomenon in which a mass of solid particles transitions to a fluid-like state when subjected to an upward flow of gas or liquid. This phenomenon is central to many industrial operations and has many applications in sectors such as chemical synthesis, pharmaceutical manufacturing, energy production, and food processing. In chemical manufacturing, fluidized bed systems are employed for the synthesis of polymers, where the principal advantage is the homogenization of monomer and catalyst concentrations throughout the reactor, enabling efficient and stringent control of particle growth and polymer properties [1,2]. In pharmaceuticals, the post-processing steps (including granulation, coating, and drying of powders or pellets) benefit from uniform product quality, efficient moisture removal, and precise control over particle characteristics [3–6]. In the energy sector, fluidized bed systems are widely used for processes such as pyrolysis, gasification, and combustion of solid fuels (e.g., biomass and waste), where high levels of mixing provide efficient gas–solids contact and uniform distributions of species and temperature, thereby enabling effective fuel conversion. These features also allow fluidized beds to process a wide variety of feedstocks with different particle sizes and densities [3,7]. In food processing, fluidized beds enable precise control of heating and mixing conditions, which is especially important for delicate, heat-sensitive ingredients. This approach helps maintain consistent product quality while preserving nutritional value and natural flavors [8,9].

The conventional "stationary" bubbling fluidized bed (BFB) is characterized by the formation of gas bubbles when the upward gas flow exceeds the minimum fluidization velocity, suspending the solid particles in a vigorously mixed environment. In this bubbling regime, the gas velocity remains below the level that would generate significant particle entrainment [3,10]. When operated at higher gas velocities, fluidized beds enter the circulating fluidized bed (CFB) regime, where a substantial fraction of the solids is entrained in the gas stream, separated externally (for example, by a cyclone), and recirculated to the bed [3,10]. In BFBs, vertical mixing is promoted by bubble movement and is much more intense than lateral (horizontal) mixing, which limits the gas–solids mixing efficiency at larger scales. In contrast, circulating fluidized beds achieve vigorous solids circulation and gas–solid contacts throughout the reactor; mixing is particularly effective in the dilute core region, while mixing is less intense near the wall [3,10]. Heat transfer in BFBs primarily occurs through hot gas contacting exchange surfaces, with radiative heat transfer sometimes contributing more than convection, depending on the conditions. In CFBs, recirculating hot particles significantly enhance heat transfer efficiency. Furthermore, while process intensification and scale-up in CFBs present their own challenges, these systems offer greater flexibility than BFBs, as adjusting the fluidization velocity or reactor length can improve solids circulation and increase the available heat-extraction area. This can be achieved without encountering the same constraints on mixing degree and temperature uniformity that typically limit the scale-up of larger BFBs. The dynamics within a BFB can be further manipulated through operational parameters, such as the fluidization velocity, distributor configuration, and the introduction of solids feeds or withdrawals [3,10]. The latter adjustments imply BFB operation with solids throughput, where different configurations of the relative orientations of the gas and solids

streams are possible: the solids flow can be arranged in a countercurrent, co-current, or crossflow configuration with respect to the gas flow.

The choice of solids throughput configuration in bubbling fluidized beds can significantly impact mixing patterns within the bed. In co-current configurations, the gas–solids flow occurs in the same direction, whereas in counter-current configurations, the flows are in opposite directions. In bubble column systems, the co-current mode delays the transition to churn-turbulent regimes, producing larger, more stable bubbles and gentler mixing, while the counter-current mode increases turbulence, gas holdup, and bubble breakage, thereby enhancing mass transfer [11]. In fluidized beds, operating in co-current mode at high velocities results in lower mixing efficiency, with solids rapidly exiting the system, whereas the counter-current mode establishes a denser, more stable bed and improves gas–solids contact, albeit at the cost of increased sensitivity to changes in operating parameters [12]. In fixed-bed combustion systems, the co-current mode results in rapid propagation of the reaction front and a clear separation of conversion stages, which is beneficial for fast conversion but limits the overlap of reaction zones and reduces mixing efficiency. In contrast, the counter-current mode results in more pronounced spatial overlap of the drying, devolatilization, and char oxidation zones, uniform solids holdup, and longer fuel residence times, thereby improving conversion efficiency at the expense of a higher pressure drop and greater operational complexity [13]. In downer reactors, the co-current mode promotes smoother particle flow but results in lower and less uniform solids holdup, whereas the counter-current mode yields a uniform velocity profile, higher solids retention, and improved mass and heat transfer, though at the cost of increased pressure drop and greater fluctuations in solids distribution [14].

Crossflow arrangements are characterized by gas–solids flows that occur predominantly perpendicular to each other. In large-scale thermochemical processes such as conventional boilers, enhanced lateral (horizontal) mixing of solids, often achieved through a crossflow mode, is crucial for uniform fuel distribution and stable operation [15–17]. If lateral mixing occurs too slowly, fuel introduced at specific feed-points may not spread evenly across the bed, leading to volatile maldistribution, hot spots, and local temperature fluctuations [16,18]. These issues can result in incomplete combustion, higher emissions, and potential damage to boiler components [16–18]. To compensate for inadequate mixing, operators often increase the air-to-fuel ratio to ensure complete combustion. However, excess air reduces thermal efficiency and increases both flue gas volume and operating costs due to higher fan energy consumption. In addition, the larger flue gas volume requires more expensive gas-cleaning systems, further increasing capital expenses. In pharmaceutical manufacturing, crossflow configurations enable the controlled movement of solids through compartmentalized zones within a single unit [19–21]. The compartmentalization of these beds using weirs enables independent adjustments of process parameters (e.g., spray rate, temperature, and gas velocity) across sequential zones [19,20]. The movement of solids between compartments and the resulting residence time distribution directly affect the moisture content, morphology, and structural properties of the particles [19–22]. Insufficient control over solids transport or excessive particle backmixing can result in non-uniform drying, broad particle-size distributions, and variability in granule porosity and strength, ultimately compromising downstream processing [19,20,22]. In iron ore reduction, the crossflow configuration enables direct processing of fine ores, enhances gas-solid contact, and provides uniform reduction conditions, thereby improving metallization rates and reducing energy use [23].

Table 1-1 provides an overview of representative studies that have utilized fluidized beds with solids crossflow across different applications, summarizing the characteristics of the bulk-phase solids (material, size, density), the operating conditions, and the key findings relevant to solids crossflow. These studies highlight the versatility of crossflow configurations in two distinct applications: thermochemical energy conversion and pharmaceutical manufacturing. Control of the solids crossflow rate and mixing is primarily achieved by adjusting the fluidization velocity, bed inventory, and internal geometric features (baffles, weirs, compartmental walls). By tuning these parameters, operators can regulate the mixing intensity and residence time distribution and minimize the extent of the stagnant zones. Overall, process performance depends on the careful integration of these design and operating variables to optimize crossflow behavior for the specific application.

While the literature demonstrates the adaptability of fluidized beds with solids crossflow, a detailed mechanistic understanding of solids transport in these systems, particularly for thermochemical applications, is lacking. Methods for efficiently and flexibly controlling the solids crossflow are not well-established. The experience gained with solids circulation in risers (CFB furnaces, FCC reactors, etc.) is limited because these units are designed with the constraint of providing sufficient gas and solids residence time and/or heat-exchange area, rather than maximizing external solids circulation. An effective solids circulation is important for maintaining uniform temperature, enhancing mixing, and ensuring stable reactor operation, and is typically managed through adjustments in gas velocity, the use of loop seals, or mechanical devices that regulate solids flow. Therefore, further studies are needed to explore solids conveying configurations that can offer improved performance.

Table 1-1: Overview of key studies in the literature that report fluidized-bed configurations that exhibit solids crossflow.

Reference	Geometric configuration	Solids characteristics	Operating condition	Key findings regarding solids crossflow
Application: Thermochemical energy conversion				
Foscolo et al. [24]	BFB-BFB D_{BFB}: 0.25/0.55 m (tapered)	Type: Copper ρ_p: 8,822 kg/m^3 d_p: 122 μm	T,P: Ambient Fluidization agent: Air u_o/u_{umf}: 1.8–2.5 (upflow bed) u_o/u_{umf}: 1.1 (downflow bed) H: ≈0.275 m	- Solids crossflow between beds is controlled by the difference in fluidization velocities, creating a pressure differential across the baffle opening. - Crossflow keeps buoyant (biomass-like) particles immersed, preventing segregation to the bed surface. - Higher crossflow reduces the extent of stagnant zones and improves bed mixing. - Tapering further limits the size of dead regions.
Wee et al. [25]	BFB-BFB D: 0.48 m, H: 1.8 m - Weir separation	Type: Sand, alumina ρ_p: 2,620–2,638 kg/m^3, 3,992 kg/m^3 d_p: 256–272 μm, 360 μm	T,P: Ambient Fluidization agent: Air u_o/u_{umf}: 0.5–2.5 D_e: 0.173–0.234/0.290 m (gasifier/combustor)	- Poor solids crossflow, and low fluidization quality occur in compartments with a small effective diameter (D_e), due to channeling. - Increasing D_e in the gasifier, beyond a critical threshold, improves fluidization quality.
Kong et al. [26]	Shallow crossflow BFB W: 0.08 m, L: 1–2 m - Baffles	Type: Cristobalite powder ρ_p: 2,309 kg/m^3 d_p: 60 μm	T,P: Ambient Fluidization agent: Air u_o/u_{umf}: 3–4 H: 0.10–0.15 m	- Crossflow beds exhibit near PFR-like solids transport. - Adding baffles further reduces the extent of dead zones and backmixing. - Bed height has a minor effect on the crossflow; solids mixing remains efficient even for shallow beds.
Geng et al. [27]	Crossflow BFB Dimensions: 0.45×0.04×0.2 m^3 - Baffles	Type: Silica sand ρ_p: 2,600 kg/m^3 d_p: 0.2 mm	T,P: Ambient Fluidization agent: Air u_o/u_{umf}: 4–8 H: 0.07–0.13 m	- Increasing solids flux→ narrower RTD. - Increasing bed height (solids inventory) → broader RTD. - Baffle near the outlet prevents short-circuiting and increases the average solids residence time.

Table 1-1 (continued):

Reference	Geometric configuration	Solids characteristics	Operating condition	Key findings regarding solids crossflow
Application: Thermochemical energy conversion				
Sette et al. [28]	Crossflow BFB Area: 1.44 m^2	Type: Bronze ρ_p: 8,900 kg/m^3 d_p: 60 μm	T,P: Ambient Fluidization agent: Air u_o: 0.05–0.09 m/s	- Higher fluidization velocity increases the impact of solids crossflow on accelerating the lateral mixing of fuel particles. - Increased bulk solids circulation rate (crossflow) reduces the residence time of fuel particles.
Vollmari et al. [29]	Dual-chamber fluidized bed Dimensions: 0.11×0.11 m^2 (each compartment) - Weir separation	Type: Beech wood ρ_p: 709–773 kg/m^3 d_p: 6.5–7.2 mm	T,P: Ambient Fluidization agent: Air u_o: 2.0–2.5 m/s	- Increasing fluidization velocity enhances solids crossflow → narrow RTD. - Raising weir height accelerates particle transfer between chambers, further increasing solids crossflow.
Hua et al. [30]	Crossflow BFB Dimensions: 0.12×0.06×0.5 m^3 - Baffles	Type: Calcium carbonate ρ_p: 3,135 kg/m^3 d_s: 341 μm	T,P: Ambient Fluidization agent: Air u_o: 0.4–0.45 m/s	- Increasing fluidization velocity enhances solids crossflow → PFR-like behavior. - Lateral dispersion increases with fluidization velocity and decreases with the presence of baffles.
Gan et al. [31]	Quasi-slot-rectangular spouted bed (QSRSB) Dimensions: 0.9×0.2×0.8 m^3 - Inclined base (45°)	Type: Bottom ash from CFB boiler (sieved) ρ_p: 2,344 kg/m^3 Sizes: 0.25–0.35, 0.35–0.50, 0.50–0.71 mm	T,P: Ambient Fluidization agent: Air u_o: 0.7–3.67 m/s H: 0.1–0.2 m	- Enhanced solids crossflow improves mixing and limits the occurrence of defluidization and agglomeration. - Higher fluidization velocity, increased bed height, and wider air inlet promote stronger crossflow and mixing. - QSRSB enables sufficient crossflow and mixing at lower gas velocities than conventional BFBs.

Table 1-1 (continued):

Reference	Geometric configuration	Solids characteristics	Operating condition	Key findings regarding solids crossflow
Application: Pharmaceutical manufacturing				
Diez et al. [19,22]	Horizontal fluidized bed spray granulator Dimensions: 1×0.25×0.4 m^3 -Weir separation	Type: Sodium benzoate ρ_p: 1,440 kg/m^3 d_p: 0.5–2.5 mm	Drying temperature: 100°–200°C u_o: 3 m/s	- Higher fluidization velocity → stronger solids crossflow. - Overflow/no-weir configurations promote stronger backmixing → broad RTD. - Underflow/sideflow weirs restrict backmixing → narrow RTD.
Meyer et al. [32]	Pseudo-2D horizontal fluidized bed -Weir separation	Type: γ-alumina ρ_b: 970 kg/m^3 d_p: 1.8±0.1 mm	T,P: Ambient Fluidization agent: Air u_o: 3–5u_{mf} m/s	- Higher fluidization velocity increases particle exchange across the weir and decreases the degree of internal recirculation (backmixing) → PFR-like behavior. - Pressure differences drive preferential crossflow; when bed heights are equal, crossflow is symmetric and dominated by bubble-induced mixing.
Bachmann et al. [33,34]	Horizontal fluidized bed Pilot plant: 1×0.2 m^2 Lab-scale: 0.6×0.08 m^2 -Weir separation	Type: γ-alumina ρ_p: 3,980 kg/m^3 d_p: 1.8–3 mm	Fluidization agent: Air u_o: 2.8–3.4 m/s (pilot plant) u_o: 1.9–2.8 m/s (lab-scale)	- Higher fluidization velocity increases axial dispersion → broad RTD. - Higher solids flow rate and reduced weir height → PFR-like behavior. - Longer beds (higher length/width ratio) → PFR-like behavior.
Zhang et al. [35]	Horizontal fluidized bed Dimensions: 0.6 m × (0.04–0.2) m × 0.3 m - Integrated screw conveyor	Type: Pharmaceutical granules ρ_b: 288 kg/m^3 $d_{10}/d_{50}/d_{90}$: 47/121/1,260 μm	Air temperature: 40°–60°C u_o: 0.5–0.8 m/s	-Screw conveyor enhances plug flow and reduces backmixing. -Increased fluidization velocity enhances crossflow but can also increase bypassing.
Note: The term "horizontal fluidized bed" as used in these works refers to a multi-compartment system arranged in a horizontal configuration, with solids flowing laterally from one chamber to the next, as opposed to the typical vertical solids movement in classical bubbling or circulating beds.				

Regarding the characteristics of solids flow in crossflow configurations, important questions about the underlying transport mechanisms remain unanswered. In particular, the relationship between convection—the mean horizontal movement of solids intentionally induced to create crossflow (termed **forced horizontal convection**)—and dispersion, representing the superimposed mixing on this mean flow, is not fully understood. The influence of operational parameters on these processes and system non-idealities also requires further investigation. Macroscopic solids convection strongly affects mixing by dispersion, which in turn shapes residence time distributions and governs concentration and temperature gradients, ultimately impacting chemical reaction efficiency. Moreover, the impact of crossflow on fluidization quality, for example, the persistence of non-idealities such as defluidized zones and gas channeling, is not well understood. Although some studies have provided spatially resolved data [27,29,30,36], detailed characterization of flow macrostructures in the presence of a solids crossflow has received limited attention. Furthermore, a key challenge lies in characterizing the rheological behavior of dense beds with horizontal solids flow. Once this parameter is well understood, frictional losses can be reliably estimated, which in turn governs the established solids flowrate, enables effective control of energy consumption and equipment longevity, and ultimately ensures stable operation [37].

Acquiring insights into the behavior of solids crossflows in bubbling beds necessitates precise measurement approaches, for which various methods are currently available [38]. Intrusive methods interact directly with the bed material and may disturb the flow; examples of these involve the use of: the mass accumulation method [39,40], which quantifies solids circulation rates by temporarily halting the flow and collecting solids; optical fiber probes [41–43], which detect local particle velocities or concentrations via interruptions of light signals; hot film anemometers [44], which measure fluid velocity through thermal dissipation; and thermocouples [45–47], which rely on the thermoelectric effect. Conversely, non-intrusive techniques maintain the natural state of the flow and are preferred for their minimal impact on system dynamics. These techniques include: acoustic emission sensors [48–50], which capture collision-generated sound; particle image velocimetry [51–54], which visualizes flow by tracking seeded particles; infrared thermography [55,56], which maps surface temperature fields by detecting emitted infrared radiation; radioactive particle tracking [57–59], which reconstructs trajectories of isotopically tagged particles; magnetic particle tracking [60–62], which maps flow paths using magnetically embedded particles; and electrical capacitance tomography [63–66], which monitors changes in capacitance that result from variations in the dielectric properties of the materials. However, each method has limitations in accuracy, spatial and temporal resolution, or bed disturbance, making it difficult to obtain dependable measurements in these systems.

In summary, optimizing the process design, scale-up, and industrial deployment of bubbling fluidized bed configurations with solids crossflow requires not only adjusting operational parameters and geometric features to induce crossflow, but also addressing critical knowledge gaps in the fundamental mechanisms of solids transport. This calls for integrated experimental efforts that employ robust measurement techniques, complemented by modeling tools, to gain detailed insight into the underlying flow phenomena.

1.2. Aim and scope

This thesis seeks to advance understanding of the mechanism by which forced horizontal convection impacts the solids flow in bubbling fluidized beds. The research is structured around the following core objectives: (i) evaluating experimental methods for measuring horizontal solids circulation; (ii) comparing the efficiencies of mechanisms for inducing solids horizontal convection; (iii) characterizing bed solids transport with the emphasis on the relationships between convection, dispersion, and fluidization quality; (iv) analyzing the influence of solids crossflow on the underlying flow structures; (v) investigating frictional losses and the rheological properties of the conveyed dense solids suspension; and (vi) assessing the effects of bulk solids crossflow on the mixing behaviors of large, low-density particles. To address these objectives, the research is structured around six corresponding research questions (**RQ1**–**RQ6**), summarized in **Table 1-2** along with the corresponding methodologies and solids flow parameters investigated. Research questions **RQ1**–**RQ5** are each addressed in one of the five appended papers, whereas **RQ6** is examined exclusively in this essay.

Paper I systematically compares the use of four techniques—integral mass accumulation, differential mass accumulation, thermal tracing, and magnetic solids tracing—for measuring horizontal solids flow in bubbling fluidized beds with induced crossflow. **Paper II** explores five alternative mechanisms for generating horizontal movement of solids in bubbling fluidized beds: free solids splashing (driven by bubble bursts at the bed surface); confined solids splashing (enhanced particle lift via turbulence); slugging (periodic vertical transport mediated by rising gas slugs); solids entrainment (particle lifting from a high-velocity gas flow); and directed gas injection (lateral momentum from angled nozzles). **Paper III** characterizes the horizontal solids crossflow in bubbling fluidized beds using three analytical approaches: deconvolution; convection-dispersion modeling; and compartment modeling. Furthermore, the work examines how operational parameters—solids crossflow rate, bed height, and fluidization velocity—affect convective and dispersive transport modes, residence time distributions, and fluidization quality. **Paper IV** provides a spatially-resolved analysis of the flow structures and transport mechanisms in a bubbling fluidized bed with horizontal solids crossflow, using Eulerian–Eulerian CFD modeling. **Paper V** investigates frictional losses and the rheological behavior exhibited during horizontal solids transport, focusing on the effects of solids velocity, channel width, and bed height.

The reference system for this work is a fluid-dynamically scaled cold-flow unit operated under ambient conditions. Glicksman's scaling laws are applied to ensure dynamic similarity with industrial-scale units for thermochemical fuel conversion operating at high temperature. In line with this, the study limits its scope to Geldart B-type bulk solids. Further, the scope is limited to fluidized beds operating within the bubbling regime. The work combines experimental investigations with a range of modeling approaches, including 0D (compartment) models, 1D macroscopic transport models, and 3D CFD models (Eulerian–Eulerian and Lagrangian particle-tracking).

Table 1-2: Overview of the research questions, investigated solids flow parameters, and methodologies applied in the present study.

RESEARCH QUESTIONS			PAPER	SOLIDS FLOW PARAMETERS						METHODOLOGY														
				Solids convection	Solids dispersion (macro-scale)	Solids dispersion (micro-scale)	System non-idealities	Fanning friction factor	Solids conveying efficiency	MEASUREMENT TECHNIQUES	Integral mass accumulation	Differential mass accumulation	Thermal solids tracing	Magnetic solids tracing	Pressure drop (horizontal)	MODELING APPROACHES	Macroscopic mass balance	Energy transport equation	Species transport equation	Compartment model	Power-law model	Eulerian-Eulerian model	Lagrangian particle tracking
BULK-PHASE SOLIDS	RQ1	How can the solids circulation rate be accurately measured?	I	×							×	×	×	×			×	×						
	RQ2	How effectively can different fluidization regimes be exploited to induce horizontal solids convection in fluidized beds?	II	×					×					×	×				×					
	RQ3	What is the impact of operational parameters on macroscopic solids transport and the fluidization quality?	III	×	×		×							×					×	×				
	RQ4	How do operational parameters influence the solids flow structure in a bubbling bed with crossflow?	IV	×	×	×								×					×			×		
	RQ5	How does the rheological behavior of solids influence frictional losses in the horizontal flow of solids under bubbling conditions?	V	×				×						×	×				×		×			
LEAN-PHASE SOLIDS	RQ6	What is the impact of bulk solids crossflow on the transport of larger, lighter particles?	-	×	×									×					×			×	×	

2. Theory

This chapter introduces the key concepts and modeling strategies for solids flow in bubbling fluidized beds with induced crossflow. **Section 2.1** outlines the fluidization regimes. **Section 2.2** describes the solids transport mechanisms and the distinction between bulk-phase and lean-phase solids. **Section 2.3** discusses the non-Newtonian and regime-dependent rheological behaviors of granular suspensions. **Section 2.4** reviews the four modeling approaches for solids transport in fluidized beds used in the present study: the compartment model, macroscopic transport models, and computational fluid dynamics (CFD) models, which include both the gas–solids Eulerian–Eulerian model for gas–bulk solids flow and the Lagrangian particle tracking (LPT) approach for the lean solids phase.

2.1. Fluidization regimes

Fluidization regimes define the various states observed in fluidized beds, which exhibit distinct particle–fluid interaction patterns as a gas flows through a bed of solid particles. The transitions between regimes are primarily governed by fluid velocity, particle properties, and fluid characteristics. **Figure 2-1** illustrates the sequence of fluidization regimes encountered as the gas velocity increases. At low velocities, the system operates as a fixed bed, with stationary particles and gas passing through the interstitial spaces. Upon reaching the minimum fluidization velocity, the bed behaves as a fluidized medium, exhibiting fluid-like properties without bubble formation. A further increase in gas velocity induces the bubbling fluidization regime, characterized by the generation and ascent of gas bubbles that promote solids mixing. In beds with specific geometries (e.g., narrow and deep), the system may transition to the slugging regime, where large bubbles span the bed's cross-section, causing a plug-like movement. As the velocity increases further, the turbulent fluidization regime is established, characterized by intense gas–solid interactions and the absence of discrete bubbles. With further increase in the gas velocity, the system transitions to lean-phase fluidization with pneumatic transport. In this regime, bubbles vanish, and solids are entrained and transported upwards as a dilute, dispersed phase, leading to lower particle concentrations in the freeboard and minimal pressure fluctuations. This behavior is characteristic of a circulating fluidized bed (CFB), where high gas velocities enable continuous solids transport throughout the reactor.

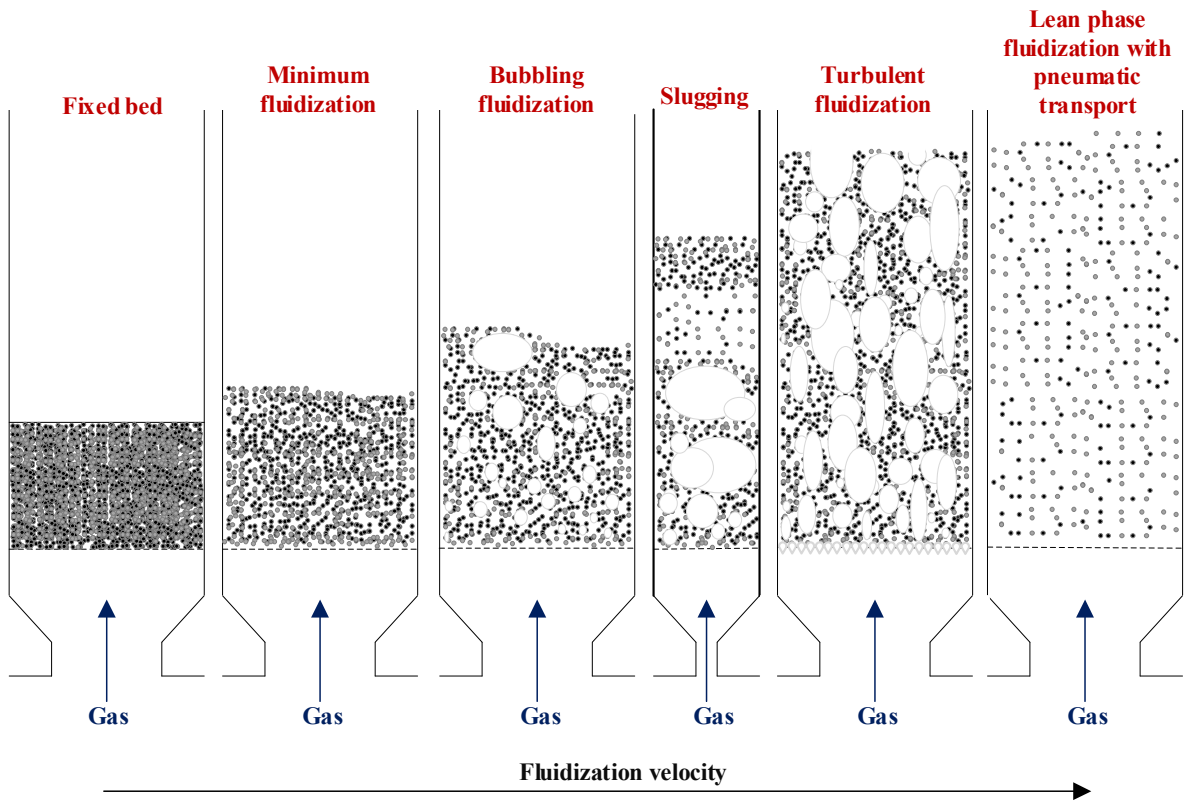

Figure 2-1: Fluidization regimes established by varying the fluidization velocity.

This study investigates alternative methods for driving solids flow beyond the conventional use of a riser by examining several conveying configurations that leverage distinct gas–solids interactions across different fluidization regimes. The efficiency of solids convection is defined as the ratio of the flow energy transferred to horizontally conveyed solids to the energy

supplied via the gas phase, as expressed by Eq. [1]. This metric enables direct comparison of energy utilization across different configurations—a crucial step for optimizing reactor design and minimizing operational costs.

$$\eta = \frac{E_s}{E_{in}} \quad [1]$$

The energy effectively imparted to the horizontal solids flow is determined by the velocity and the pressure drop along the flow direction:

$$E_s = u_s \cdot A_{MZ} \cdot \Delta P_{TZ} \quad [2]$$

The energy input to the solids suspension by the conveying gas is defined as:

$$E_{in} = \frac{\gamma}{\gamma - 1} P_{Atm} Q_{CZ} \left[\left(\frac{P_{Plenum}}{P_{Atm}} \right)^{\frac{\gamma-1}{\gamma}} - 1 \right] \quad [3]$$

2.2. Solids transport mechanisms

Solids mixing in stationary bubbling fluidized beds is predominantly influenced by the dynamics of the interactions between particles and bubbles. Within the dense bed, solids migrate downward as they fill the spaces generated by ascending bubbles [3,67]. Concurrently, particles from the emulsion phase surrounding the rising bubbles are entrained into the wakes of these bubbles and transported upwards [3,67]. In the splash zone at the bed surface, the eruption of bubbles ejects particles ballistically, promoting lateral transport [3,67]. This interplay of vertical and lateral movements results in toroidal circulation of the solids along preferred bubble pathways, characterized by upward flow in the bubble wakes and downward flow in the interstitial regions [68–70]. A schematic representation of these flow patterns in a bubbling fluidized bed with induced solids crossflow is shown in **Figure 2-2**.

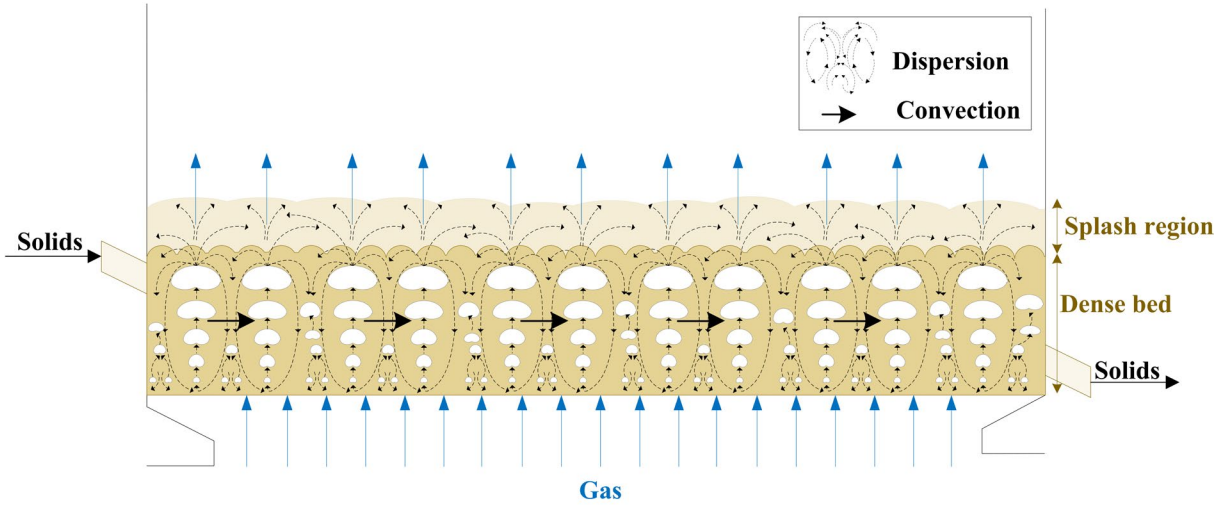

Figure 2-2: Schematic of a bubbling fluidized bed with induced solids crossflow.

The introduction of a horizontal solids crossflow imposes an additional convective field, producing a net solids transport that overlays the solids mixing induced by the bubble motion. In this work, **macroscopic convection** refers to the mean horizontal transport of solids driven by the imposed crossflow [71,72]. **Macroscopic dispersion** refers to the mixing superimposed on this mean flow, resulting from both local velocity fluctuations (due to particle collisions

and small-scale turbulence) and the larger-scale motions associated with bubble passages and coherent flow structures [72,73].

Dispersion describes the spreading of solids in the bed resulting from the random motion of individual particles, analogous to the Brownian motion observed in a homogeneous phase [61,68,69,74]. In fluidized beds, dispersion can be distinguished at both the macro- and micro-scales. Macro-scale dispersion emerges from the cumulative effects of repeated bubble passages and the coherent flow patterns that they generate, often manifesting as large vortices in stationary bubbling beds without crossflow. In this study, macro-scale dispersion is evaluated using the mean squared displacement (MSD), which is calculated from multiple tracked particle trajectories over time, following the classical Einstein relation, $D = L^2/(2t)$, with corrections applied in the presence of macroscopic convection [75–78].

Granular temperature is closely related to micro-scale dispersion. However, converting it to a dispersion coefficient requires knowledge of the spatial distribution of the collision frequency, which standard analytical expressions cannot reliably estimate across varying voidage ranges [73,79]. Micro-scale dispersion has both laminar and turbulent components. The laminar component arises from the velocity fluctuations of individual particles relative to the local mean, primarily due to interparticle collisions [51,73,80,81]. This component can be estimated by dividing the granular temperature—a scalar variable representing the kinetic energy of particle velocity fluctuations, as described by the energy conservation equation for solids (see Eq. [20])—by the dominant frequency of these fluctuations [51,73,81,82]. Turbulent dispersion results from the collective dynamics of bubbles and particle clusters, which induce eddies and localized mixing across the bed [51,73,79–82]. Its intensity—and the resulting turbulent dispersion coefficient in each direction—is quantified from the Reynolds normal stresses and the corresponding Lagrangian timescales of these velocity fluctuations.

Lean-phase solids (larger, lighter particles) introduced into the system exhibit distinct trajectories, which are governed by the dynamics of the bubbles and the solids suspension, as well as by their own physical properties. **Figure 2-3** illustrates the principal mechanisms affecting the movements of lean-phase solids in a bubbling fluidized bed. Note that these pathways may change in the presence of a crossflow. In the figure, black lines indicate the bed solids pathways, and red markers indicate the introduced particles, with possible representative trajectories labeled (i) through (vi).

Upon entry, these particles encounter several characteristic transport mechanisms [70,83–86]. As bubbles erupt at the bed surface, they predominantly (i) scatter the particles laterally into the splash region. Some (ii) remain suspended at the surface, while (iii) others begin to sink through the emulsion phase, migrating downwards among the bulk solids. During this descent, (iv) certain particles may be entrained in the wakes of rising bubbles and (v) carried upwards along the bubble paths. As the bubbles approach the surface, (vi) the particles are released from the wakes and reintroduced into the bed. Importantly, these dynamics vary across the bed and depend on local conditions. The residence time associated with each type of movement, as well as the frequency with which particles transition between them, can differ considerably. Consequently, fuel particles may accumulate preferentially in certain regions, leading to spatial heterogeneities in the distribution of solids within the bed.

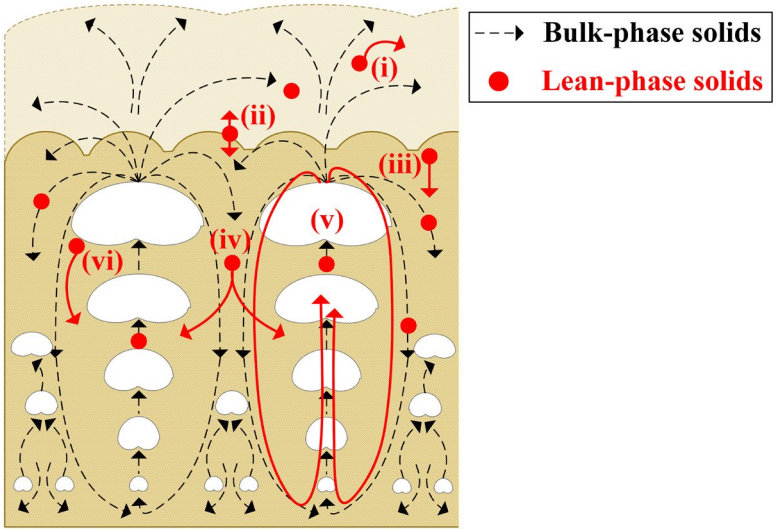

Figure 2-3: Schematic of the principal transport pathways for lean-phase solids (larger, lighter particles) in a bubbling fluidized bed, involving the following steps: (i) lateral scattering into the splash zone; (ii) temporary surface suspension; (iii) sinking through the emulsion phase; (iv) entrainment in bubble wakes; (v) upward transport with bubbles; and (vi) release from the bubble wake and re-entry into the bed.

2.3. Non-Newtonian granular flow

There are significant challenges to understanding the rheology of fluidized beds, owing to their inherently non-Newtonian behaviors and the limited availability of comprehensive studies in the literature [87,88]. Non-Newtonian fluids are those whose apparent viscosity varies with the applied shear rate, in contrast to Newtonian fluids, which exhibit a constant ratio of shear stress to shear rate (i.e., constant viscosity). **Figure 2-4** illustrates the characteristic rheological responses of various fluid types.

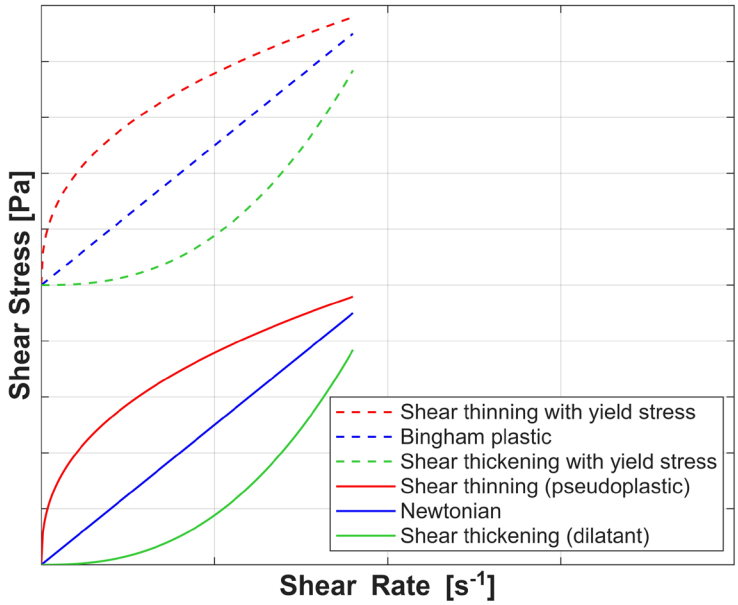

Figure 2-4: Rheological profiles for different fluid types.

Shear-thinning (pseudoplastic) fluids show a decrease in apparent viscosity with increasing shear rate, facilitating flow under higher stress levels. In contrast, shear-thickening (dilatant)

fluids exhibit an increase in apparent viscosity as the shear rate rises, thereby becoming more resistant to deformation. In addition, some non-Newtonian fluids exhibit a yield stress, requiring the application of a minimum stress before flow commences (as indicated by the red curves in **Figure 2-4**).

2.3.1. Rheological models

Rheometry is the experimental measurement of a material's flow and deformation behavior under applied forces. Various experimental techniques have been employed to characterize the rheological properties of fluidized beds. The falling sphere method determines viscosity by monitoring the descent of a sphere through a medium and applying Stokes' law [88–90]. Capillary techniques assess flow behavior within narrow tubes using the Hagen–Poiseuille equation [88–90], while Couette flow analysis examines the shear stress and shear rate generated between two moving surfaces [88–90].

To facilitate analyses of horizontal solids transport, the system is analogized to a liquid flow in a channel. Assuming an incompressible, steady-state, fully developed single-phase flow, the pressure drop gradient along the channel is related to the solids flow velocity, conduit geometry, and the properties of the solids suspension via the friction factor, as follows:

$$\frac{\Delta P}{\Delta L} = \frac{2 f_F \rho_{fluid} {u_s}^2}{D_h} \quad [4]$$

A force balance analysis enables the formulation of an expression for the average wall shear stress along the wetted perimeter for generalized fluids flowing in rectangular channels:

$$\tau_w = D_h \cdot \frac{\Delta P}{\Delta L} \quad [5]$$

Previous studies of the fully developed laminar flow of non-Newtonian fluids have introduced correlations for specific conduit geometries, including non-circular shapes, using a generalized Reynolds number (Re^*) and a geometric constant (C):

$$f_F = \frac{C}{Re^*} \quad [6]$$

Accurate representation of these rheological characteristics requires the development of robust theoretical models. However, most existing models have been developed for single-phase fluids, and their applicability to complex multiphase systems, such as fluidized beds, remains insufficiently explored [87,88]. In this study, the flow of solids in a rectangular open channel is analyzed using three established models: Kozicki et al. [91–94], Delplace–Leuliet [95], and Kostic–Harnett [96,97]. The analytical frameworks for these models are summarized in **Table 2-1**. To describe the rheology of non-Newtonian fluids, the power-law model (Eq. [7]) is employed. This model relates the wall shear stress to the apparent shear rate through the flow behavior index n^* and the consistency index k^*, capturing the nonlinear relationship between these quantities:

$$\begin{aligned} \tau_w &= k^* {\dot{\gamma}_a}^{n^*} \\ \Rightarrow \tau_w &= k^* \left(\frac{8 u_s}{D_h}\right)^{n^*} \end{aligned} \quad [7]$$

The apparent shear rate is determined under the assumption of Newtonian flow behavior and used as an initial estimate for the wall shear rate.

The models presented in **Table 2-1** extend conventional expressions to account for geometric effects using distinct variables (a, b, ω, β). Kozicki et al. [91] (**Model 1**) developed a two-shape-factor (a,b) framework for analyzing the flow in rectangular open channels. Kostic–Hartnett [96] combined the approaches of Kozicki et al. [91–94] and Metzner–Reed [98], introducing a geometry parameter, ω, for non-circular ducts. Ayas et al. [97] (**Model 2**) further refined this framework for application to shear-thinning fluids. Delplace–Leuliet [95] (**Model 3**) showed that the geometrical coefficients used in previous models, although accounting for duct shape, included a denominator term (8^{n-1}) that is specific to circular ducts, and they proposed a modification using a geometric parameter, β.

Table 2-1: Rheological parameters in power-law-based models for rectangular channels.

	Model 1	**Model 2**	**Model 3**
Reynolds number, Re^* [-]	$\frac{\rho_{fluid} u_s^{2-n} D_h^n}{8^{n-1} K_{KT} \left[\frac{a+bn}{n}\right]^n}$	$\frac{\rho_{fluid} u_s^{2-n} D_h^n}{8^{n-1} K_{KH} \omega \left[\frac{3n+1}{4n}\right]^n}$	$\frac{\rho_{fluid} u_s^{2-n} D_h^n}{\beta^{n-1} K_{DL} \left[\frac{24n+\beta}{(24+\beta)n}\right]^n}$
Flow behavior index, n^* [-]	n		
Flow consistency index, k^* [Pa.s^n]	$K_{KT} \left\{\frac{a+bn}{n}\right\}^n$	$K_{KH} \omega \left[\frac{3n+1}{4n}\right]^n$	$K_{DL} \left[\frac{24n+\beta}{(24+\beta)n}\right]^n$
Wall shear rate, $\dot{\gamma}_w$ [s^{-1}]	$\left[\frac{a+bn}{n}\right]\left[\frac{8u_s}{D_h}\right]$	$\omega^{1/n}\left[\frac{3n+1}{4n}\right]\left[\frac{8u_s}{D_h}\right]$	$\left[\frac{24n+\beta}{(24+\beta)n}\right]\left[\frac{\beta u_s}{D_h}\right]$

Alternatively, by extending the generalized Rabinowitsch–Mooney model developed by Kozicki et al. [91,92], this work proposes the following formulation for the flow consistency index in non-circular channels:

$$k^* = K[f(W, H_b)]^n$$
$$\Rightarrow k^* = K\left[C_W\left[\frac{W}{d_p}\right] + C_{H_b}\left[\frac{H_b}{d_p}\right]\right]^n \quad [8]$$

Here, C_W and C_{H_b} are empirical constants that account for the effects of channel width and expanded bed height, respectively.

2.3.2. Granular flow regime

The rheological behavior of a solids suspension is highly dependent on the granular flow regime governing the system. Therefore, investigating these regimes in the context of the present study is essential for determining the friction dynamics of the system. At low particle velocities, the quasi-static regime prevails, where frictional particle–particle interactions dominate, resulting in minimal variation of the friction coefficient and a solid-like behavior of the suspension. As particle movement increases, the system enters the intermediate (dense) regime, where both frictional and collisional interactions significantly affect the rheology, and the solids exhibit liquid-like characteristics. At even higher particle velocities, the collisional regime is established, wherein particle collisions are the primary mechanism of momentum transfer, inertial effects become significant, and the friction coefficient stabilizes or decreases as the influence of the confining pressure diminishes. The $\mu(I)$ constitutive law, as expressed by Eq. [9], provides an analytical framework for describing the transition from quasi-static to

collisional flow as particle movement increases [99–101]. This relation expresses the macroscopic friction coefficient, $\mu(I)$, as a function of the inertial number, I:

$$\mu(I) = \mu_S + \frac{\mu_2 - \mu_S}{I_0/I + 1} \quad [9]$$

where μ_S is the static friction coefficient, μ_2 is the friction coefficient at high inertial numbers, and I_0 is a constant. The macroscopic friction coefficient is defined as the ratio of the wall shear stress to the particle pressure P_p [100,102]. The inertial number quantifies the flow state by comparing the timescale of particle rearrangement due to inertia with the timescale of deformation under shear stress:

$$I = \frac{t_P}{t_{\dot{\gamma}_w}} = \frac{\sqrt{\rho_s d_s^2 / P_p}}{1/\dot{\gamma}_w} \quad [10]$$

2.4. Modelling frameworks for solids transport in fluidized beds

The simulation of solids transport in fluidized beds can be accomplished using frameworks that operate across multiple scales and degrees of complexity [74,103]. Zero-dimensional (0D) or lumped parameter models treat the fluidized bed system as a single, ideally mixed control volume with no internal spatial gradients. These models are primarily used to calculate overall mass and energy balances, and to provide rapid estimates of key system-level variables, such as total solids hold-up, average solid and gas concentrations, global heat transfer rates, flue gas composition, and overall thermal efficiency [104–106]. Another approach is to describe the system using reactor models, such as perfectly mixed or plug flow reactors [71]. To capture deviations from ideal behavior, compartment models further subdivide the bed into interconnected zones with distinct mixing characteristics [71].

Macroscopic models describe the transport of species in a fluidized bed without explicitly solving the momentum balances and, therefore, they do not resolve local gas–solids velocity fields [103]. These models can be formulated in 1D/1.5D/2D/3D, depending on the specific requirements. Convection-dispersion transport models are incorporated into these frameworks to describe the macroscopic gas-solids mixing behavior within the bed. They can be formulated for either steady-state or transient conditions [107]. Furthermore, empirical parameters and correlations—often derived from experimental data—are typically incorporated for key quantities.

To resolve the local gas–solids flow structures in fluidized beds, advanced multiphase modeling techniques—collectively known as computational fluid dynamics (CFD)—are employed to solve the governing momentum balances. In the Eulerian–Eulerian approach, both phases are treated as interpenetrating continua, with the behavior of the solid phase being described by the kinetic theory of granular flow (KTGF) [79,108,109]. The mass and momentum conservation equations are solved separately for the gas and solid phases, with interphase mass/momentum exchange terms describing their interactions [108,110–113]. In the Eulerian–Lagrangian approach, the fluid phase is modeled as a continuum, while individual particles are represented as discrete elements using a Lagrangian framework, with two-way coupling of the phases [114–116]. The fluid flow is governed by continuum equations, and each particle's trajectory is determined by integrating Newton's equations of motion, allowing

for direct modeling of both fluid–particle and particle–particle interactions [114–116]. This approach encompasses a range of models, from coarse-grained particle (CGP) [117–119] and multi-phase particle-in-cell (MP-PIC) [120–122] methods that capture particle clusters, to fully resolved particle-level simulations, such as direct numerical simulation (DNS) [115,123,124] and discrete particle methods (DPM) [125–128], offering varying degrees of resolution and computational cost. **Table 2-2** presents a selection of studies from the literature that use a range of modeling frameworks to analyze the mechanisms of solids transport in fluidized beds with a crossflow configuration. Notably, relevant studies for this type of system remain relatively sparse. The reviewed works encompass macroscopic transport, compartment, Eulerian–Eulerian, and coupled CFD–DEM modeling techniques.

Table 2-2: Summary of the modeling approaches and key findings in studies of the transport mechanisms in fluidized beds with a solids crossflow.

Reference	Modeling technique	Main findings
[28,129]	Macroscopic transport model	-Dispersion increases with bed height, fluidization velocity, and distributor pressure drop. -Lateral crossflow and bubble-induced dispersion both significantly affect mixing.
[31]		-Dispersion increases with gas velocity, bed height, and air inlet width.
[26]	Compartment model	-Increased air velocity and bed length promote plug-flow behavior. -Addition of baffles reduces the bypass flow and dead zones, shifting solids transport towards plug flow.
[34]		-Increasing the outlet weir height or adding internal baffles broadens the RTD.
[27]	Eulerian–Eulerian (with kinetic theory of granular flow)	-Higher solids inventory or bed height increases the mean residence time, whereas a higher solids flux reduces it. -Solids backmixing is significant, yielding a long-tail RTD profile in crossflow bubbling fluidized beds.
[30]		-Baffles significantly narrow the RTD curve and move it towards a plug-flow behavior, indicating reduced backmixing. -Increasing the gas velocity reduces the mean residence time, although the effect of baffles is more pronounced. -Particle flow and outflow fluctuations are more stable in baffled beds compared to free beds, leading to smoother solids discharge.
[36]		-Compartmentalization with baffles narrows the RTD and reduces backmixing, promoting plug flow. -Increasing the gas velocity or bed outlet height leads to faster solids discharge but broadens the RTD, indicating increased dispersion.
[29]	Computational Fluid Dynamics - Discrete Element Method (CFD-DEM)	-Higher mass inflow rate or fluidization velocity results in shorter, narrower RTDs, approaching plug-flow behavior.

2.4.1. Compartment model

The reactor design literature provides analytical models that describe idealized flow patterns, most notably those in the continuous stirred tank reactor (CSTR) and the plug flow reactor (PFR). In the CSTR, perfect mixing yields uniform concentrations and temperatures, whereas in the PFR, no axial mixing is assumed, resulting in concentration gradients along the flow path. PFRs generally achieve higher conversion rates for fast or highly selective reactions, whereas CSTRs are preferred for processes that require uniform mixing and temperature control. In practice, reactors frequently exhibit non-ideal behavior, such as dead zones, short-circuiting, and channeling, which affect the dynamics of solids transport. In fluidized beds, dead zones are localized regions where solid particles remain largely immobile and do not participate in bulk movement [71]. Short-circuiting describes the rapid passage of solids from the inlet to the outlet via pathways that bypass the main flow, often due to insufficient fluidization or poor reactor design [71]. Channeling refers to the development of preferential flow paths that allow the fluid and solids to move quickly through specific regions, resulting in an uneven distribution and limited interactions across the bed [71].

Figure 2-5 illustrates ideal reactor concepts alongside common deviations observed in practical operation. To represent real systems more accurately, it is often necessary to combine ideal reactor models with explicit consideration of non-idealities.

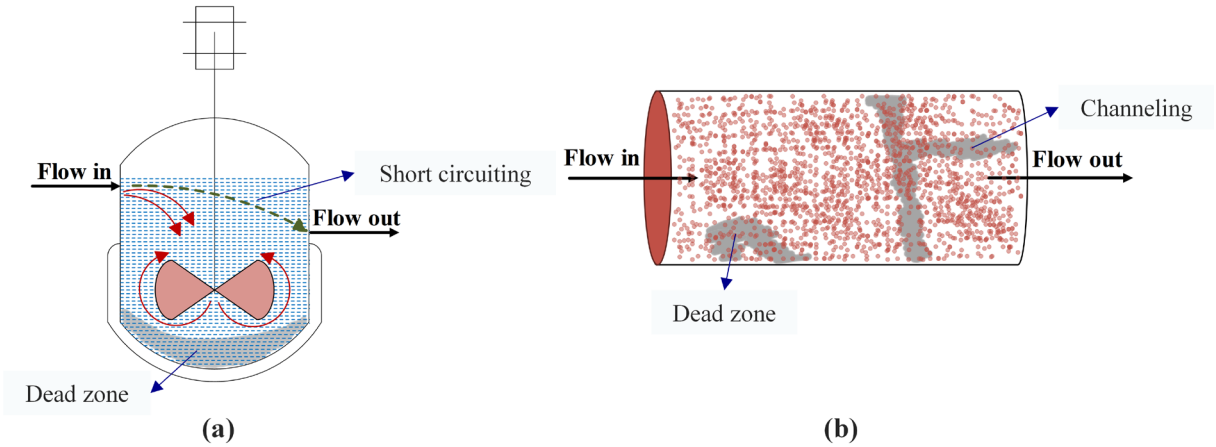

Figure 2-5: Schematic of the non-ideal flow patterns in: (a) a continuous stirred tank reactor (CSTR); and (b) a plug flow reactor (PFR).

A compartment model represents the flow within a reactor by combining distinct subunits, enabling quantification of the flow parameters—such as dead zones—by fitting the model's predicted residence time distribution (RTD) to experimental measurements [71]. In this work, solids mixing in the crossflow direction is modeled as a series of CSTRs that capture the dispersive component of the flow, in combination with a PFR to represent the convective component, as illustrated in **Figure 2-6**.

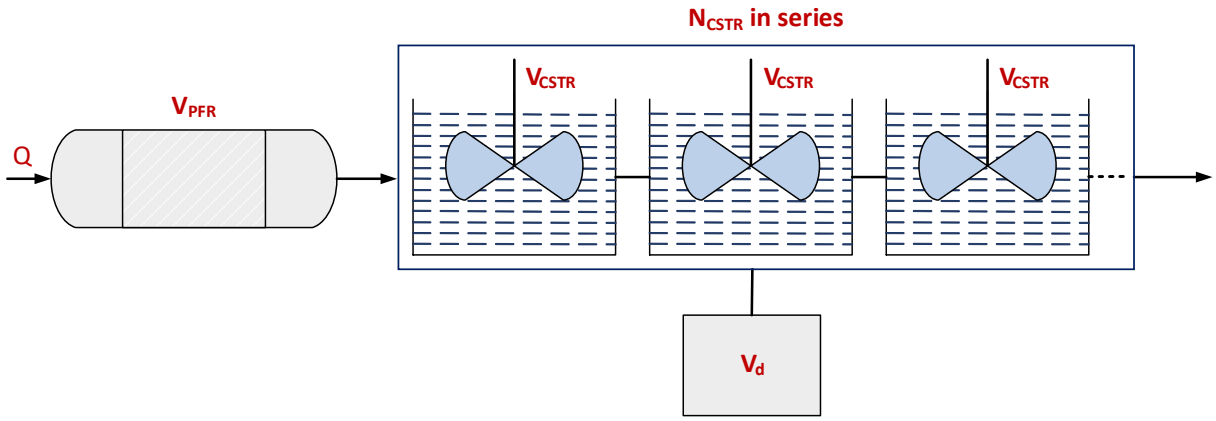

Figure 2-6: Schematic of the compartment model employed, featuring a plug flow reactor (PFR), a series of continuous stirred tank reactors (CSTRs), and a stagnant compartment.

The model parameters include the number and volume of the CSTRs (N_{CSTR}, V_{CSTR}), the volume of the PFR (V_{PFR}), and an additional stagnant compartment (volume V_d) representing the dead zones—corresponding to defluidized regions that reduce the effective solids flow volume. The selection and layout of the compartments require general information regarding the expected flow behavior (typically extracted from concentration transients), and the process involves some iteration. The configuration shown in **Figure 2-6** is a suitable representation of the system studied in this work.

For this layout, Eq. [11] provides the transient outlet concentration of a tracer given its input concentration $C_{in}(t)$. Here, m_t and Q_t denote the mass and volumetric flowrate of the injected tracer, respectively; τ is the mean residence time of solids; and i_d represents the volume fraction of the dead zones (V_d) in the system [71].

$$C_{i,out}(t) = C_{i,in}(t) + \frac{m_t}{Q_t}\left\{\frac{1}{\tau(1-i_d)}\frac{{N_{CSTR}}^{N_{CSTR}}}{(N_{CSTR}-1)!}\left[\frac{(t-\tau_{PFR})}{\tau(1-i_d)}\right]^{N_{CSTR}-1}\right\} e^{-N_{CSTR}\frac{(t-\tau_{PFR})}{\tau(1-i_d)}} \quad [11]$$

Furthermore, the solids residence time distribution (RTD), or E-curve, for the compartment model layout in **Figure 2-6** is given by:

$$E(t) = \left\{\frac{1}{\tau(1-i_d)}\frac{{N_{CSTR}}^{N_{CSTR}}}{(N_{CSTR}-1)!}\left[\frac{(t-\tau_{PFR})}{\tau(1-i_d)}\right]^{N_{CSTR}-1}\right\} e^{-N_{CSTR}\frac{(t-\tau_{PFR})}{\tau(1-i_d)}} \quad [12]$$

2.4.2. Macroscopic transport model

The inclusion of convection and dispersion terms enables quantification of both the advective transport and the spreading of solids within the system. In this study, two transport equations—for solids species conservation and energy conservation—are employed to characterize these transport modes. The equations are applied in a simplified 1D discretization of the geometry, with the spatial coordinate corresponding to the horizontal direction of the solids crossflow, as depicted in **Figure 2-7**. This approach does not resolve complex flow structures, dead zones, or recirculation phenomena.

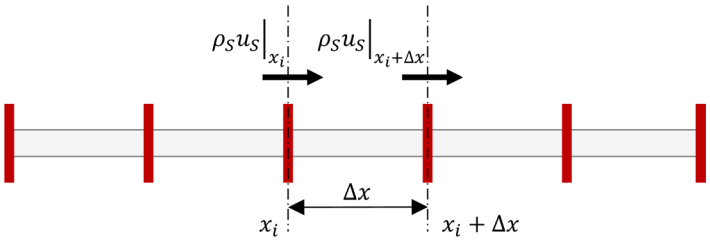

Figure 2-7: Schematic representation of the species conservation equation applied to a 1D domain along the horizontal direction of solids flow considered in this study.

The species conservation equation, in its transient form (Eq. [13]), describes the change in concentration of a given species over time and space [107]:

$$\frac{\partial \rho_s}{\partial t} = D_s \frac{\partial^2 \rho_s}{\partial x^2} - u_s \frac{\partial \rho_s}{\partial x} \quad [13]$$

The energy conservation equation expresses the heat balance, yielding a temperature profile across a domain, $T(x)$, as a function of the dispersion coefficient, the solids velocity, and the gas flow parameters included in the rightmost source term [107]. In its stationary form, it is described by:

$$0 = \lambda \frac{\partial^2 T}{\partial x^2} - \rho_s u_s (1 - \varepsilon_g) C_{p,s} \frac{dT}{dx} + \rho_g u_g C_{p,g} \frac{\Delta T}{H_b} \quad [14]$$

where the effective thermal conductivity of the bed is expressed as [55]:

$$\lambda = D_s (1 - \varepsilon_g) \rho_s C_{p,s} \quad [15]$$

2.4.3. CFD model

(i) Eulerian-Eulerian model

In the present study, the Eulerian–Eulerian model is employed, incorporating the kinetic theory of granular flow. **Table 2-3** summarizes the governing equations and constitutive relations used in the model.

Table 2-3: Governing equations and constitutive relations employed in the computational fluid dynamics (CFD) framework.

Conservation of mass equations:		
$\frac{\partial}{\partial t}\left(\varepsilon_g \rho_g\right) + \nabla \cdot \left(\varepsilon_g \rho_g \vec{u}_g\right) = 0$		[16]
$\frac{\partial}{\partial t}\left(\varepsilon_s \rho_s\right) + \nabla \cdot \left(\varepsilon_s \rho_s \vec{u}_s\right) = 0$		[17]
Momentum balance equations:		
$\frac{\partial}{\partial t}\left(\varepsilon_g \rho_g \vec{u}_g\right) + \nabla \cdot \left(\varepsilon_g \rho_g \vec{u}_g \vec{u}_g\right) = -\varepsilon_g \nabla P + \nabla \cdot \bar{\bar{\tau}}_g + \varepsilon_g \rho_g \vec{g} - \beta_{gs}\left(\vec{u}_g - \vec{u}_s\right)$		[18]
$\frac{\partial}{\partial t}\left(\varepsilon_s \rho_s \vec{u}_s\right) + \nabla \cdot \left(\varepsilon_s \rho_s \vec{u}_s \vec{u}_s\right) = -\varepsilon_s \nabla P - \nabla P_s + \nabla \cdot \bar{\bar{\tau}}_s + \varepsilon_s \rho_s \vec{g} + \beta_{gs}\left(\vec{u}_g - \vec{u}_s\right)$		[19]
Granular kinetic energy transport equation:		
$\frac{3}{2}\varepsilon_s \rho_s \left[\frac{\partial \theta_s}{\partial t} + \vec{u}_s \nabla \cdot \theta_s\right] = \bar{\bar{\tau}}_s : \nabla \vec{u}_s + \nabla \cdot \left(\kappa_{\theta_s} \nabla \theta_s\right) - \gamma_{\theta_s}$		[20]
Constitutive equations:		
Gas-phase stress tensor:	$\bar{\bar{\tau}}_g = -\varepsilon_g \left[\left(\xi_g - \frac{2}{3}\mu_g\right)(\nabla \cdot \vec{u}_g)\boldsymbol{I} + \mu_g\left(\nabla \vec{u}_g + \left(\nabla \vec{u}_g\right)^T\right)\right]$	[21]
Solids-phase stress tensor:	$\bar{\bar{\tau}}_s = -\varepsilon_s \left[\left(\xi_s - \frac{2}{3}\mu_s\right)(\nabla \cdot \vec{u}_s)\boldsymbol{I} + \mu_s(\nabla \vec{u}_s + (\nabla \vec{u}_s)^T)\right]$	[22]
Inter-phase momentum exchange coefficient [108,130–132]:	$\beta_{gs} = \frac{3}{4} C_D \frac{\varepsilon_s \varepsilon_g \rho_g \left\lvert \vec{u}_g - \vec{u}_s \right\rvert}{d_s} \varepsilon_g^{-2.65}$, for $\varepsilon_g > 0.8$	[23]
	$C_D = \begin{cases} \frac{24}{\varepsilon_g Re_s}\left[1 + 0.15\left(\varepsilon_g Re_s\right)^{0.687}\right], & Re_s < 1000 \\ 0.44, & Re_s > 1000 \end{cases}$	[24]
	$\beta_{gs} = 150 \frac{\varepsilon_s^2 \mu_g}{\varepsilon_g d_s^2} + 1.75 \frac{\varepsilon_s \rho_g \left\lvert \vec{u}_g - \vec{u}_s \right\rvert}{d_s}$, for $\varepsilon_g \leq 0.8$	[25]
Solids shear viscosity [133]:	$\mu_s = \mu_{s,c} + \mu_{s,k} + \mu_{s,f}$	[26]
Collisional viscosity [132]:	$\mu_{s,c} = \left[\frac{4}{5}\varepsilon_s \rho_s d_s g_0 (1+e)\left(\frac{\theta_s}{\pi}\right)^{\frac{1}{2}}\right]$	[27]
Kinetic viscosity [134]:	$\mu_{s,k} = \left[\frac{\rho_s d_s \sqrt{\theta_s \pi}}{6(3-e)}\left(1 + \frac{2}{5}(1+e)(3e-1)\varepsilon_s g_0\right)\right]$	[28]
Frictional viscosity [130]:	$\mu_{s,f} = \left[\frac{P_s \sin\varphi_f}{2\sqrt{I_{2D}}}\right]$	[29]
Solids bulk viscosity [108,132]:	$\xi_s = \frac{4}{3}\varepsilon_s^2 \rho_s d_s g_0 (1+e)\left(\frac{\theta_s}{\pi}\right)^{\frac{1}{2}}$	[30]
Solids pressure [108,132]:	$P_s = \rho_s \varepsilon_s \theta_s [1 + 2(1+e) g_0 \varepsilon_s]$	[31]
Radial distribution function [79,108,132]:	$g_0 = \left[1 - \left(\frac{\varepsilon_s}{\varepsilon_{s,max}}\right)^{\frac{1}{3}}\right]^{-1}$	[32]
Granular conductivity [132,135]:	$\kappa_{\theta_s} = \frac{150 \rho_s d_s \sqrt{\theta_s \pi}}{384(1+e) g_0}\left[1 + \frac{6}{5}\varepsilon_s g_0 (1+e)\right]^2 + 2\rho_s \varepsilon_s^2 d_s (1+e) g_0 \sqrt{\frac{\theta_s}{\pi}}$	[33]
Collision energy dissipation [130]:	$\gamma_{\theta_s} = \frac{12(1-e^2) g_0}{d_s \sqrt{\pi}} \rho_s \varepsilon_s^2 \sqrt{\theta_s^3}$	[34]

(ii) Lagrangian particle tracking

Lagrangian particle tracking (LPT) is used to analyze individual particle trajectories by solving the equations of motion along their paths, as summarized in **Table 2-4**. This method requires local pseudo-fluid properties, such as time-resolved velocity, volume fraction, density, and viscosity, which are extracted from the gas–solids model outputs of the preceding two-fluid (Eulerian–Eulerian) simulations. The resulting pseudo-field database provides the necessary input for LPT calculations, enabling detailed trajectory analysis based on established methodologies [136–138]. A key assumption in the Lagrangian tracking applied in this work is the use of a one-way coupling scheme, i.e., tracers are modeled as passive, point-like particles that do not influence the gas or solid flow fields. Accordingly, the force balance includes only the weight, buoyancy, and drag from the surrounding pseudo-fluid. Tracer interactions with bed boundaries are treated as perfectly elastic collisions.

Table 2-4: Governing equations for Lagrangian particle tracking (LPT) in monodisperse gas-solids suspensions.

Pseudo-fluid properties: $\phi_{pf} = \varepsilon_g \phi_g + \varepsilon_s \phi_s$ where ϕ=u,ρ,μ	[35]
Particle equations of motion: $\frac{dx_{lp}}{dt} = \vec{u}_{lp}$	[36]
$m_{lp} \frac{d\vec{u}_{lp}}{dt} = F_D + F_B$	[37]
Particle buoyancy force: $F_B = (\rho_{lp} - \rho_{pf}) \frac{\pi d_{lp}^3}{6} g$	[38]
Particle drag force: $F_D = \frac{\pi}{8} C_{D,lp} Re_{lp} d_{lp} \mu_{pf} (u_{lp} - u_{pf})$	[39]
Particle drag coefficient: $C_{D,lp} = \left(0.63 + \frac{4.8}{Re_{lp}^{0.5}}\right)^2$	[40]

3. Methodology

This chapter is organized into five sections. **Section 3.1** presents the methodology used for fluid-dynamic scaling. **Section 3.2** describes the experimental setup, including various configurations designed to drive horizontal solids convection. **Section 3.3** introduces the experimental methods used to characterize solids flow by determining key flow parameters. **Section 3.4** details the specific CFD model settings employed in this work, the analysis of simulated data, and the validation of the simulations. Lastly, **Section 3.5** outlines the experimental matrix, providing an overview of the variables and operational ranges explored in this study.

3.1. Fluid-dynamic scaling

Fluid-dynamic downscaling enables the investigation of gas–solid flow phenomena in large-scale, high-temperature, or high-pressure systems by reproducing their flow behaviors in laboratory-scale units under ambient conditions. These cold-flow models provide enhanced operational and geometric flexibility, facilitate the implementation of diagnostic techniques, and permit safer, more cost-effective experimentation. The scaling methodology adopted in this work follows Glicksman's simplified set of scaling laws [139,140]. Thus, the following dimensionless numbers must be kept as similar as possible between the full-scale (hot) unit and the downscaled model.

$$\frac{u_0^2}{gD_b}, \frac{\rho_s}{\rho_g}, \frac{u_0}{u_{mf}}, \frac{G_S}{\rho_S u_0}, \frac{L_1}{L_2}, \varphi, PSD$$

This set of scaling laws is a validated experimental method [140–142] that substitutes the Reynolds number in the original full set of scaling laws [139] with the u_0/u_{mf} ratio. This substitution enables greater flexibility in length scaling, as it depends on the minimum fluidization velocity ratio for the gas-solids pair:

$$[L] = \frac{L_{cold}}{L_{hot}} = \frac{\left[\frac{u_{mf}^2}{g \cdot Fr}\right]_{cold}}{\left[\frac{u_{mf}^2}{g \cdot Fr}\right]_{hot}} = \left(\frac{[u_{mf}]_{cold}}{[u_{mf}]_{hot}}\right)^2 \quad [41]$$

The experimental apparatus used in this work was designed with a length scaling factor of 0.12. This choice was influenced by the laboratory's constraints, including airflow capacity and the availability of suitable bed material. The experimental unit is designed to replicate large-scale hot conditions, in which silica sand with a mean size of 950 μm is fluidized with flue gases at 800°C. The scaling of biomass fuel particles (wood chips) with two different densities, 415 kg/m³ and 897.5 kg/m³, is also considered in this work. **Table 3-1** provides a comparison of the cold-flow model and its corresponding high-temperature reference system with respect to the operating conditions, bed material (bulk-phase), and fuel particles (lean-phase).

Table 3-1: Main parameters used in the fluid-dynamically scaled model.

Parameter	Units	Hot unit	Cold model
Temperature	℃	800	24
Fluidization gas	-	Air or flue gases	Air
Gas density	kg/m³	0.359	1.187
Gas viscosity	m²/s	1.4×10^{-4}	1.54×10^{-5}
Bed geometry	m	L_{hot}	$0.12L_{hot}$
Bed material	-	Silica sand	Bronze
Particle density, bulk solids	kg/m³	2,650	8,770
Mean particle diameter, bulk solids	μm	950	125
Particle density, lean solids	kg/m³	415, 897.50	1,370, 2,970
Particle size, lean solids	mm	Ø20×30	Ø2×3
Gas superficial velocity	m/s	$u_{0,hot}$	$\sqrt{0.12}u_{0,hot}$
Minimum fluidization velocity	m/s	0.31	0.074
Solids mean velocity	m/s	$u_{s,hot}$	$\sqrt{0.12}u_{s,hot}$
Solids dispersion coefficient	m²/s	$D_{s,hot}$	$0.042D_{s,hot}$

3.2. Experimental setup

The cold-flow model (CFM) used in this study, depicted in **Figure 3-1**, operates under bubbling fluidization conditions. The apparatus, which is constructed from acrylic glass, has a footprint of 0.5 × 0.4 m² and a height of 0.5 m. A central rectangular section, referred to as the "centre box," forms a closed annular channel in which fluidized solids circulate in a clockwise direction. As illustrated in **Figure 3-1a (**top view**)**, the annular channel comprises a transport zone, where the solids are fluidized in the bubbling regime, and a conveying zone with independently controlled airflow, in which a crossflow of solids is induced by high-velocity nozzles and baffles (specific configurations are presented below).

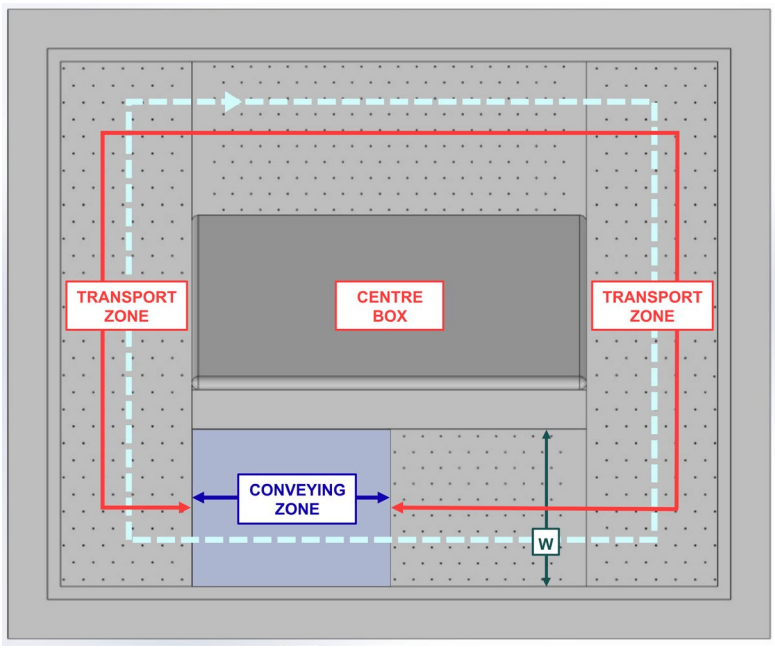

(a) Top view

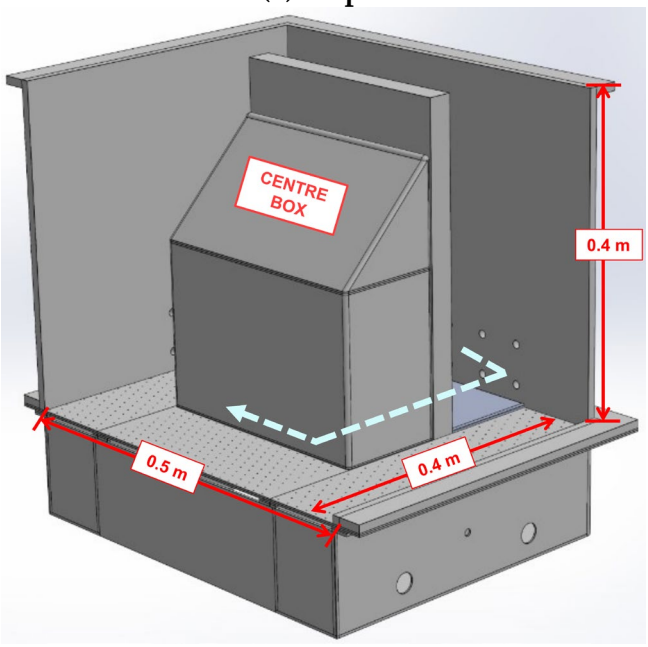

(b) Isometric view

Figure 3-1: Fluid-dynamically down-scaled model of the experimental setup. The induced crossflow of solids is indicated by a dashed light-blue arrow.

This study evaluates five configurations for their effectiveness in conveying solids horizontally, as illustrated in **Figure 3-2**: (a) free solids splashing; (b) confined solids splashing; (c) slugging; (d) solids entrainment; and (e) directed gas injection.

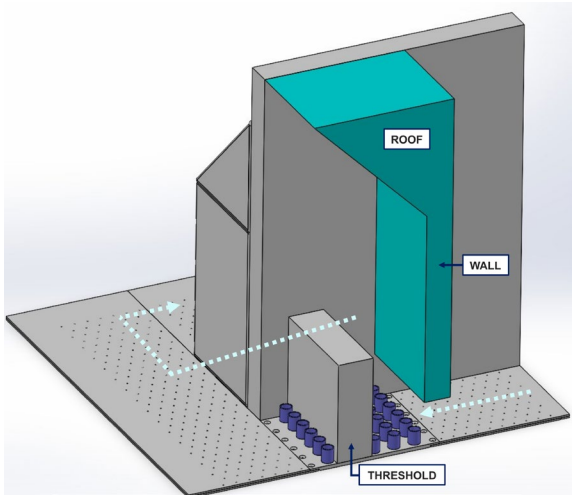

(a) Free solids splashing

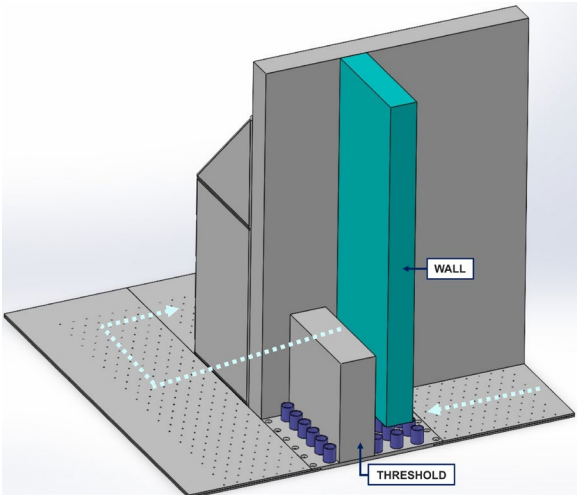

(b) Confined solids splashing

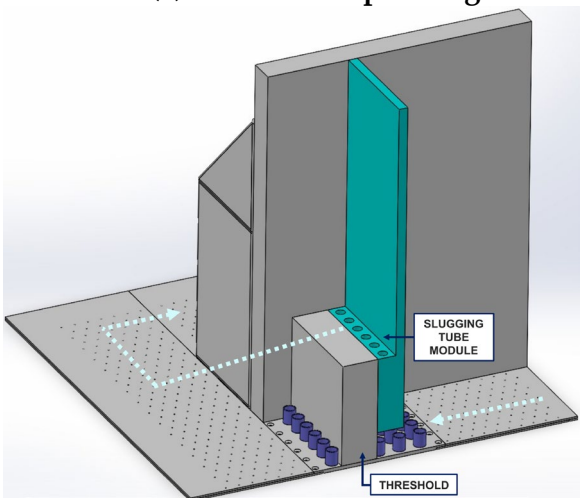

(c) Slugging

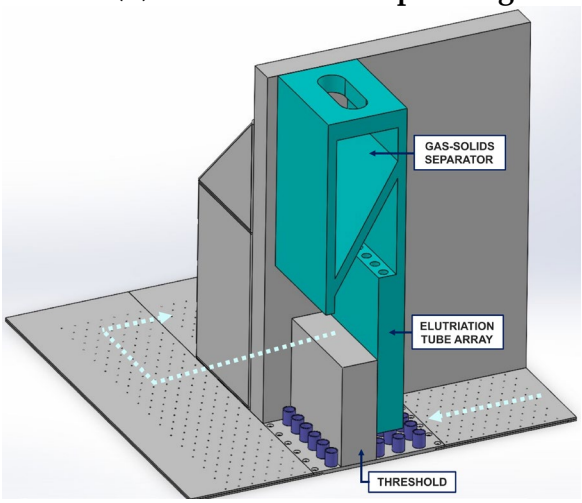

(d) Solids entrainment

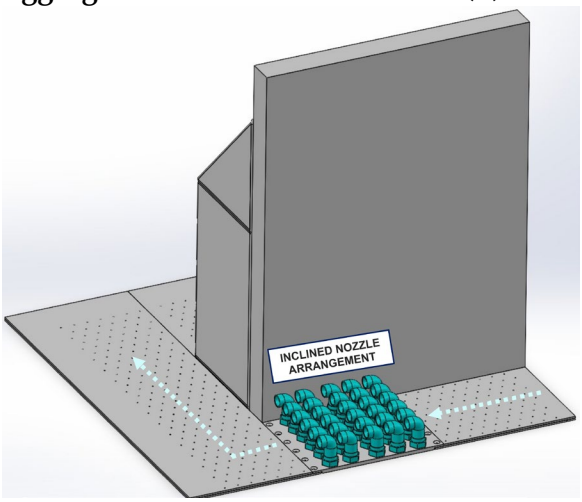

(e) Directed gas injection

Figure 3-2: Configurations for solids conveying tested in this work.

Each configuration is based on a distinct gas–solids interaction mode and was designed to explore different mechanisms for promoting horizontal transport. The specific operating principles and setup details are presented in **Paper II** [143]. The **free solids splashing** configuration operates in the bubbling fluidization regime, where particles in the dense phase are intermittently lifted by rising gas bubbles. When these bubbles burst at the surface, they eject solids into the freeboard, resulting in ballistic backmixing with high particle velocities and a wide range of ejection angles. The **confined solids splashing** configuration employs turbulent fluidization, which is characterized by high kinetic energy and chaotic particle motion. The narrower lateral confinement compared to the free solids splashing configuration enhances horizontal transport through turbulence- and buoyancy-driven movement. The **slugging** configuration promotes the coalescence of gas bubbles into large slugs. The rise and collapse of these slugs, in combination with gravitational settling, generate recirculation and pronounced pulsating flow within the bed. The **solids entrainment** configuration relies on a high-velocity gas to lift particles from the dense bed, particularly under fast fluidization and pneumatic regimes. As the gas velocity increases, solids are entrained into the dilute phase, necessitating separation and recycling to sustain a continuous flow. The **directed gas injection** configuration introduces fluidizing gas through inclined nozzles, imparting horizontal momentum to the bubbles and solids. Rows of angled nozzles are used to induce and control the horizontal movement of solids.

The solids velocity, and consequently the solids conveying rate, is determined using the magnetic solids tracing technique (see **Section 3.3.4**). The pressure drops experienced by the gas when injected into the conveying module and by the solids suspension as it moves along the transport channel are measured to analyze the efficiency of each configuration in converting gas compression energy (see Eq.[3]) into net solids flow energy (see Eq.[2]).

3.3. Methods for solids flow characterization

In this study, five measurement techniques were employed to quantify the key parameters of the solids flow, as detailed in the following subsections. **Table 3-2** summarizes these methods, specifying the measurement approach, technique, measured variables, equations or analytical tools used, and the extracted variables.

Table 3-2: Overview of measurement methods, including techniques, analytical tools, and solids flow parameters studied.

Measurement method	Measurement technique	Measured variable	Equation (or) analytical tool		Extracted variables
Integral mass accumulation	Weight difference	Mass flow rate	$u_s = \frac{\Delta m}{\Delta t}\frac{1}{\rho_{bulk} HW}$		u_s
Differential mass accumulation	Pressure sampling	Dynamic pressure gradient	$u_s = \frac{dP}{dt}\frac{A_{Accumulation}}{g}\frac{1}{\rho_{bulk} HW}$		u_s
Thermal tracing	Thermography	Temperature field (2D)	Transport equation (energy conservation): $0 = \lambda\frac{\partial^2 T}{\partial x^2} - \{\rho_s u_s(1-\varepsilon_g)C_{p,s}\}\frac{dT}{dx} + \{\rho_g u_g C_{p,g}\}\frac{\Delta T}{H_b}$ where, $D_s = \frac{\lambda}{(1-\varepsilon_g)\rho_s C_{p,s}}$		u_s, D_s
Magnetic tracing	Inductance	Transient tracer concentration profile	Transport equation (species conservation): $\frac{\partial C_i}{\partial t} = D_s\frac{\partial^2 C_i}{\partial x^2} - u_s\frac{\partial C_i}{\partial x}$		u_s, D_s
			Compartment model: $C_{i,out}(t) = C_{i,in}(t) + \frac{m_t}{Q_t}\left\{\frac{1}{\tau(1-i_d)}\frac{{N_{CSTR}}^{N_{CSTR}}}{(N_{CSTR}-1)!}\left[\frac{(t-\tau_{PFR})}{\tau(1-i_d)}\right]^{N_{CSTR}-1}\right\} e^{-N_{CSTR}\frac{(t-\tau_{PFR})}{\tau(1-i_d)}}$		i_d, N_{CSTR}, τ_{PFR} & τ
Crossflow fluidized bed rheometry	Inductance	Transient tracer concentration profile	Transport equation (species conservation): $\frac{\partial C_i}{\partial t} = D_s\frac{\partial^2 C_i}{\partial x^2} - u_s\frac{\partial C_i}{\partial x}$		u_s
	Pressure sampling	Steady-state pressure gradient	Fanning friction factor:	$\frac{\Delta P}{\Delta L} = \frac{2 f_F \rho_{fluid} {u_s}^2}{D_h}$	f_F, τ_w, k^*, n^*
			Wall shear stress:	$\tau_w = D_h \cdot \frac{\Delta P}{\Delta L}$	
			Power-law model:	$\tau_w = k^*\left(\frac{8u_s}{D_h}\right)^{n^*}$	

3.3.1. Integral mass accumulation

The mean solids velocity is determined by directly measuring the mass of solids that is collected in a container over a specified time interval. The experimental setup, shown in **Figure 3-3**, comprises two collection boxes: Box 1, which is easily removable and serves as the primary measurement device; and Box 2, which is securely attached to the unit walls to capture any minor leakage of solids. The opening of Box 1 remains closed (via a sliding wall) until stable fluidization conditions are established in both the transport and conveying zones. The mean solids mass flow is calculated from the collected mass and the collection duration. Subsequently, the mean horizontal solids velocity is obtained by dividing the mass flow rate by the effective cross-sectional flow area in the transport zone.

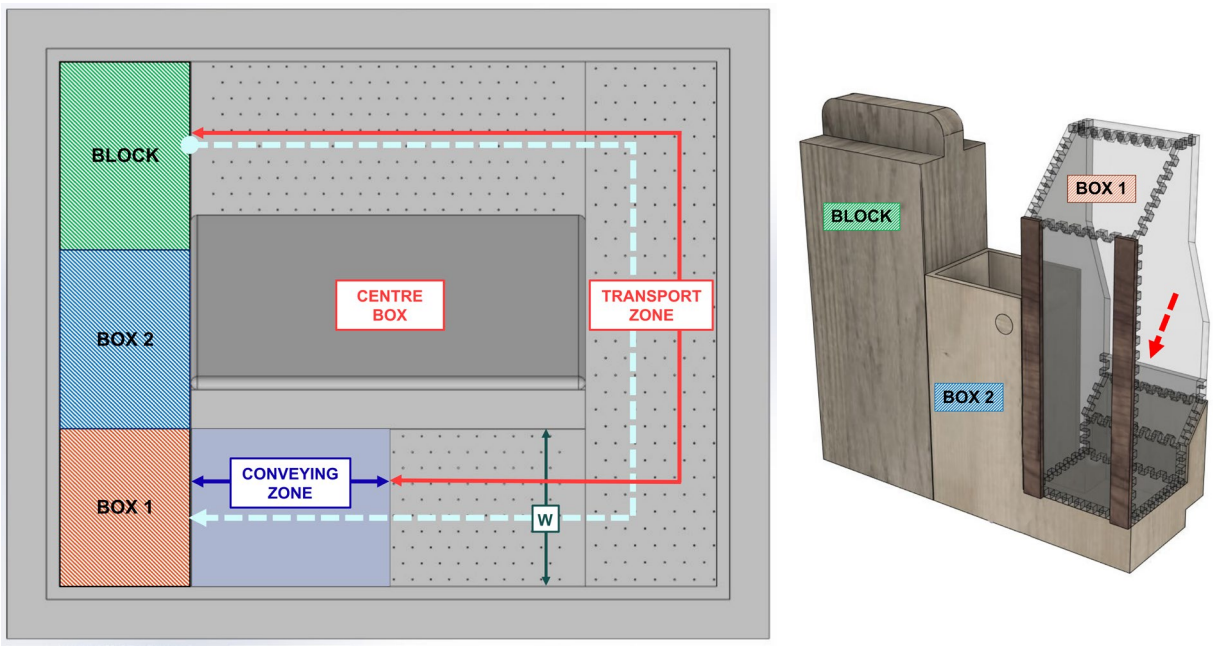

(a) Top view of the unit setting **(b) Box-block arrangement used in the transport zone**

Figure 3-3: Experimental setup used for integral mass accumulation.

The time-averaged solids velocity can be determined from:

$$u_s = \frac{\Delta m}{\Delta t}\frac{1}{\rho_{bulk} HW} \quad [42]$$

This method is limited by its inherently unsteady operation. The progressive reduction in the fluidized solids inventory decreases the bed height, thereby altering the solids flow rate over time. In addition, the presence of the collection boxes reduces the total solids inventory and available volume within the system, making the experimental conditions less representative of a standard circulating operation.

3.3.2. Differential mass accumulation

The differential mass accumulation method also involves the accumulation of conveyed solids, while permitting continuous assessment. This is achieved by fluidizing the accumulation area and monitoring the resulting transient pressure increase, which corresponds to the rise in bed height. Once steady-state conditions are established, a vertical wall separator is inserted into

the transport zone (as illustrated in **Figure 3-4a**), dividing the system into an accumulating bed (blue section) and an emptying section (green section).

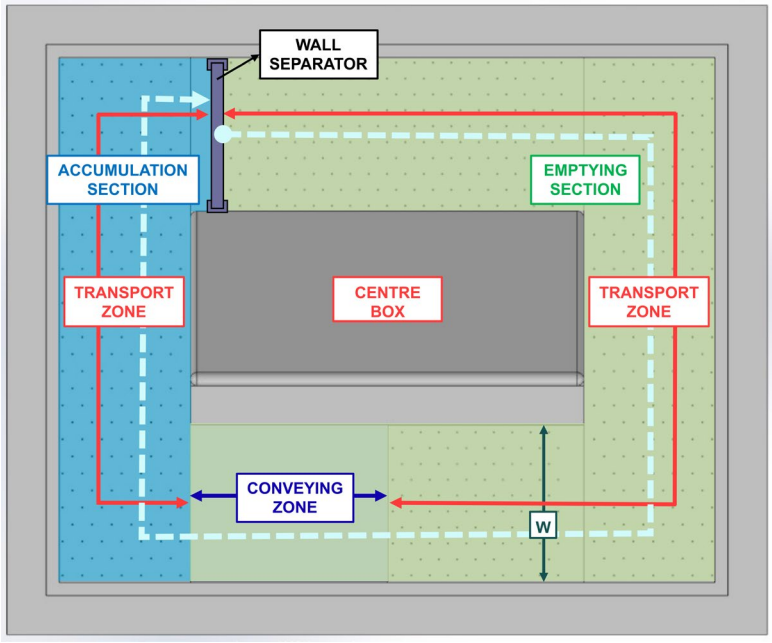

(a) Top view of the unit setting

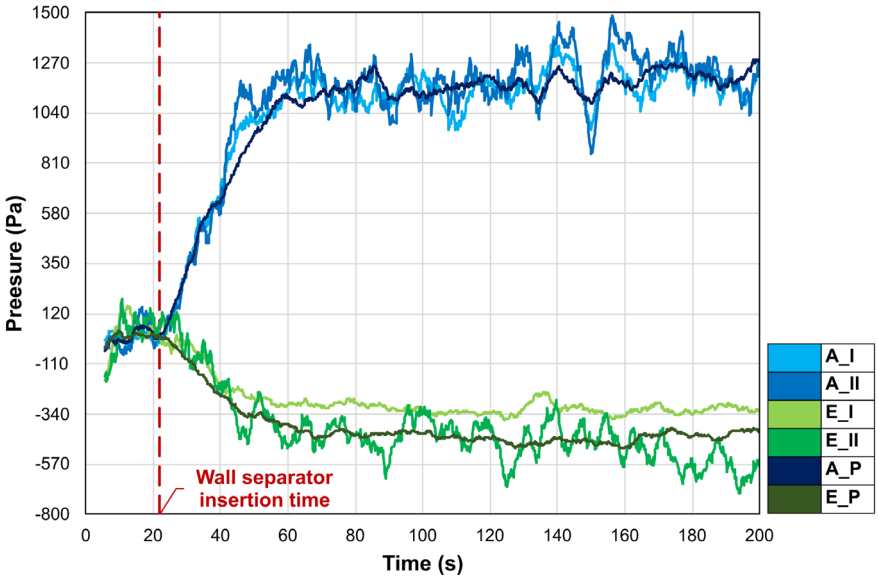

(b) Transient pressure profiles

Figure 3-4: Experimental setup used for the differential mass accumulation method. Conditions: FN_{TZ}, 3; H, 0.08 m; Q_{CZ}, 0.0143 m³/s. A = accumulation; E = emptying; P = plenum. Pressure probes I/II are located at 7.5 cm and 5.25 cm above the plate, respectively.

The observed pressure change 'dP' in the accumulating bed is then used to determine the mass accumulation rate and, subsequently, the solids velocity:

$$u_s = \frac{dP}{dt}\frac{A_{Accumulation}}{g}\frac{1}{\rho_{bulk}HW} \qquad [43]$$

Pressure is measured at three points in the accumulating and emptying beds: within the air plenum and at 5.25 cm and 7.5 cm above the gas distributor. Representative pressure transients are shown in **Figure 3-4b**. Stabilization of the pressure signals indicates maximum

accumulation of the material. The mean solids velocity is calculated from the time derivatives of pressure during intervals with a constant gradient, using data from the accumulating bed.

This method offers operational simplicity and enables time-resolved measurements of accumulation rates, thereby correcting for underestimation caused by decreasing mass flow over time. Accurate pressure measurements are crucial, especially at low solids flow rates, where pressure changes are subtle. At higher flow rates, minor leakage between the accumulation and discharge zones can occur through wall gaps, although visual inspection indicates that these losses are negligible. Nevertheless, since the process is inherently unsteady, some level of inaccuracy is unavoidable.

3.3.3. Thermal tracing

The non-intrusive method of thermal tracing determines the mean solids velocity by relating it to the bed's horizontal heat transport capacity. A temperature gradient is established along the solids flow by fluidizing the bed with air at 80°C in a designated heating zone (**Figure 3-5a**), while the remaining sections contain ambient air. Thermal imaging captures a 2D temperature field at the bed surface, which is integrated along the y-axis to yield a 1D temperature profile. A steady-state, 1D energy equation, discretized using the finite volume method, is then fitted to the measured temperature profile, $T(x)$, to estimate the horizontal solids velocity (see Eq. [14]). For each experiment, the solids dispersion coefficient, D_S, is first determined under bubbling conditions without a crossflow(Eq. [15]), such that the convection parameter, λ, remains the sole unknown. **Figure 3-5b** presents an examples of the experimental and modeled temperature profiles for the determination of solids dispersion (red curves) and convection (blue curves). Boundary conditions are defined by in-bed temperature measurements at the start (T_0) and end (T_L) of the measuring zone.

The lateral dispersion coefficient of the solids is assumed to be constant for each fluidization velocity and bed height, and it does not depend on the horizontal solids flow rate. Subsequent analysis revealed that this assumption leads to an overestimation of the calculated mean solids velocity; further discussion of this limitation is provided in **Section 4.1**.

The temperature field exhibits inherent fluctuations due to the bed dynamics, e.g., variations in bed height and bubble eruptions at the surface, as well as changes in the ambient temperature and heater control. These fluctuations may fall within the thermographic camera's sensitivity range (approximately 0.04 K), potentially affecting measurement accuracy. However, the main limitation of this method at high solids flow rates is the reduced temperature gradient across the bed, which decreases the precision with which the solids velocity can be inferred. In addition, at high flow rates, the increased thermal inertia and wall friction may influence the surface temperature of the fluidized particles. While particle emissivity is generally stable, changes in surface properties or bed composition can further affect the accuracy of thermographic measurements.

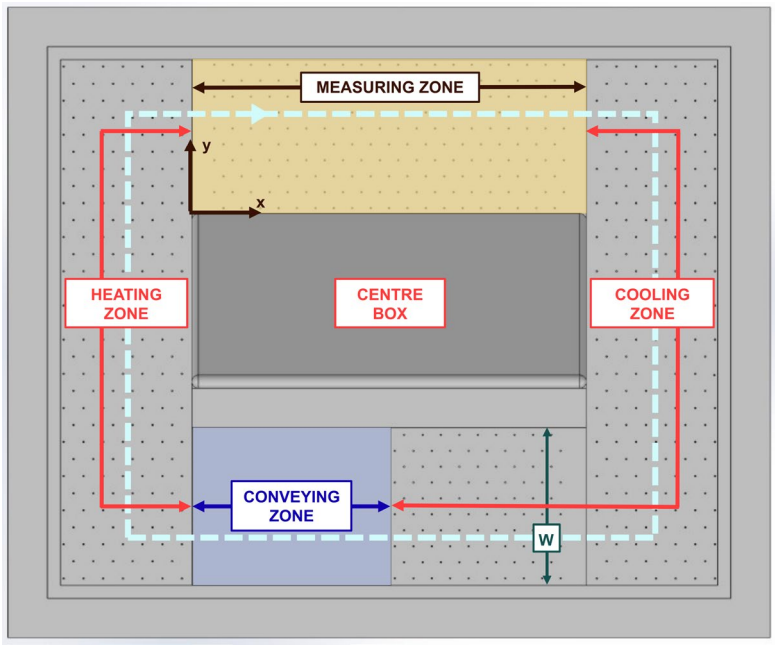

(a) Top view of the unit setting

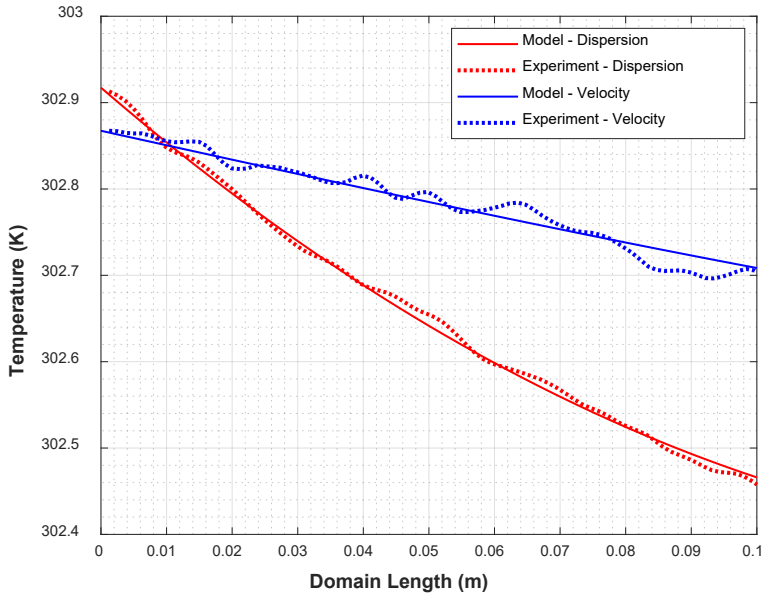

(b) Temperature profiles in the absence/presence of macroscopic solids convection.

Figure 3-5: Experimental setup used for thermal tracing and the associated results. Conditions: FN_{TZ}, 3; H, 0.08 m; Q_{CZ}, 0.0143 m³/s. The temperature scale is in Kelvin.

3.3.4. Magnetic solids tracing

(i) Bulk-phase solids

With this technique, the mean solids velocity is determined from a tracer-pulse measurement. A small amount of magnetic tracer material, selected for its similarity in fluid dynamics to the bed material, is introduced into the system, and its concentration is subsequently tracked over time at varying downstream locations using inductance coils. **Table 3-3** lists the physical properties and dimensionless particle sizes (Archimedes numbers) of the materials employed.

Table 3-3: Comparison of the bed material and magnetic tracer.

Parameter	Unit	Bed solids	Tracer
Material	-	Bronze	Fe-based alloy
Particle density	kg/m^3	8,770	7,988
Bulk density	kg/m^3	5,522	4,520
Particle size distribution d_{10}-d_{50}-d_{90}	µm	80-112-132	25-69-123
Sauter mean diameter (d_{32})	µm	126	102
Archimedes' number, Ar$^{1/3}$	-	8.386	6.127
Minimum fluidization velocity	m/s	0.074	0.039
Magnetic susceptibility	-	0	0.9

Four inductance coils arranged around the perimeter of the cross-sectional flow area are positioned within the measuring zone (see **Figure 3-6a**) to monitor changes in tracer concentration over time. A batch of iron-based tracer is injected upstream of the first coil (C1), as shown in **Figure 3-6**. The resulting transient concentration signals are recorded and used to determine the tracer residence time distribution, as well as the horizontal solids flow velocity and dispersion coefficient. **Figure 3-6b** illustrates typical transient concentration signals obtained from coils C1 to C4 during a tracer experiment.

Limitations of this method include the time-consuming separation of magnetic tracer material after each experiment and the difficulty of precisely matching the tracer's physical properties to those of the bed material. Additional errors may arise from tracer segregation at the unit corners and weaker coil signals at low solids circulation rates.

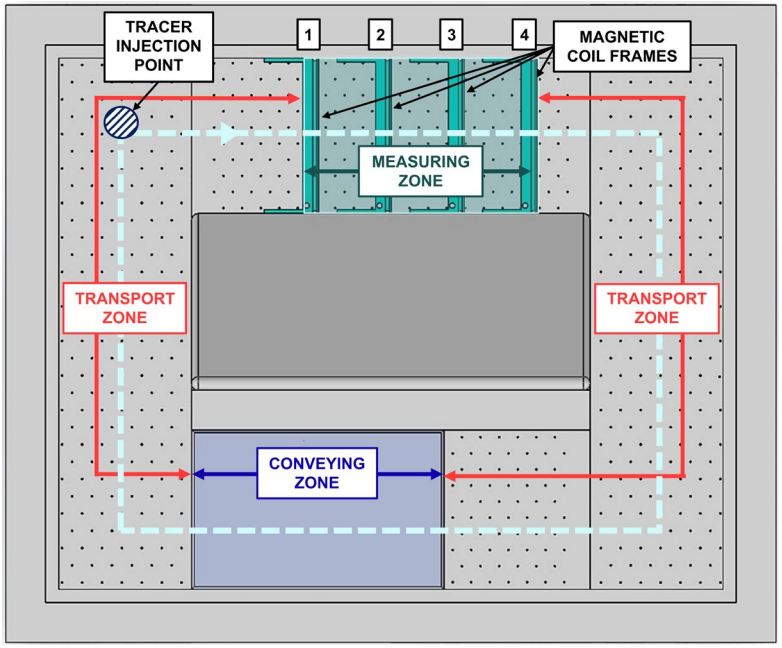

(a) Top view of the unit setup

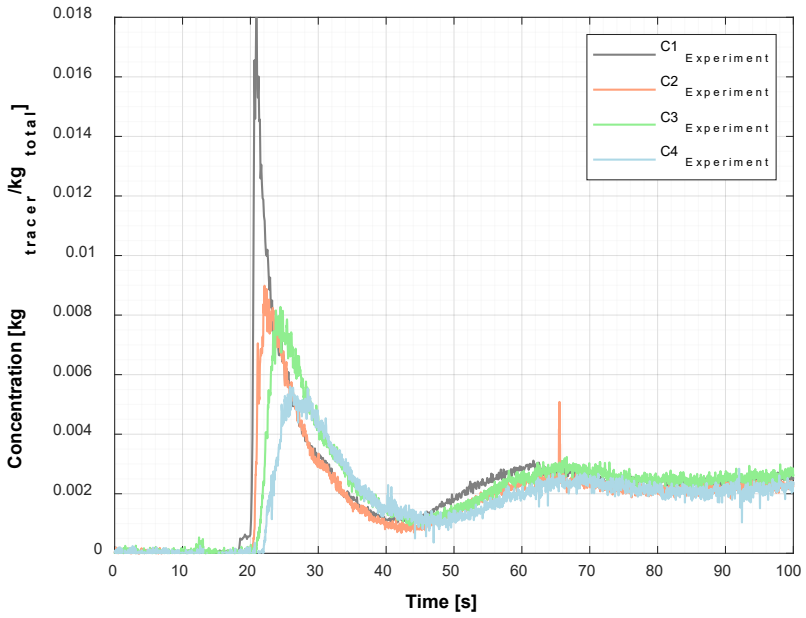

(b) Transient profiles of the measured tracer concentration at each coil

Figure 3-6: Experimental setup for the magnetic solids tracing method and corresponding transient concentration profiles. Conditions: FN_{TZ} , 3; H, 0.08 m; Q_{CZ} , 0.0143 m³/s.

Data from the magnetic solids tracing experiments were analyzed using two approaches: fitting to the transient convection–dispersion model (**Section 2.4.2**) and fitting to a compartment model (**Section 2.4.1**), each of which enabled investigation of distinct aspects of flow behavior, as shown in **Figure 3-7**.

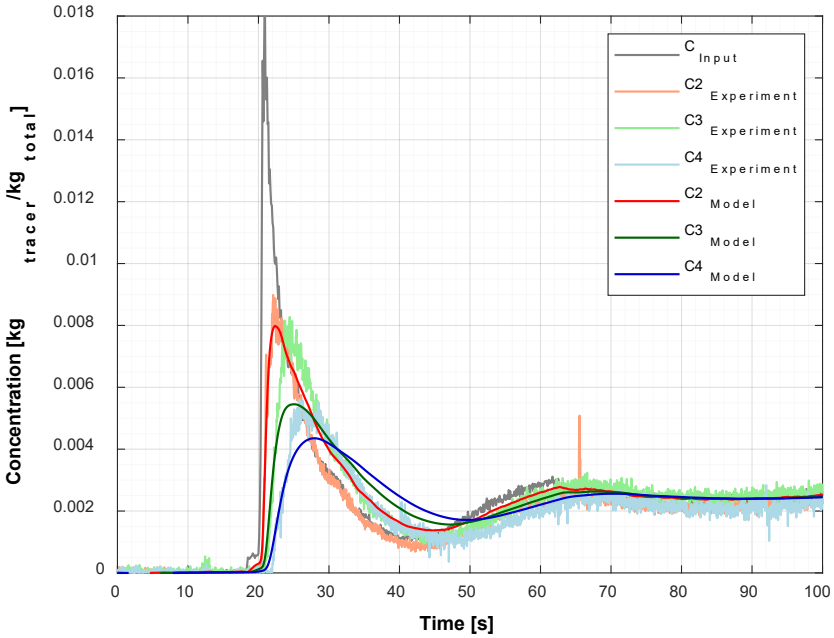

Fitted variables: u_s=1.35×10^{-2} m/s, D_s=1.64×10^{-3} m^2/s

(a)

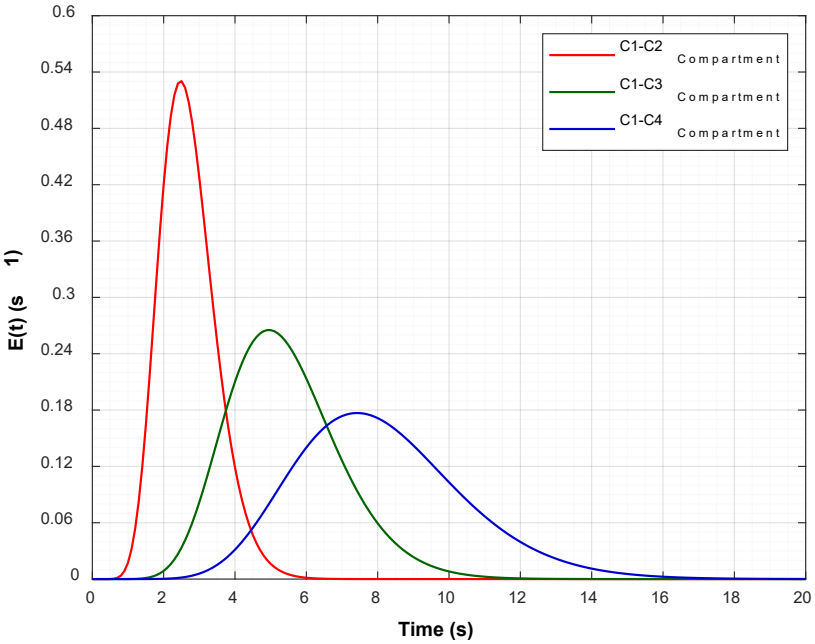

Fitted variables: i_d=0.07, N_{CSTR}=6, τ=5.16 s, τ_{PFR}=0.3 s

(b)

Figure 3-7: Analysis of bulk-phase solids using magnetic solids tracing. (a) Transient concentration profiles with fitting to the convection-dispersion model. (b) Solids RTD curves from compartment model fitting. Conditions: FN_{TZ}, 3; H, 0.08 m; Q_{CZ}, 0.0143 m^3/s.

In the first approach, the transient convection–dispersion equation (Eq. [13]) is fitted to experimental data to estimate the solids' mean velocity and dispersion coefficient. The tracer mass balance is solved numerically using the finite volume method with a fully implicit discretization for stability and accurate time integration. The hybrid differencing scheme combines the precision of central differencing in uniform regions with the stability of upwind differencing in areas of steep gradients. The modeled domain extends from coil 1 to the boundary between the transport zone and the solids-conveying section. Boundary conditions include a transient Dirichlet condition at coil 1 (based on the measured tracer concentration) and a zero-gradient condition at the conveying section inlet, simulating a wall that permits convection but not dispersion. **Figure 3-7a** displays typical model fits, where the sharp tracer peaks at all coils gradually broaden downstream due to dispersion, eventually converging to a uniform concentration, indicating complete tracer mixing in the circulating loop.

In the second approach, compartment model parameters are determined by non-linear fitting of the model output (Eq. [11]) to the measured tracer concentrations at each coil. The signal from coil 1 serves as the model input, with fitting performed to minimize discrepancies between the modeled and measured signals at coils 2–4. In addition, a robust fitting strategy tackles multiple local optima by varying the initial parameter estimates. This process yields the best-fit parameters for each experiment, allowing calculation of the residence time distribution (Eq. [12]). The flow rate ($Q_t = V/\tau$), with τ determined from the first moment of $E(t)$, is used as the model input, and the fitting loop is repeated until convergence is achieved. **Figure 3-7b** presents the RTD curves derived from the compartment model analysis, illustrating the shift and broadening of the distributions along the transport zone. This broadening reflects both an increase in the mean residence time and a broader distribution, driven by increased dispersion as the tracer moves through the system.

(ii) Lean-phase solids

The transport characteristics of the lean-phase solids were investigated using materials of two different densities, representing distinct stages of biomass conversion: fresh biomass (high-density material) and devolatilized biomass (low-density material). **Table 3-4** summarizes the physical properties of the lean-phase solids used, and compares them to those of fuel particles under hot, large-scale conditions.

A global volume fraction of 9 vol% was used for the lean-phase solids, corresponding to 1.1 wt% for the low-density solids and 2.5 wt% for the high-density solids. These values are similar to typical fuel fractions observed during large-scale, high-temperature operation (1–5 wt%). For each test, a batch of magnetic tracer with properties (size, density) identical to the lean-phase solids was added, following the measurement technique described above. The tracer concentration was approximately 0.12–0.16 wt% of the lean-phase.

The transient concentration profiles obtained (see **Figure 3-8**) exhibit well-defined peaks and progressive profile broadening across the four coils as the tracer moves along the transport channel. The transient concentrations of the magnetic lean-phase tracer were analyzed using the transient convection–dispersion model (Eq. [13]), in line with the approach used for bulk-phase solids. A notable difference between the lean-phase solids and bulk solids is that, after uniform distribution is achieved, persistent signal fluctuations are observed. This is likely due to the tendency of lean-phase solids to aggregate near the bed surface, where they are affected by bubble eruptions. Nonetheless, the model fitting remained robust.

Table 3-4: Comparison of the properties of lean-phase solids used in the experiment with those of simulated fuel particles.

Parameter	Unit	Fuel particles	Lean-phase particles	Tracer particles
Material	-	Wood chips	Polyamide PA 6 – low density PA 12 – high density	PA 66 with magnetic filler – low density PPS with magnetic filler – high density
Conversion stage: Devolatilized biomass				
Particle density	kg/m³	414	1,360	1,370
Bulk density	kg/m³	233.5	658	773
Particle size	mm	20×30	2×3	2×3
Magnetic susceptibility	-	0	0	0.04
Conversion stage: Fresh biomass				
Particle density	kg/m³	897.50	2,910	2,970
Bulk density	kg/m³	342	1,483	1,131
Particle size	mm	20×30	2×3	2×3
Magnetic susceptibility	-	0	0	0.32

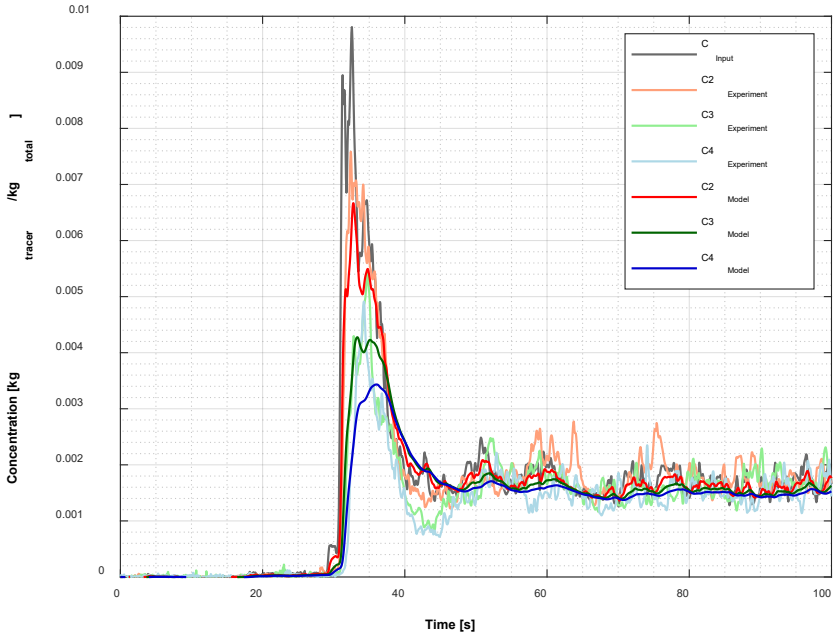

Fitted variables: u_s=6.93×10^{-4} m/s, D_s=5.99×10^{-3} m^2/s

Figure 3-8: Transient tracer concentration profiles for lean-phase solids measured by magnetic tracing, using convection–dispersion model fitting. Conditions: $\rho_{s,lean}$, 2,970 kg/m³; FN_{TZ}, 3; H, 0.08 m; Q_{CZ}, 0.0143 m³/s.

3.3.5. Crossflow fluidized bed rheometry

The measurements of solids velocity and horizontal pressure drop across the transport channel are central to quantitative mechanistic analyses of frictional losses and the bed's rheological properties. The solids velocity was determined using magnetic solids tracing, with the coil arrangement shown in **Figure 3-9a**, positioned just downstream of the injection probe. Two pressure probes were installed within the measurement zone—one upstream and one downstream of the coil array—as illustrated in **Figure 3-9a**. The channel width was varied in this study by adjusting the width of the central box, as depicted in **Figure 3-9b**.

Based on the pressure and velocity data, the Fanning friction factor and wall shear stress were calculated using Eqs. [4] and [5], respectively. The relationship between wall shear stress and apparent shear rate for the gas-solids suspension was then established using the power-law model (Eq. [7]), enabling determination of the flow behavior and consistency indices. Finally, the $\mu(I)$ constitutive law (Eq. [9]) was applied to quantify the bed's frictional behavior, using the macroscopic friction coefficient $\mu(I)$ derived from the calculated wall shear stress.

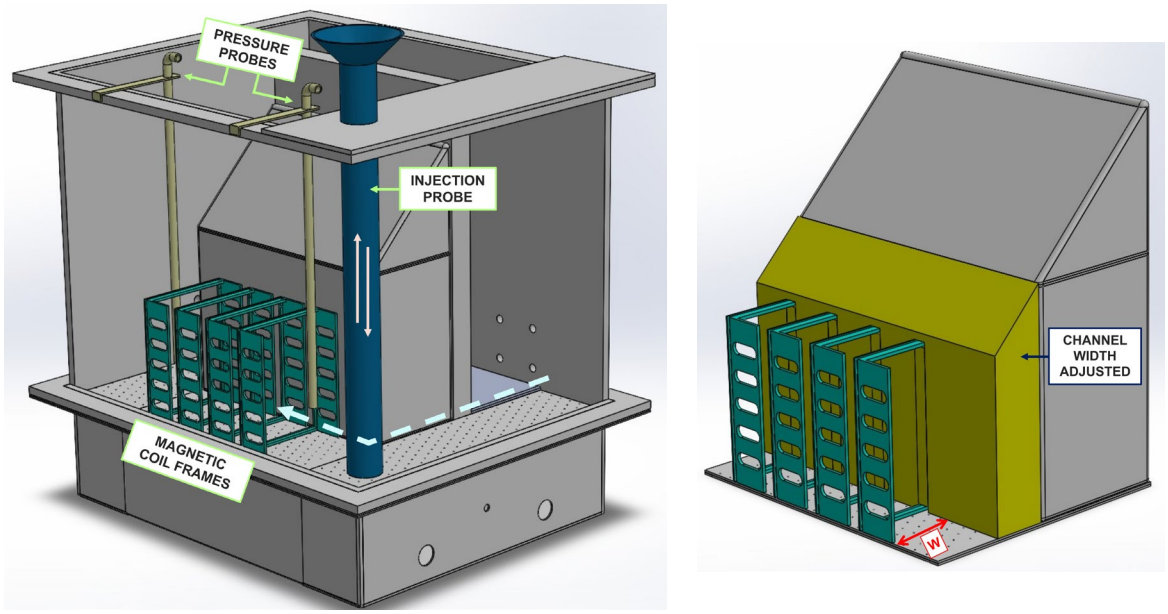

(a) **(b)**

Figure 3-9: Schematic of the CFM setup designed for the study of frictional losses in the direction of the solids crossflow, indicating: (a) the pressure probe positions in the measuring zone; and (b) the channel width adjustments.

3.4. CFD Model

3.4.1. Simulation setting

The 3D-CFD simulations for solids in the bulk phase were conducted in ANSYS Fluent, to investigate eight conditions that resulted from variations in three operational parameters: static bed height, H (0.08 m, 0.10 m); air volumetric flow rate in the conveying zone, Q_{CZ} (2.58×10^{-3} m³/s, 14.3×10^{-3} m³/s); and fluidization number in the transport zone, FN_{TZ} (1.83, 3). Each simulation encompassed the entire gas–solids system and represented 30–40 seconds of real process time, depending on the condition tested. Details of the computational model parameters are provided in **Table 3-5**.

Table 3-5: Summary of parameters used in the CFD model.

Model parameter		Setting
Bed geometry dimension [3D] (m)		0.5 × 0.4 × 0.5
Settled bed height (m)		0.08, 0.10
Bed inventory (kg)		63.5, 79.3
Mesh size (m)		0.004
Mesh resolution, $\Delta x/d_s$		10–20
Inlet boundary condition		Velocity
Outlet boundary condition		Pressure
Wall boundary condition		No slip
Velocity inlet (transport zone) (m/s)		0.14, 0.23
Velocity inlet (conveying zone) (m/s)		0.26, 1.48
Solid		Bronze
Particle diameter (μm)		125
Particle density (kg/m^3)		8,770
Friction packing limit		0.61
Initial solids volume fraction		0.607
Maximum packing limit, $\varepsilon_{s,max}$		0.63
Angle of internal friction		30°
Coefficient of restitution		0.9
Gas		Air
Operating pressure (Pa)		101325
Pressure-velocity coupling		Phase-coupled SIMPLE
Spatial discretization method	Pressure	PRESTO!
	Momentum	Convective term: First-order upwind Diffusive term: Second-order accurate central differencing scheme
	Volume fraction	First-order upwind
Transient formulation		First-order implicit
Timestep		10^{-5} s

3.4.2. Analysis of simulated data

While the entire gas-solids domain was simulated, the section highlighted in green in **Figure 3-10** was chosen as the primary area for analysis due to its relatively long, straight geometry and its suitability for direct comparison with existing experimental results for validation. Within this selected region, the predominant solids convection occurs along the x-axis (x=0.14–0.44 m), the channel spans the z-direction (z=0.04–0.16 m), and the bed height is measured along the y-axis, with y=0 corresponding to the location of the gas distributor plate. Sixteen sampling planes, perpendicular to the direction of solids transport and spaced at 0.02 m intervals along the x-axis, were established as reference points for extracting simulation data.

Prior to analyzing the simulation results, a time interval corresponding to steady-state conditions had to be identified. Steady state was assessed by monitoring the temporal evolution of the solids-phase velocity in the flow direction. In all cases, steady-state conditions were achieved after 10 s of simulation time (for details, see **Paper IV** [78]).

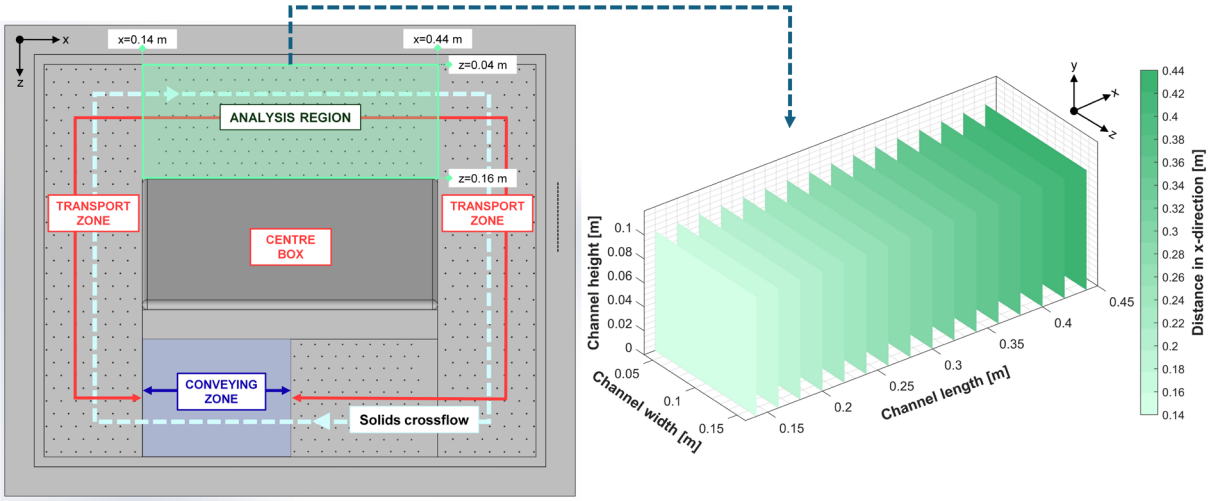

Figure 3-10: Schematic of the cold-flow model highlighting the analysis region (green area, left) and the data sampling planes along the *x*-direction (slices, right).

(i) Bulk-phase solids

To investigate the flow patterns of bulk solids, particle trajectories were obtained by numerically integrating the time-averaged solids velocity fields generated in the simulations. A fourth-order Runge-Kutta (RK4) algorithm was employed to calculate these trajectories [144]. The initial positions of the pathlines were uniformly distributed on a grid within the channel's physical boundaries, with their orientations set perpendicular to the direction of solids flow at the channel inlet plane (x=0.14 m). These trajectories were subsequently used to assess the macroscale dispersion of solids along the flow direction, applying the Einstein relation.

(ii) Lean-phase solids

To analyze the flow characteristics of particles in the lean phase, the Lagrangian particle tracking technique (**Table 2-4**) was applied in conjunction with the Eulerian–Eulerian framework for gas–solids flow (**Table 2-3**). Particle tracking was conducted as a post-processing step, using fields from Eulerian–Eulerian simulations to generate time-resolved 3D pseudo-fields of velocity, density, and viscosity (see **Section 2.4.3**). At each timestep, data from multiple planes were interpolated onto a uniform grid using scattered data interpolation with Delaunay triangulation.

As the effect of lean-phase solids density on flow parameters was empirically found to be minimal, only one of the two particle densities tested experimentally (2,970 kg/m^3) was used in the simulations. The simulation included 5,000 tracer particles, which were assumed to be spherical with a diameter of 2.55 mm—an equivalent value based on the projected area of the non-spherical cylindrical pellets used in the experiments (diameter, 2 mm; height, 3 mm; sphericity, ≈ 0.86). The particles were released at the start of the simulation and uniformly distributed within a specified region of the analysis domain: x=0.20–0.42 m (streamwise); y=0.07–0.08 m (channel height); and z=0.06–0.14 m (channel width).

To quantify the particle transport mechanisms in the lean phase, simulated particle trajectories were analyzed to determine the time-dependent fractions of particles in the dense bed and

splash regions. The boundary separating these regions was defined by a threshold value, i.e., the height marking the transition from the dense bed to the splash region, obtained from the Eulerian–Eulerian simulation results (0.095/0.115 m for low/high bed height conditions). At each timestep, particles were assigned to regions based on their vertical position, and regional fractions were computed as the proportion of tracked particles. Data analysis was restricted to times t>0.2 s, to exclude initial transients associated with particle introduction. This approach enables direct quantification of the spatiotemporal distribution of lean-phase particles, providing details as to where the particles are present over time. This information cannot be resolved experimentally, as only cross-sectionally averaged data are available. The temporal evolution of these regional fractions are presented in **Figure A 4** and **Figure A 7**.

Time-averaged fractions for each region were then obtained, enabling quantitative comparisons of particle distribution across simulated conditions. This was calculated as the mean of the instantaneous fractions over all timesteps after t>0.2 s:

$$\bar{f}_{region} = \frac{1}{N}\sum_{i=1}^{N} f_{region}(t_i) \quad [44]$$

where $f_{region}(t_i)$ is the fraction of particles in the specified region at timestep i, and N is the total number of analyzed timesteps.

After quantifying particle fractions across different regions, particle motion angles in the x–y plane were calculated at each timestep for all trajectories, yielding a large set of directional observations. Each observation was classified as belonging to either the dense bed or splash region based on the particle's position relative to the bed surface at each timestep. Angular distributions were compiled using 1° bins over the full 0–360° range, and normalized by dividing each bin count by the total number of observations in the respective region. This normalization yielded relative frequencies, enabling direct comparisons of the prevailing transport directions under varying operating conditions.

3.4.3. Model validation

The first validation tool compared bed voidage data from simulations and experiments, given its sensitivity to the closure models used in the Eulerian–Eulerian framework. The CFD model accurately reproduced the experimental bed voidage, with values of 0.50/0.54 observed experimentally and 0.49/0.53 predicted for low and high FN_{TZ}, respectively. This agreement demonstrates the model's capability to capture key features of the gas–solids flow.

The second validation tool evaluated the solids transport characteristics by comparing the convection and dispersion values from simulations and experiments across various operating conditions, for both bulk-phase and lean-phase solids. The mean solids velocity and dispersion coefficient in the streamwise direction were obtained from CFD simulations, with the latter calculated from particle pathline data using the Einstein relation over the analysis domain (see **Figure 3-10**). Both parameters were compared to experimental values derived by fitting a 1D convection–dispersion transient model, as explained in **Section 2.4.2**. The results are shown in **Figure 3-11**. The high level of agreement, in terms of both the order of magnitude and observed trends, between the simulated and experimental values demonstrates that the model reliably captures solids transport across all the operating conditions tested.

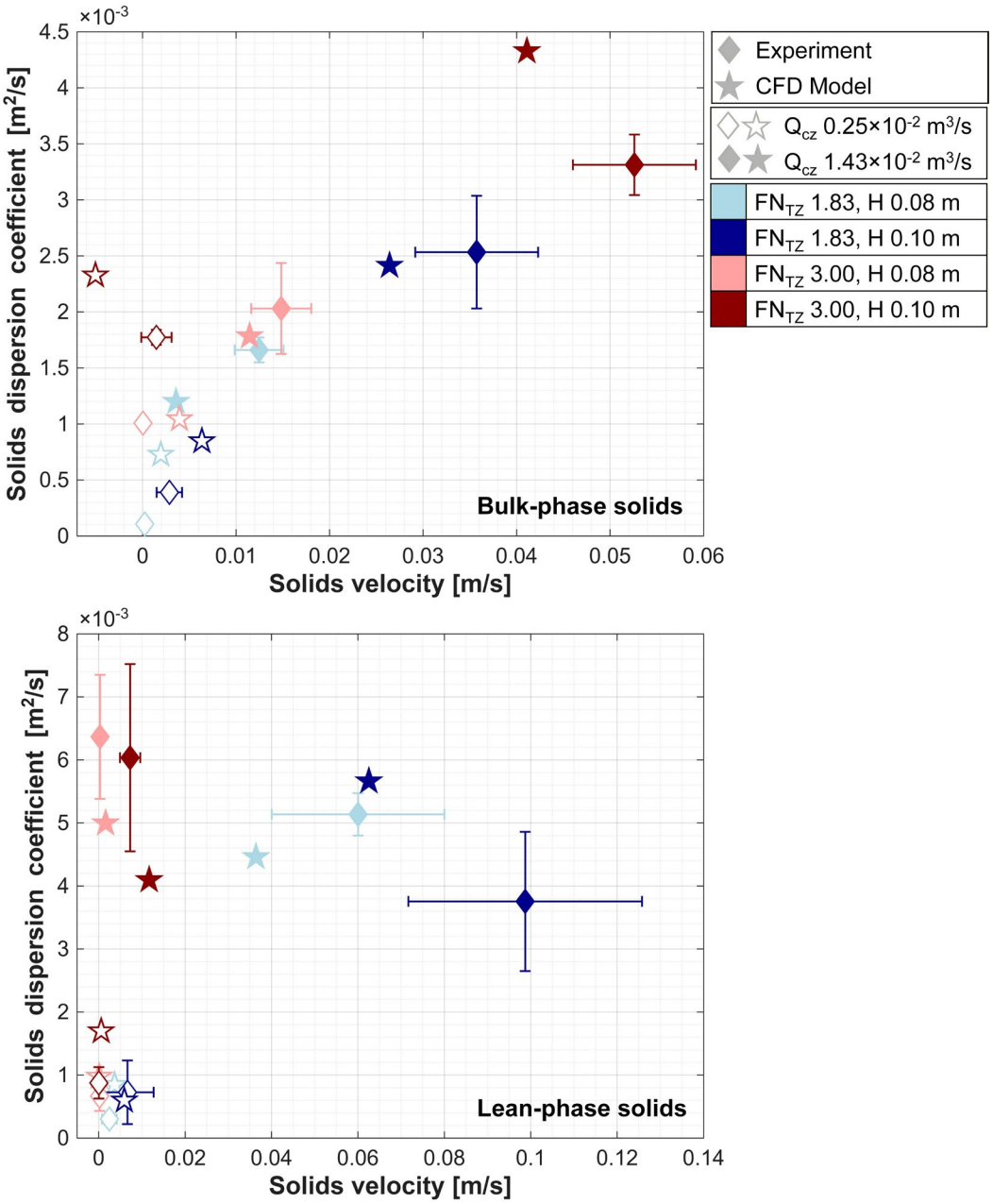

Figure 3-11: Comparison of the CFD-predicted and experimental global transport parameters under various operating conditions.

3.5. Test matrix

This thesis revolves around six research questions, as outlined in **Section 1.2**. The first five questions are addressed individually in separate research papers (see **Table 1-2**), whereas **RQ6** is investigated directly in this thesis. Each study utilizes a specific set of experiments. The test matrix (**Table 3-6**) summarizes the key variables extracted and analyzed for the characterization of both the bulk-phase and lean-phase solids flows. Five main operating parameters were controlled: fixed bed height; channel width; fluidization number in the transport zone; volumetric flow rate in the conveying zone; and solids-conveying configuration. These variables were systematically combined according to the objectives of the individual research questions.

Table 3-6: Experimental matrix for solids flow characterization addressing the different research questions (RQs).

Operating parameters	**BULK-PHASE SOLIDS**	**RQ1**	**RQ2**	**RQ3**	**RQ4**	**RQ5**	**LEAN-PHASE SOLIDS**	**RQ6**
Fixed bed height, H [m]		0.08–0.10	0.08–0.10	0.08–0.10	0.08–0.10	0.08–0.10		0.08 – 0.10
Channel width, W [m]		0.12	0.12	0.12	0.07–0.12	0.12		0.12
Fluidization number in the transport zone, FN_{TZ} [-]		1.83–4.00	3.00	1.83–3.00	3.00	1.83–3.00		1.83–3.00
Volumetric flowrate in the conveying zone, Q_{CZ} [m³/s]		0–0.015	0–0.015	0–0.015	0–0.010	0–0.015		0–0.015
Solids conveying configuration, [-]		Free solids splashing	Free solids splashing, Confined solids splashing, Slugging, Solids entrainment, Directed gas injection	Free solids splashing	Directed gas injection	Free solids splashing		Free solids splashing
Characterization of solids flow								
1. Solids convection		×	×	×	×	×		×
2. Solids dispersion (macro-scale)				×	×	×		×
3. Solids dispersion (micro-scale)					×			
4. System non-idealities				×				
5. Fanning friction factor						×		
6. Solids conveying efficiency			×					

4. Results and discussion

This chapter summarizes the principal findings of the thesis, structured into four sections. **Section 4.1** evaluates the measurement methods used for quantifying the solids mass flow rate. **Section 4.2** examines the performances of different solids-conveying configurations and assesses their conveying efficiencies. **Section 4.3** presents the flow characterization of bulk solids, divided into three subsections: solids transport parameters (convection–dispersion relationship), fluidization quality, and rheological analysis. **Section 4.4** addresses lean-phase solids, focusing on the transport parameters (convection–dispersion relationship), the impact of solids crossflow on particle transport, and trajectory analysis.

4.1. Methods for quantifying solids convection

This section addresses **RQ1** (**Paper I**) regarding how the solids circulation rate in the investigated system, a bubbling fluidized bed with solids crossflow, can be measured accurately. **Figure 4-1** presents the mean solids velocity, $u_{s,x}$, which is proportional to the forced convective flow of solids, as determined using four measurement methods (integral mass accumulation, differential mass accumulation, thermal tracing, and magnetic solids tracing). The results are shown for a range of experimental conditions, enabling assessment of the system's response to variations in bed height (H), fluidization number in the transport zone (FN_{TZ}), and volumetric air flow rate in the solids-conveying zone (Q_{CZ}). The vertical bars in **Figure 4-1** indicate the variance for three replicate measurements for each set of conditions; in some cases, these bars are not visible due to their small magnitude. All four methods yield similar qualitative trends: increases in any of the three operational variables lead to higher solids flow rates. However, the absolute values and rates of increase differ among the methods.

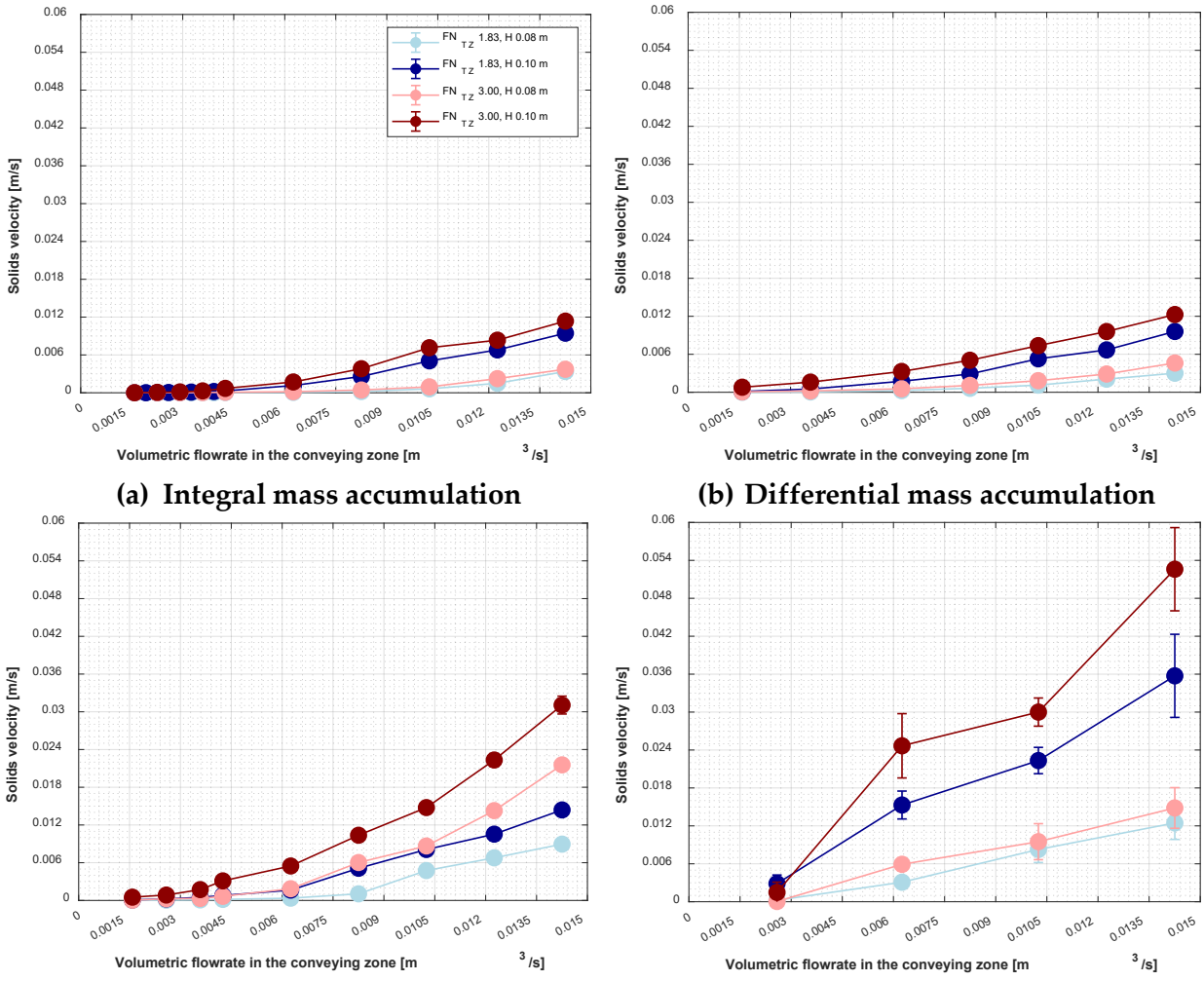

(a) Integral mass accumulation **(b) Differential mass accumulation**

(c) Thermal tracing **(d) Magnetic solids tracing**

Figure 4-1: Solids velocity obtained using four different measurement methods, assessed under varying operational conditions.

The two mass accumulation methods yielded comparable solids flow rates, which were generally lower than those obtained by the other techniques. This discrepancy is likely due to a reduction in the flow rate as accumulation progresses, as well as to material losses during

the measurement. Both methods have limited accuracy at low solids-conveying rates. The integral method fails to register low rates when splashed material does not reach the collection box, whereas the differential method requires that the pressure increase substantially exceed the pressure signal's noise level to be reliably associated with the flow rate.

The thermal tracing method yielded solids flow rates that were significantly higher—by a factor of 2.5 to 2.8—than those measured by the mass accumulation techniques. This is attributed to the method's reliance on surface-temperature data, where solids dispersion due to bubble splashing occurs more rapidly than in a dense bed. As a result, the thermal method may yield higher horizontal dispersion values, leading to lower estimates of convective velocity. Further evidence of this is presented in **Figure 16** in [145], which compares the dispersion values obtained using the thermal and magnetic solids tracing methods. In addition, at high solids flow rates, the small spatial temperature gradients further reduced the accuracy of this method. The magnetic solids tracing method reported the highest solids flow rates among the four techniques. It is regarded as the most reliable method for determining solids flow rates due to its capacity for continuous measurement—unlike the start–stop approach of mass accumulation methods—and its robust signal detection. The magnetic tracer produces distinct, transient responses that are easily separated from the background noise, ensuring accurate results under varying operating conditions and minimizing susceptibility to interference.

A regression analysis was conducted to assess the effects of operational parameters on solids flow rates measured using the four measurement methods; the resulting factorial effect size statistics are presented in **Figure 4-2**.

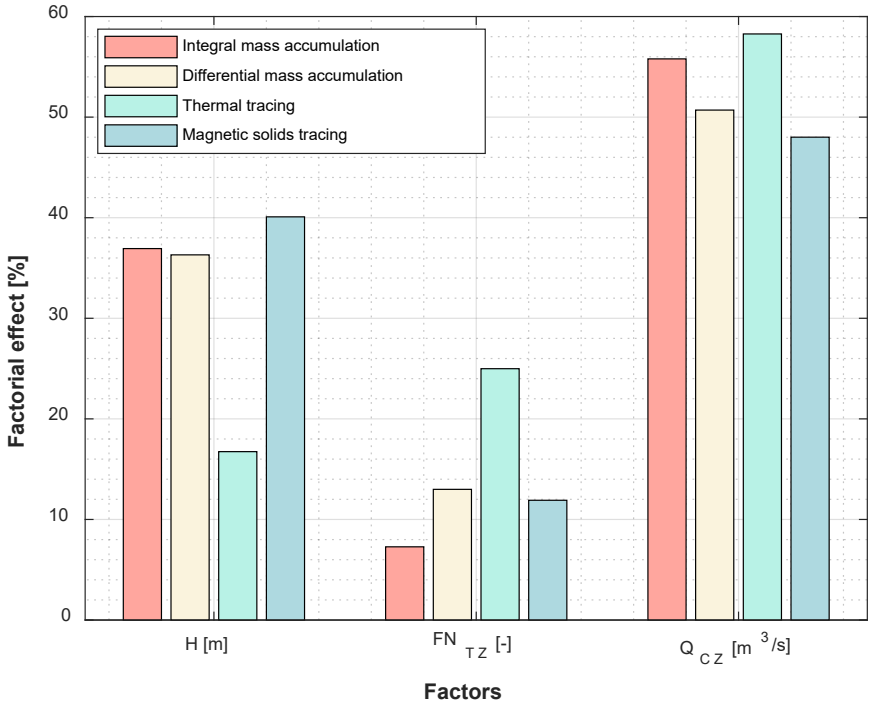

Figure 4-2: Comparative analysis of factorial effect sizes for the three operational parameters across the four evaluated measurement methods.

Across all four methods, the airflow rate in the solids-conveying zone exerted the strongest effect on solids velocity, accounting for 48%–60% of the total factorial effect, underscoring its central role in regulating solids transport. A fixed bed height was the second-most-influential

parameter across all methods, except for thermal tracing, where the fluidization number in the transport zone was more significant (25%); it had only a minimal effect (8%–12%) in the other techniques. This distinct sensitivity pattern suggests that the thermal solids tracing method is less reliable and potentially less accurate. In contrast, the mass accumulation and magnetic solids tracing methods showed consistent responses to the operational variables, with the latter demonstrating the highest overall accuracy.

To summarize, magnetic solids tracing is selected as the most accurate method for quantifying the solids circulation rate and is therefore applied to address the remaining research questions.

4.2. Solids conveying efficiency

This section addresses **RQ2** (**Paper II**) by examining how the horizontal flow of fluidized solids can be achieved and assessing the effectiveness of the resulting convective transport. **Figure 4-3** presents, for each of the five solids-conveying configurations examined, the relationship between the energy flow associated with the horizontal transport of fluidized solids (Eq. [2]) and the energy input supplied to the conveying zone (Eq. [3]), along with the resulting efficiency. The differences in performance observed between the tested configurations are attributable to variations in their underlying fluidization dynamics and gas–solids interactions.

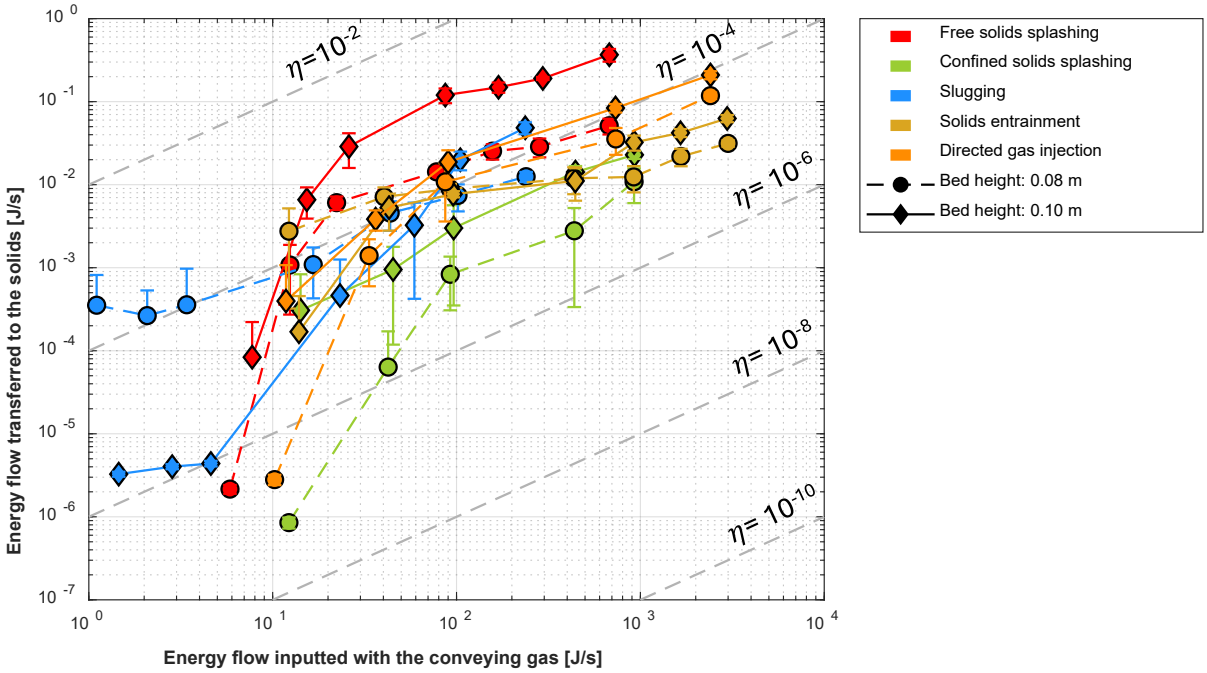

Figure 4-3: Characterization of the conveying zone dynamics in a BFB-BFB bed using analysis of the energy input and solids energy flux for the five tested configurations. The dashed lines indicate the solids-conveying efficiencies (η). Source: Paper II.

Among the tested configurations, the free solids splashing setup exhibited the highest energy transfer efficiency, attributed to macroscopic particle transport in the bubbling regime, where bubble bursting effectively transfers kinetic energy in the horizontal direction. In contrast, the confined solids splashing and solids entrainment configurations, both characterized by highly erratic particle motions and rapid gas streams, exhibited lower energy transfer efficiencies, as a larger fraction of the energy was consumed to sustain fluidization and mixing at finer scales

rather than for bulk solids movement. The slugging and directed gas injection configurations achieved intermediate efficiencies, benefiting from substantial, albeit less chaotic, solid–gas interactions. These findings highlight the significance of the conveying configuration and the nature of the solid–gas interactions in determining the overall energy efficiency of the operation. More-organized gas flow structures, such as well-defined bubbles or slugs, are shown to enhance energy transfer to the solids. In addition, although bed height generally affects energy efficiency, this effect was most pronounced in the free solids splashing configuration.

Compared with conventional risers in CFB systems, both free splashing and directed gas injection configurations exhibited higher solids-conveying efficiencies. These configurations achieved solids circulation at lower fluidization velocities compared to traditional risers. Under up-scaled conditions (900°C), the solids circulation rates were in the range of 5×10^{-2}–2×10^{3} kg/m²·s at fluidization velocities in the range of 0.3–4.3 m/s (see **Figure 10** in **Paper II** [143]). These results indicate that the tested configurations offer a more energy-efficient approach to driving solids circulation than traditional risers.

To summarize, the results demonstrate that the horizontal flow of fluidized solids can be effectively induced by specific conveying configurations, with free solids splashing and directed gas injection exhibiting the highest efficiencies for convective transport.

4.3. Flow characterization of bulk-phase solids

This section addresses three research questions, each focusing on a different aspect of the bulk solids flow characterization in a bubbling fluidized bed with solids crossflow. **Section 4.3.1** investigates global solids transport by analyzing the relationship between the solids velocity and dispersion coefficient using a macroscopic transport modeling approach (**RQ3→Paper III**). **Section 4.3.2**, using CFD simulations based on the Eulerian–Eulerian framework, explores the roles of transport parameters in shaping the overall flow structure. It further examines the local solids velocity, granular temperature distributions, and distinguishes between micro-scale and macro-scale dispersion types (**RQ4→Paper IV**). **Section 4.3.3** evaluates fluidization quality using ideal reactor models (PFR/CSTR comparison) and the dead zone index, employing a compartment modeling approach (**RQ3→Paper III**). **Section 4.3.4** investigates the influence of frictional losses on the horizontal flow and the rheological behavior of the gas–solids suspension, utilizing established literature models alongside a newly proposed correlation (**RQ5→Paper V**). Regarding experimental techniques, magnetic solids tracing (**Section 3.3.4**) is used for **RQ3** and **RQ4**, while crossflow fluidized bed rheometry (**Section 3.3.5**) is used for **RQ5**.

4.3.1. Solids transport parameters

Figure 4-4a displays paired values of the solids velocity and solids dispersion coefficient (u_s, D_s) for bulk-phase solids in the streamwise direction, across all the tested operational sets, defined by fluidization number in the transport zone (FN_{TZ}), fixed bed height (H), and solids-conveying velocity (Q_{CZ}). Error bars indicate the variability observed across three replicate measurements for each set. Notably, a strong, almost linear relationship is apparent between the two parameters, suggesting that convection, via friction-induced shear mixing, enhances

the horizontal mixing of solids. It is also evident that both transport parameters exhibit increasing trends as the operational variables are increased.

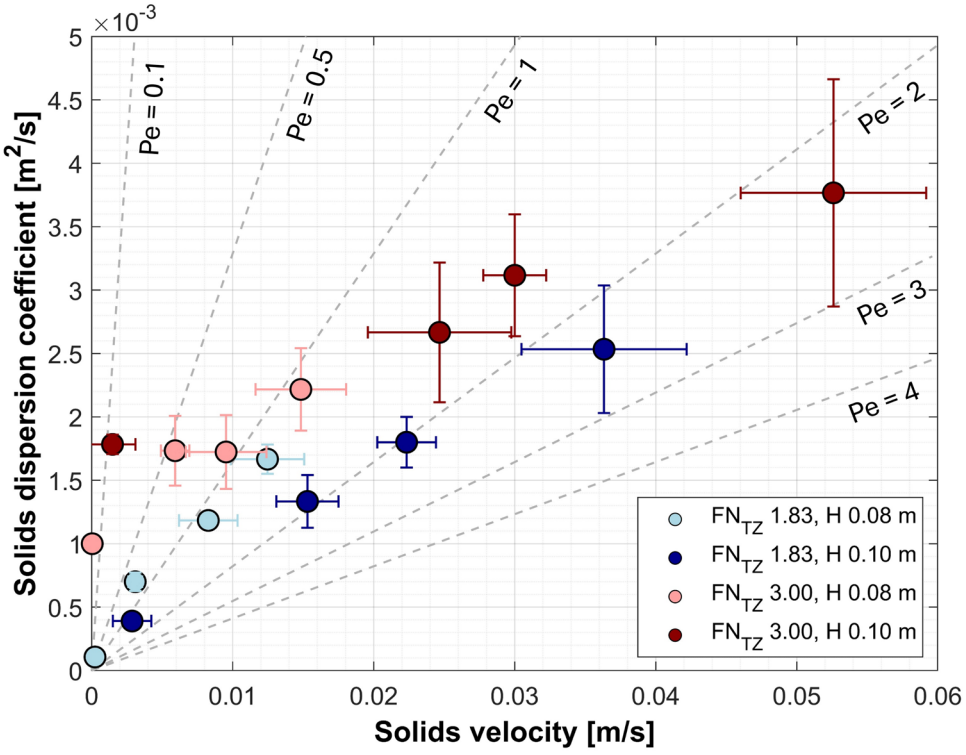

(a) Correlation between the solids dispersion coefficient and the solids velocity. The dashed lines on the plot indicate Péclet numbers.

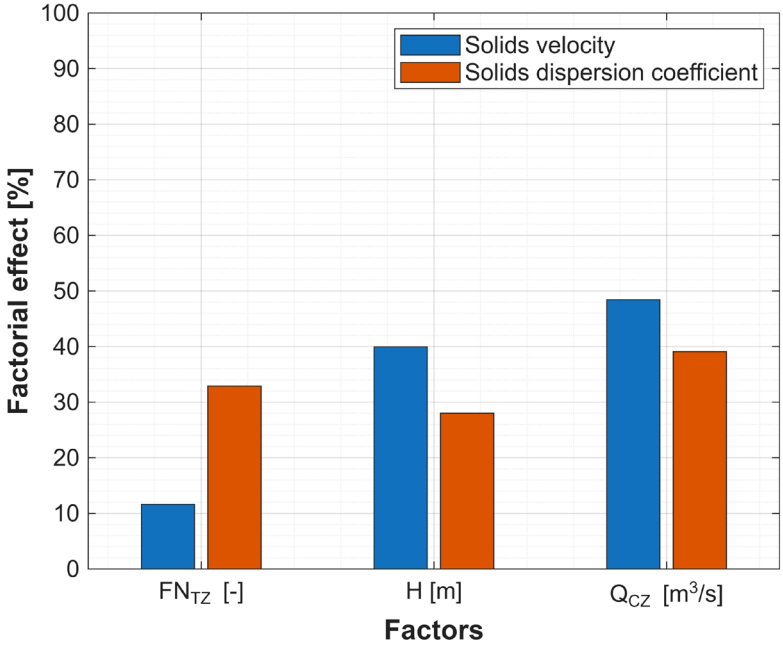

(b) Regression analysis of parameter contributions.

Figure 4-4: Impact of operational parameters on global transport parameters for bulk-phase solids in the streamwise direction. Source: Paper III.

The regression analysis (**Figure 4-4b**) quantifies the contribution of each operational parameter to the solids velocity (blue bars) and the solids dispersion coefficient (orange bars). The Q_{CZ} parameter is the dominant factor affecting the solids velocity (48%), followed by bed height H

(40%), which increases the active conveying zone and, thus, the velocity. FN_{TZ} contributes to a lesser extent (12%) by enhancing voidage and reducing friction in the circulation path. For the solids dispersion coefficient, the Q_{CZ} factor also has the strongest influence (39%), whereas FN_{TZ} and H account for 34% and 27%, respectively. These trends are consistent with previous studies [129] that employed stationary fluidized beds, linking increased airflow and bed height to enhanced bubble activity and the formation of larger bubbles at higher solids flow rates. Notably, the solids crossflow affects the system to a similar extent.

In summary, the global transport parameters (u_s, D_s) for bulk-phase solids exhibit a strong linear correlation, and systematically increase with the tested operational parameters (**RQ3**). The analysis also shows that, although the Péclet number (Pe) generally increases with velocity, it reaches a plateau at higher values—especially in taller beds—implying that increasing velocity alone does not achieve plug flow, as higher velocities tend to promote back-mixing rather than purely forward transport.

4.3.2. Solids flow structure

Examining flow structures is essential for understanding global trends in solids transport, particularly the linear velocity–dispersion relationship in the crossflow direction, as identified in **Section 4.3.1**. **Figure 4-5** displays the particle pathlines for FN_{TZ} of 3 at two values of fixed bed height and solids-conveying velocity, respectively. Representative pathlines for FN_{TZ} of 1.83 are shown in **Figure A 1** and are not presented here in the main text, as the trends are similar. The particle pathlines are color-coded from blue to yellow, ordered by increasing initial injection height. Across all the tested conditions, it is evident that the operating parameters significantly affect the position, distinctness, and size of the vortex structures. At low solids crossflow rates, prominent macrostructures corresponding to large-scale recirculation zones are observed, in which particle trajectories follow compact, coherent vortical paths, thereby limiting the characteristic transport length. The visualizations also reveal that the sizes of these structures increase with bed height, consistent with the trend of increased dispersion seen in **Section 4.3.1**. In contrast, increasing the solids crossflow rate disrupts the distinct recirculation vortices, producing more elongated and less organized pathlines that may be associated with enhanced internal mixing.

To better understand the mechanisms underlying the observed particle pathlines and vortex structures, the spatial variation of the solids velocity in the streamwise direction and the turbulent granular temperature (calculated using Eq.[22] in **Paper IV** [78]) are analyzed. **Figure 4-6** summarizes these results for a representative operating condition, with profiles plotted as a function of bed height (top row) and channel width (bottom row). The data are presented at selected streamwise positions, as indicated in **Figure 3-10**.

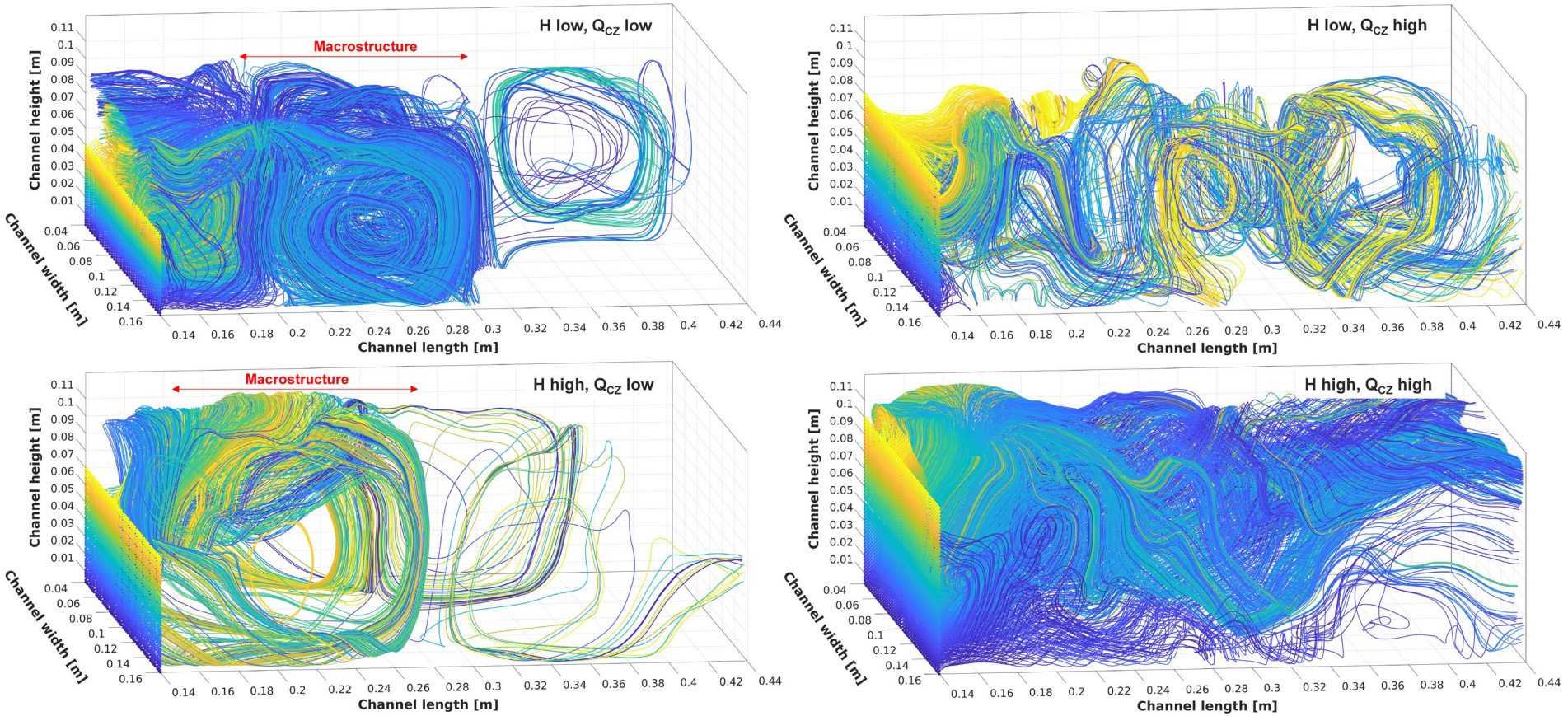

Figure 4-5: Particle pathlines in the analysis region for varying bed heights (H) volumetric flow rates of air in the conveying zone (Q_{CZ}), at FN_{TZ} of 3. Source: Paper IV.

For the solids velocity component (**Figure 4-6a**), the vertical profiles reveal notable changes in the flow pattern along the channel length. Upstream (x=0.14–0.28 m), forward motion predominates near the bed surface, while reverse flow is present closer to the distributor plate. At downstream locations (x=0.34–0.44 m), this pattern is inverted, with reverse flow near the bed surface and forward motion near the distributor. The high velocities near the distributor plate arise from intense gas–solid interactions, where vertical gas jets and bubble formation initiate macrostructure formation in the system. Subsequently, these structures redirect the solids motion along the streamwise direction—either forward or backward, depending on their orientation. In proximity to the bed surface and splash zone, bubble eruptions produce ballistic particle trajectories with substantial horizontal displacement. An inflection point at mid-bed height is associated with a sequence of vortices exhibiting alternating spin directions, as further detailed in **Figure A1** of **Paper IV** [78]; the exact structure varies with the operating conditions applied. The corresponding profiles across the channel width demonstrate an asymmetric flow profile with steep velocity gradients close to the sidewalls. This asymmetry reflects the influence of strong wall effects and the organization of vortex structures within the cross-section (see **Figure A2** in **Paper IV** [78]). The proximity of counter-rotating vortices to the walls enhances local shear and contributes to the formation of shear layers. The z-direction is defined such that the channel width extends from z=0.04 m to z=0.16 m.

The laminar granular temperature is about two orders of magnitude lower than its turbulent counterpart, indicating that random particle motion and collisions play minor roles in solids mixing compared to the turbulence generated by the bubble dynamics and large-scale eddies (see **Figure 11** in **Paper IV** [78]). The profiles presented in **Figure 4-6b** indicate that microscale dispersive transport reaches a local maximum just above the bottom plate, then sharply declines with height, followed by a moderate rise within the dense bed. The dispersion reaches its highest value in the splash region, which is attributable to the ejection of solids by erupting bubbles. Above this zone, in the dilute region, the dispersion decreases further with increasing height. This trend is consistent throughout the channel and aligns with previous studies, showing that bubble eruptions account for 30%–90% of horizontal solids mixing, depending on the system configuration [55,146,147]. Across the channel width, dispersion remains largely uniform, with only slight variations apparent near the sidewalls. This indicates that bubble-induced mixing is laterally consistent within the channel core and that wall effects are minimal.

The comparable orders of magnitude between the micro-scale (turbulent, see **Table A1** in **Paper IV** [78] for values) and macro-scale dispersion in the streamwise direction suggest that the mixing contributions from local turbulence and large-scale structures are similar.

In summary, this analysis shows that solids transport parameters (u_s, D_s) directly shape the global flow structure (**RQ4**). At low crossflow rates, solids motion is governed by counter-rotating vortices, resulting in significant backmixing and alternating regions of forward and reverse flow. As the crossflow rate increases, these vortex structures are disrupted, leading to predominantly forward transport, more elongated macrostructures, and higher dispersion coefficients.

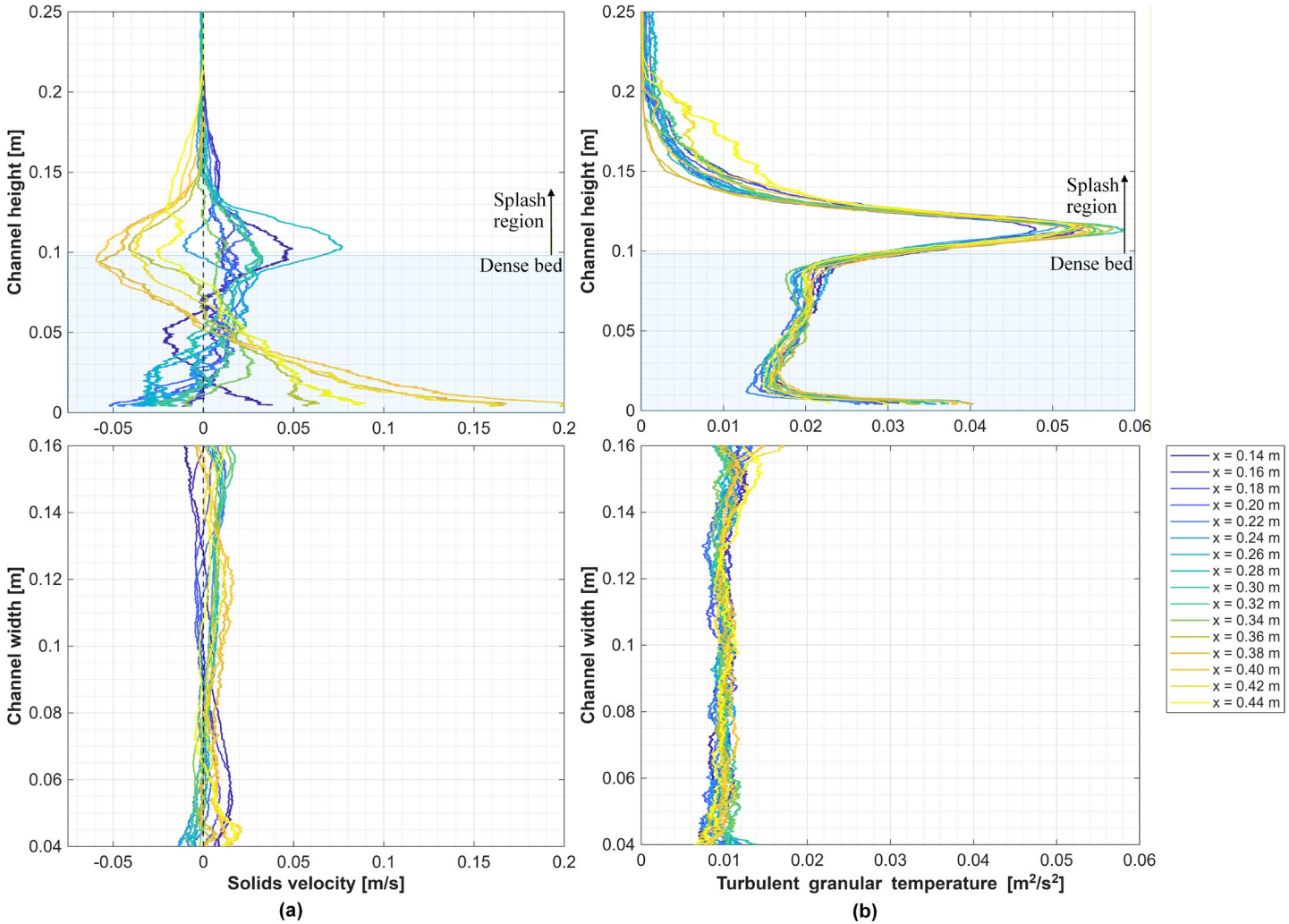

Figure 4-6: Profiles of: (a) the solids velocity in the flow direction; and (b) the turbulent granular temperature at various streamwise locations, shown as a function of the channel height (top row) and channel width (bottom row). Conditions: H, 0.08 m, Q_{CZ}, 1.43×10^{-2} m^3/s. Source: Paper IV.

4.3.3. Fluidization quality

Figure 4-7 illustrates the influence of operational conditions on the dead zone index (**Figure 4-7a**) and the number of CSTRs in series (**Figure 4-7b**), parameters that are defined in the compartment modelling approach (see **Section 2.4.1**). The PFR component yielded negligible magnitudes across all modeled cases, indicating that it need not be explicitly included in the compartment model for the configuration studied.

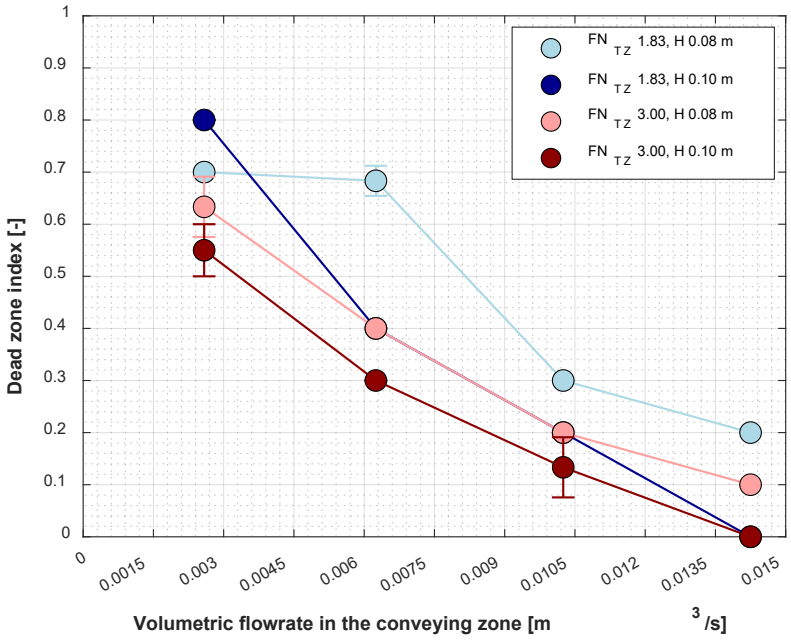

(a) Dead zone index

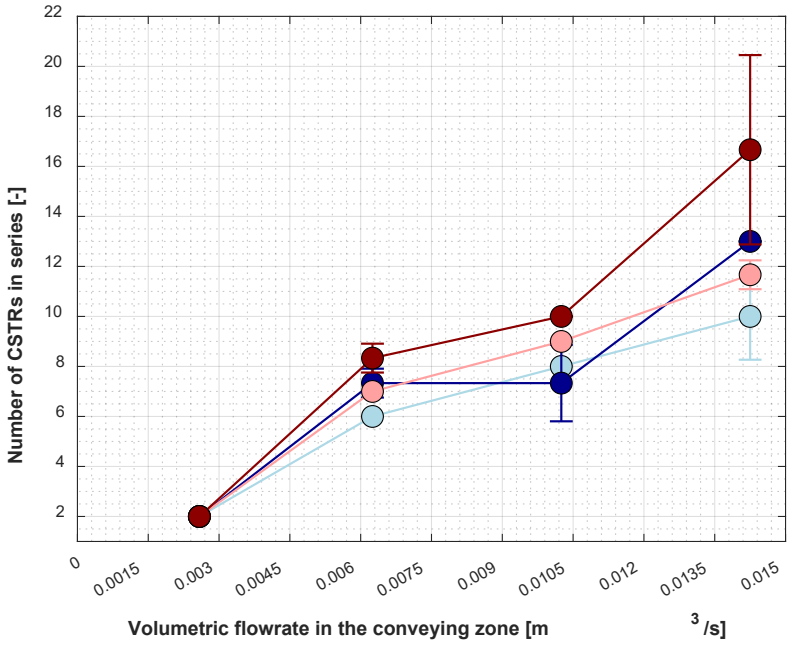

(b) Number of CSTRs in series

Figure 4-7: Impact of operational conditions on the variables extracted after compartment model fitting. Source: Paper III.

As shown in **Figure 4-7a**, the dead zone index decreases with an increase in the fluidization number, bed height, and air flow rate in the conveying zone. Notably, the effect of bed height

observed here contrasts with findings for stationary bubbling beds, where greater bed height typically negatively affects gas–solids mixing due to higher bed-to-distributor pressure drop ratios and larger bubble sizes. However, the relatively narrow range of bed heights examined in this study likely limits the observed impact. The data further indicate that a higher solids crossflow is more effective in reducing the extent of stagnant zones in taller beds. Regarding the number of CSTRs in series (**Figure 4-7b**), a pronounced increase is observed with higher conveyed solids rates, fluidization numbers, and bed heights. This trend reflects a transition from the uniform, well-mixed behavior characterized by higher dispersion to a regime dominated by convection, with solids transport becoming more plug-flow-like.

To summarize, the analysis demonstrates that increasing any of the operational parameters improves fluidization quality by reducing the extent of stagnant regions. This promotes a shift from strong backmixing to a more convective transport in the direction of the solids crossflow (**RQ3**).

4.3.4. Solids flow rheology

Figure 4-8 presents the relationship between the macroscopic pressure drop gradient and the mean solids velocity in the streamwise direction. The results show that the pressure drop increases with higher solids velocities and with decreasing channel width. Regression analysis shows that channel width has the most significant factorial effect, accounting for 70.6% of the variance. In comparison, fixed bed height and solids velocity contribute only 11.4% and 18.0%, respectively (see **Figure 4** in **Paper V** [148]).

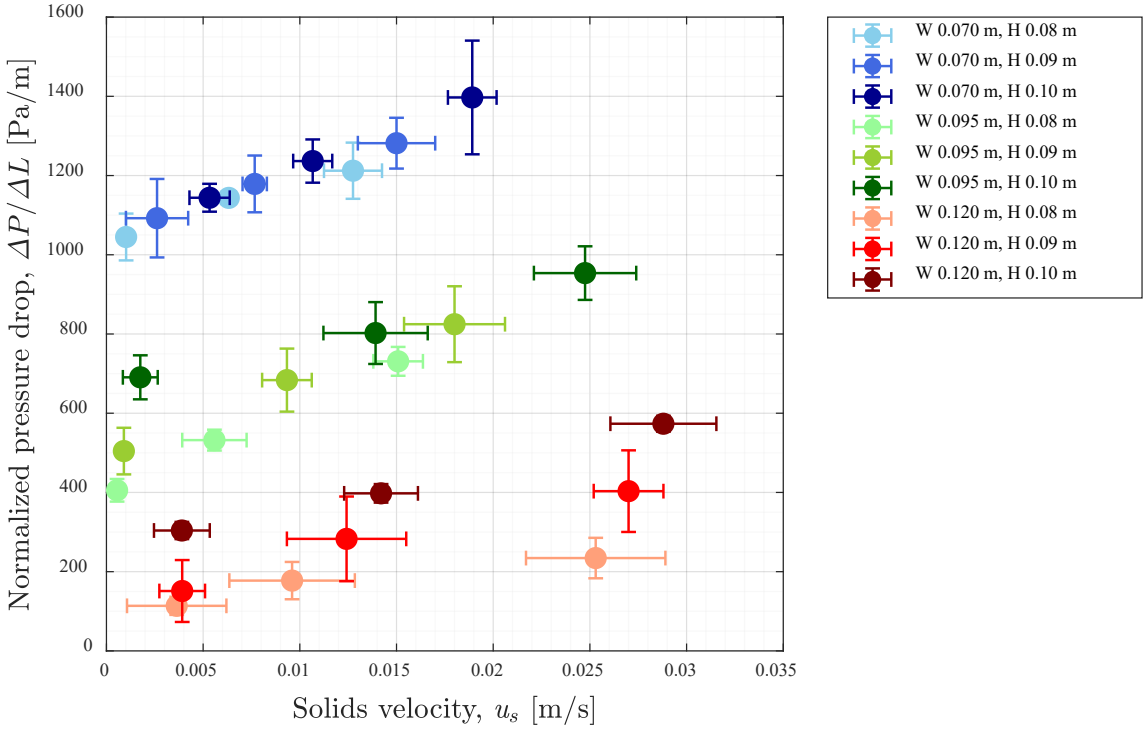

Figure 4-8: Macroscopic horizontal pressure gradient as a function of the solids velocity in the direction of the crossflow. Source: Paper V.

The relationship between the Fanning friction factor (see Eq. [4]) and the Péclet number (**Figure A 2**) shows that the value of f decreases as Pe increases, reflecting reduced viscous resistance and a lower energy demand as convective transport becomes dominant. At high Pe,

frictional losses are minimal, whereas at low Pe, viscous effects prevail, resulting in greater frictional resistance and higher energy consumption.

To investigate the rheological behavior of the suspended solids flow, the experimental data presented in **Figure 4-8** were analyzed using established rheological models, as described in **Section 2.3.1**. By fitting the measurement data, the empirical constants for the flow consistency index in non-circular channels in Eq. [8] were determined as C_W=-5.85×10^{-3} and C_{H_b}=6.51×10^{-3}. **Figure 4-9** summarizes the results of the comparison of the measured and predicted wall shear stresses, along with the observed rheological flow curve for the fluidized solids.

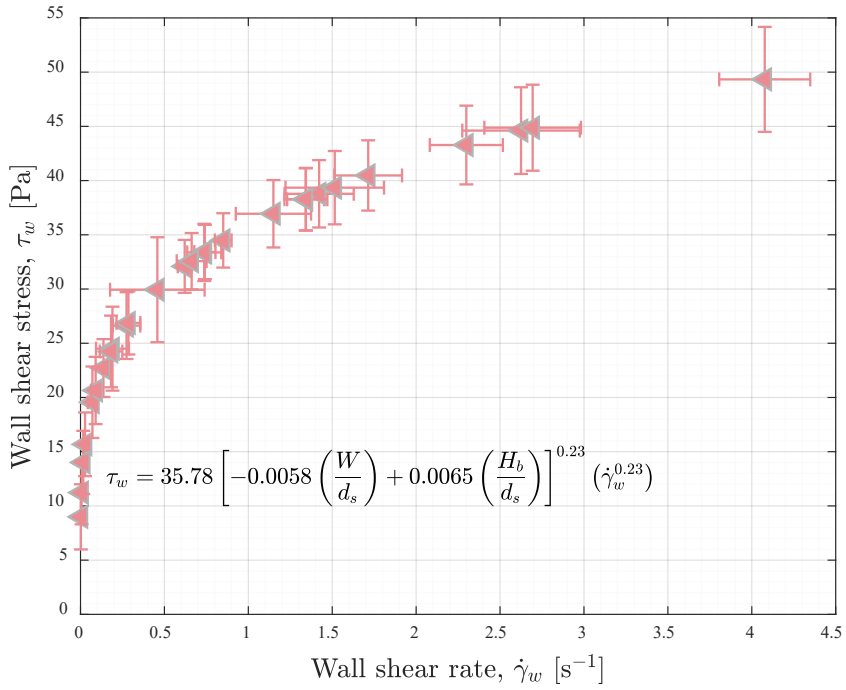

(a) Wall shear stress vs. wall shear rate profile.

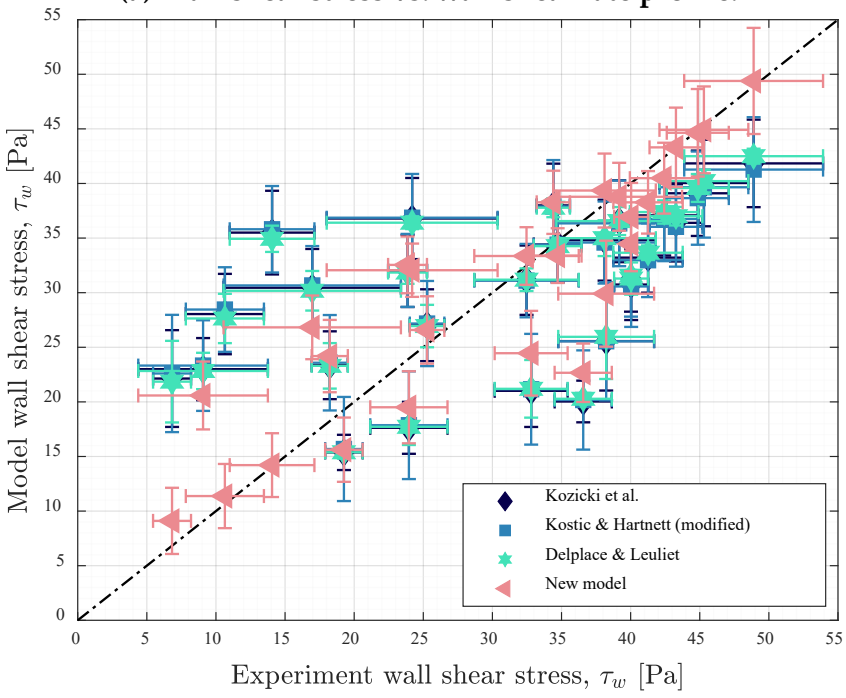

(b) Comparison of the modeled and experimental wall shear stress values.

Figure 4-9: Rheological assessment of the suspended solids flow. Source: Paper V.

Figure 4-9a presents the results from the proposed model, showing the relationship between wall shear stress (5–55 Pa) and true wall shear rate (0.002–4.5 s^{-1}), demonstrating a shear-thinning behavior. **Figure 4-9b** compares the measured wall shear stress with the model predictions to assess predictive accuracy. The R-squared values for the Kozicki et al. [91–94], Kostic-Hartnett [96,97], and Delplace-Leuliet [95] models were 0.314, 0.291, and 0.351, respectively, indicating notable discrepancies between the model predictions and experimental results. These models, originally developed for single-phase flow in rectangular channels, have not been previously validated for gas-fluidized solids and exhibit limited applicability in this context, underscoring the need for more suitable models. In contrast, the new model developed in this work shows strong agreement with the experimental data (R-squared = 0.785).

Additional insights into the rheological flow behavior are obtained by fitting the experimental data to a constitutive granular flow model, enabling identification of the operating regime, as described in **Section 2.3.2**. **Figure 4-10** presents the effective friction coefficient as a function of the inertial number, with the data fitted to the $\mu(I)$ constitutive law(Eq. [9]). The $\mu(I)$ model provides an adequate description of the experimental results, which span inertial numbers in the range of 10^{-6}–10^{-2}, corresponding to the dense flow regime, with $\mu(I)$ values in the range of 0.03–0.3. This indicates that both interparticle friction and collisions significantly contribute to momentum transfer in the solids flow.

It should be noted that, while the model fit suggests threshold inertial numbers and potential regime transitions, validating these thresholds would require a broader experimental range than was available in the present study.

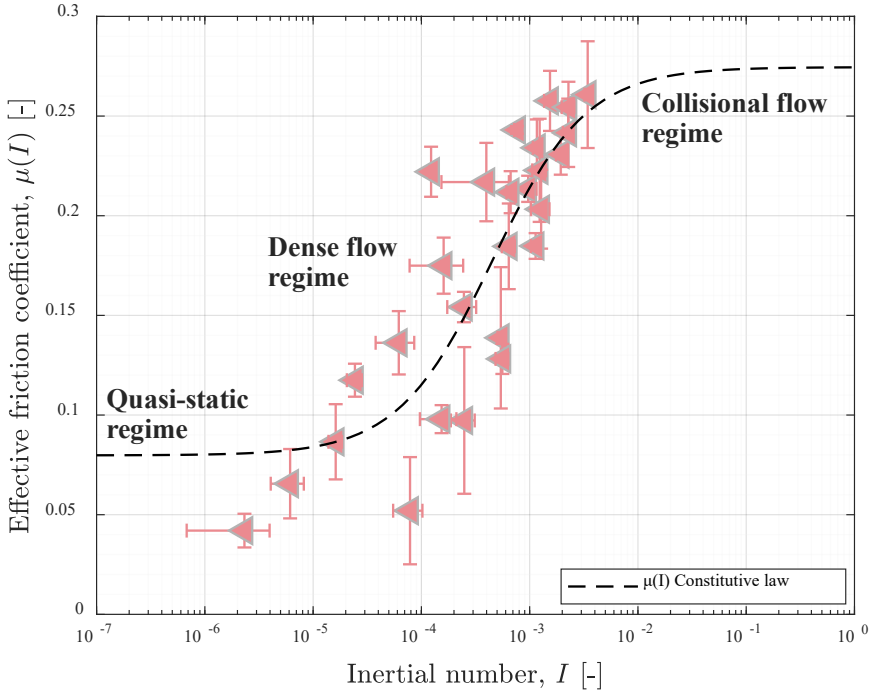

Figure 4-10: Effective friction coefficient variation with inertial number, fitted with the $\mu(I)$ constitutive law (Eq. [9]) curve. Source: Paper V.

To summarize, the horizontal pressure gradient increases with the solids velocity and bed height, but decreases as the channel width increases, while the bed solids suspension exhibits shear-thinning behavior. The Fanning friction factor decreases with rising Péclet number, indicating reduced viscous resistance and lower energy demand as convective transport becomes more significant. The granular flow analysis confirms that the system operates in the dense flow regime.

4.4. Flow characterization of lean-phase solids

This section addresses **RQ6** by examining the impact of bulk-solids crossflow on the transport of lean-phase solids. Using a macroscopic transport modeling approach, **Figure 4-11a** shows a positive correlation between the mean velocity and the dispersion coefficient in the crossflow direction for lean-phase solids, evaluated across various operating conditions. Overall, the dispersion coefficients remain similar at both fluidization levels, while the macroscopic solids velocity is significantly reduced at higher fluidization velocity. Under conditions of high fluidization (FN_{TZ}=3), intense splashing and bubble activity dominate the transport of lean solids. In contrast, at low levels of fluidization (FN_{TZ}=1.83), visual observations indicate a marked change in the flow pattern: solids crossflow leads to the formation of a layer of lean solids on the bed surface, which slides over the bed of bulk solids with a greater convective, plug-like transport (with Pe>1) that predominates over the splashing-driven transport. A comparison with the transport parameters for bulk-phase solids (see **Figure A 11**) shows that the dispersion coefficients for lean-phase particles are consistently higher across all fluidization levels. Furthermore, while lean-phase particles exhibit weaker convection than bulk-phase solids at high FN_{TZ}, they show stronger convection at low FN_{TZ}.

Figure 4-11b presents the results of the regression analyses for the solids velocity (bottom-left) and solids dispersion coefficient (bottom-right), illustrating the influences of operating parameters—fluidization number in the transport zone (FN_{TZ}), bed height, and conveying zone flow rate (Q_{CZ})—on the velocity and dispersion of the lean-phase particles. With regard to velocity, the lean-phase particles are primarily affected by FN_{TZ} and Q_{CZ}, with bed height exerting minimal influence. FN_{TZ} exerts a greater impact on the horizontal velocity of lean-phase particles, as lower-density particles are more easily entrained and conveyed by the increased gas flow. With respect to the dispersion coefficient, Q_{CZ} emerges as the primary driver, reflecting the increased susceptibility of these particles, particularly those of lower density (1,370 kg/m³), to entrainment and lateral transport by the gas flow. For high-density (2,970 kg/m³) lean-phase solids, FN_{TZ} also exerts significant influence, as a higher fluidization energy is required to overcome its inertia and promote dispersion.

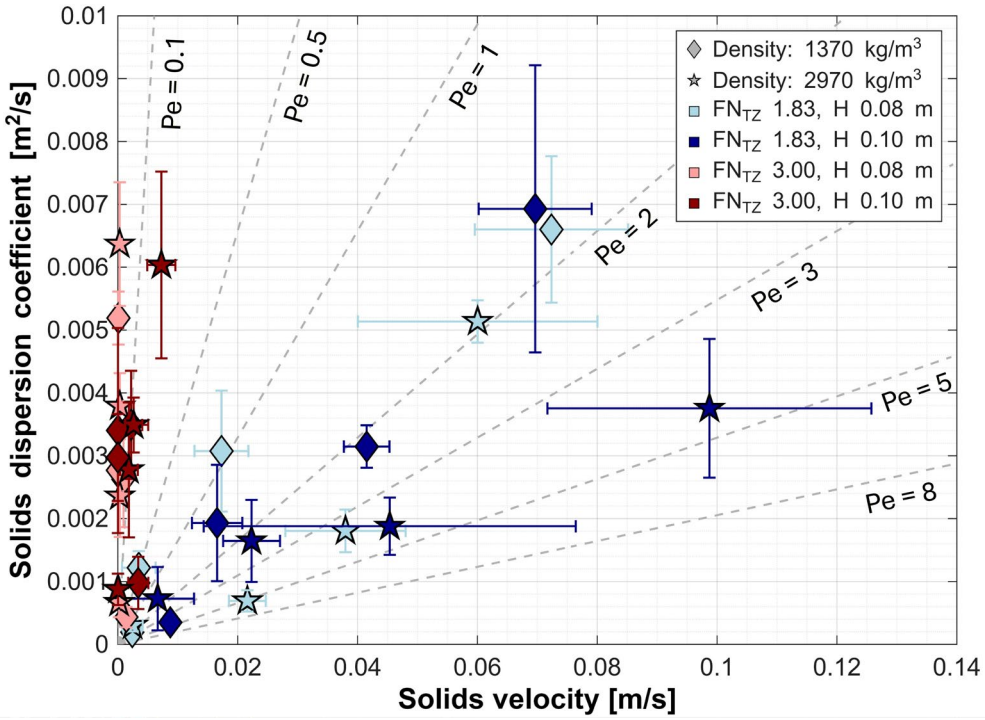

(a) Correlation between the solids dispersion coefficient and the solids velocity. The dashed lines on the plot indicate Péclet numbers.

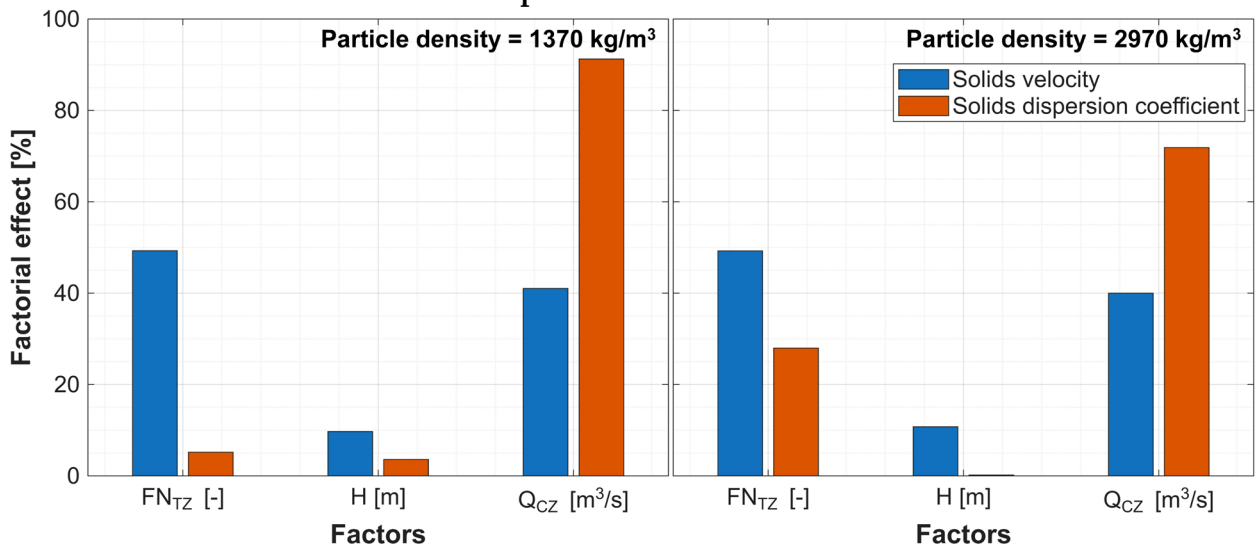

(b) Regression analysis of parameter contributions.

Figure 4-11: Impact of operational parameters on global transport parameters for lean-phase solids in the streamwise direction.

A comparative study of (up-scaled) cold-flow results and hot-scale experimental data is presented in **Appendix E**.

In addition, a trajectory-based assessment was conducted to distinguish the particle dynamics in the dense bed and splash regions. This analysis applied the LPT technique, supported by local pseudo-fluid properties obtained from the Eulerian–Eulerian simulations. The trajectories of the lean-phase particles were examined under two key operating conditions: (i) varying fluidization number in the transport zone (FN_{TZ}, **Figure 4-12**); and (ii) varying volumetric flow rate in the conveying zone (Q_{CZ}, **Figure 4-13**). In each figure, the left panels display the simulated particle trajectories at the low (top panel) and high (bottom panel) values

of the operating parameter. The dense region is highlighted in blue, with the splash zone shown above. Visual inspection indicated that lean-phase particles are transported mainly within the splash zone, i.e., above the bed surface. To quantify these observations, regional particle fractions were calculated using the approach described in **Section 3.4.2** (see Eq. [44]). The resulting angular distributions, shown in the polar plots (right panels: splash region, light-brown; dense bed region, dark-brown), represent the normalized frequency of particle displacements for each one-degree interval.

A marked shift in particle transport behavior is observed as FN_{TZ} is varied, as shown in **Figure 4-12**. At low FN_{TZ}, nearly all of the lean-phase particles (≈98%–99.95%; **Figure A 9**) remain confined to the splash region. This reflects the formation of a dense, compact layer above the bed that mainly restricts particle mixing to this zone, as discussed previously. The corresponding angular distributions indicate that, under these conditions, particle motion in the splash region is strongly aligned with the streamwise direction. In contrast, at higher FN_{TZ}, the fraction of particles in the splash region decreases (≈70%–85%; **Figure A 9**), indicating that enhanced splashing and bubble activity facilitate a broader spatial distribution of particle trajectories throughout the bed height. Examining the effect of increased Q_{CZ} reveals a pronounced alignment of particle transport with the direction of the bulk-solids crossflow, as shown in **Figure 4-13**. This trend is evident in the normalized angular distributions: in the splash region, the proportion of particles transported in the crossflow direction increases from 42% to 60%, while in the dense bed, it increases from 60% to 80% under the conditions presented.

The proportional contributions of the splash and dense bed regions to net particle transport are summarized in **Figure A 10**. These observations can be further interpreted in the context of the transport mechanisms outlined in **Figure 2-3**. Under low fluidization (FN_{TZ} of 1.83), almost all transport occurs in the splash region (>94%), where lateral scattering, surface suspension, and sinking through the emulsion phase (mechanisms i–iii) can occur. As fluidization increases (FN_{TZ} of 3) and with higher conveying velocities, the contribution from the dense bed expands sharply, often exceeding 60%–70%. This indicates a shift in transport pathways from the splash region to the dense bed, where entrainment into bubble wakes, upward transport with bubbles, and release from bubble wakes (mechanisms iv–vi) can occur. While angular distribution analysis provides a useful means for distinguishing regional transport behaviors, it remains challenging to separate conclusively the individual mechanisms based solely on trajectory angles, highlighting the need for more refined classification methods.

To summarize, solids crossflow promotes a convective, plug-like transport of lean-phase particles under low fluidization conditions, shifting the dominant mechanism from dispersion to convection. However, solids dispersion remains comparable across both fluidization levels. The trajectory analysis supports this trend: at low fluidization, particle transport is largely confined to the splash region, whereas at higher fluidization it extends through the dense bed, indicating a clear shift in transport pathways.

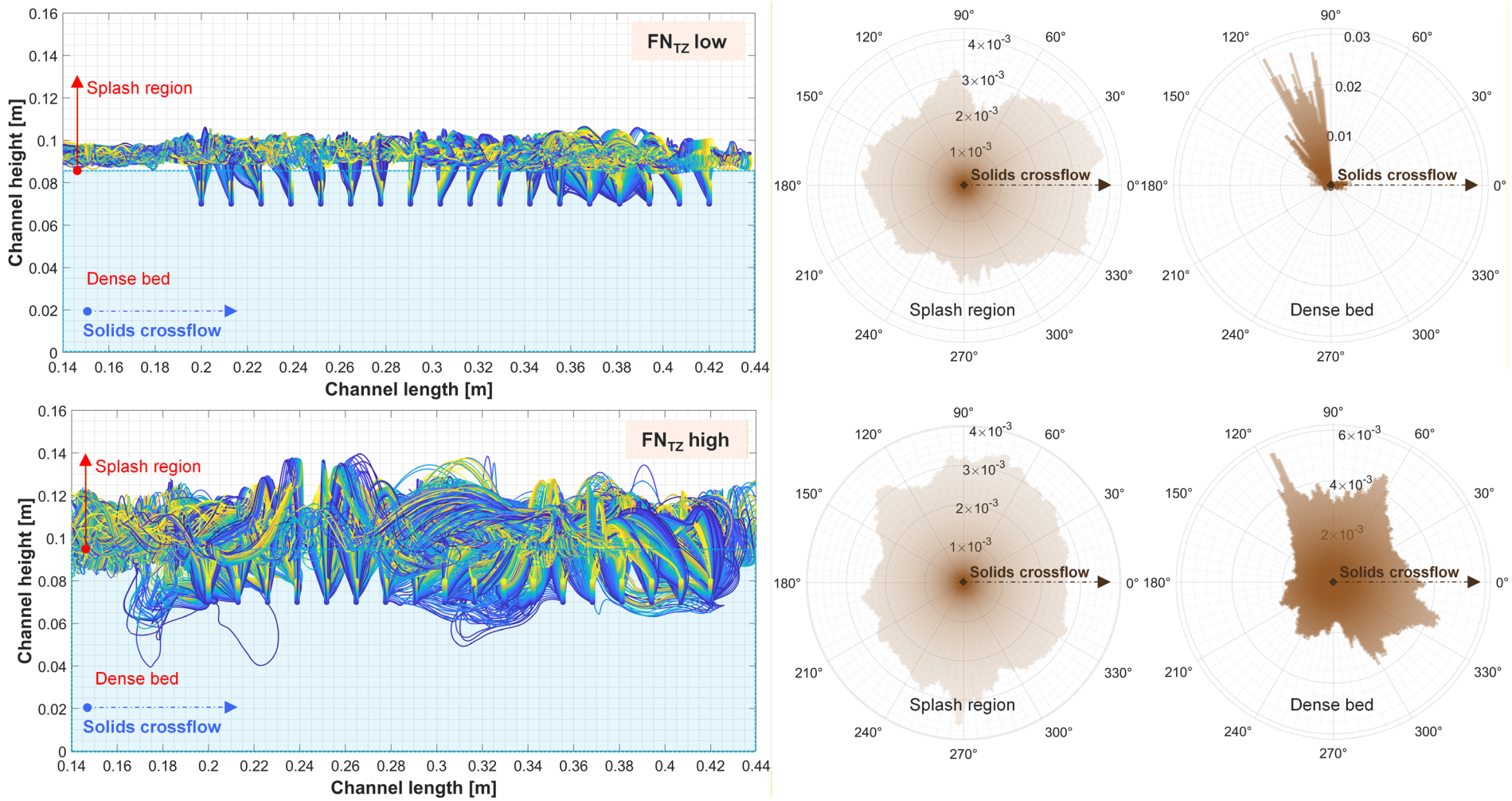

Figure 4-12: Effect of fluidization number (FN_{TZ}) on lean-phase particle transport. Left: Particle trajectories for low (top panel) and high (bottom panel) values of FN_{TZ}. Right: Normalized angular distributions in the splash region (light-brown) and dense bed (dark-brown). Fixed operating conditions: H, 0.08 m, Q_{CZ}, 1.43×10^{-2} m^3/s.

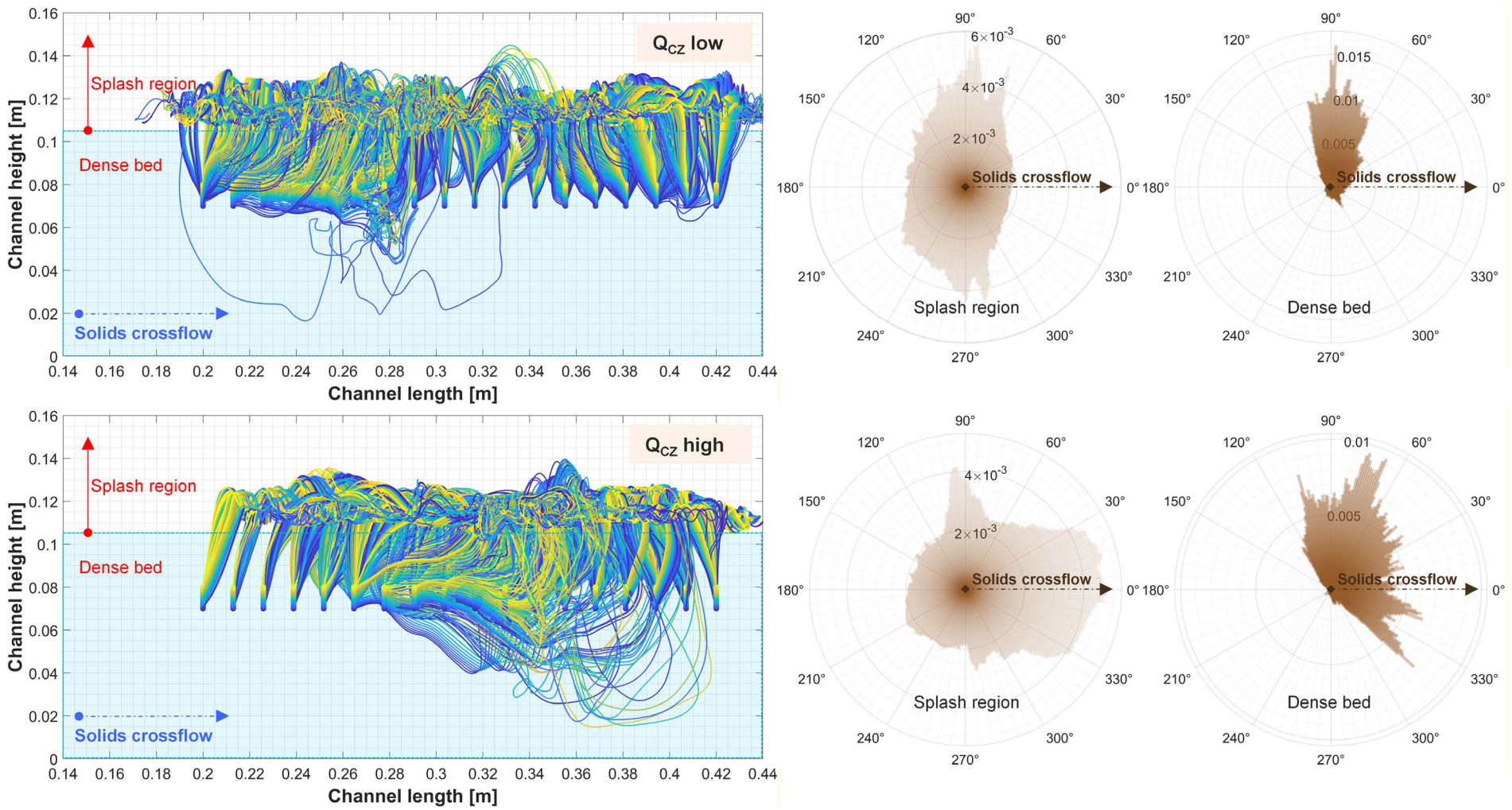

Figure 4-13: Effect of volumetric flow rate in the conveying zone (Q_{CZ}) on lean-phase particle transport. Left: Particle trajectories for low (top panel) and high (bottom panel) values of Q_{CZ}. Right: Normalized angular distributions in the splash region (light-brown) and dense bed (dark-brown). Fixed operating conditions: H, 0.08 m, FN_{TZ}, 1.83.

5. Conclusions

This thesis examines the dynamics of solids transport in bubbling fluidized beds with induced horizontal circulation. The experimental work employs a cold-flow model that is designed in accordance with Glicksman's simplified fluid-dynamic scaling laws. This setup operates at ambient temperature (20°C, fluidized with air) and simulates the conditions of a large-scale, high-temperature process (900°C) that uses silica sand (Geldart B-type solid) with an average particle size of 950 μm.

The study initially evaluates four different methods for quantifying horizontal solids flow: integral mass accumulation; differential mass accumulation; thermal tracing; and magnetic solids tracing (**RQ1**). Magnetic solids tracing proved to be the most effective method due to the resolution and quality of the acquired information, as well as the consistency of the measurements across a broad range of solids flow rates. In addition, the influences of three operational parameters—air flow rate in the conveying zone, bed height, and overall fluidization velocity—on the established solids flow rate were systematically investigated. The results show that increasing any of these parameters increases solids circulation, with the air flow rate in the conveying section having the most pronounced effect.

Subsequently, the study focused on examining the following conveying configurations: free solids splashing; confined solids splashing; slugging; solids entrainment; and directed gas injection (**RQ2**). Among these configurations, free solids splashing operating under the bubbling fluidization regime exhibited the highest efficiency in converting energy input into horizontal solids transport. The measured solids circulation rates ranged from 5×10^{-2} to 2×10^{3} kg/m²·s (up-scaled) for fluidization velocities of 1.9–4.3 m/s (up-scaled).

To characterize the global solids transport and evaluate how operational changes influence flow mechanisms and fluidization quality, the study employed 0D/1D modeling techniques (**RQ3**). The transient convection–dispersion model provided an accurate description of horizontal solids transport, with an average error of 12%–18% between predicted and measured solids tracer concentration transients across a range of operating conditions. A nearly linear relationship was observed between the dispersion coefficient and velocity in the direction of the solids crossflow, within the ranges of 2.41×10^{-4}–1.20×10^{-1} m²/s and 8.66×10^{-5}–1.73×10^{-1} m/s (up-scaled values), respectively; this trend is attributed to shear mixing from bed–wall friction. In addition, compartment model analysis demonstrated that an increased solids crossflow effectively reduces the extent of stagnant zones, indicating enhanced fluidization quality. To investigate in greater detail the influence of crossflow on solids flow structures and the observed linear relationship between transport parameters, a 3D Eulerian–Eulerian modeling framework was employed (**RQ4**). At low Péclet numbers, this interplay results in the formation of coherent, counter-rotating vortices along bubble paths. In contrast, at high Péclet numbers, convection becomes dominant, disrupting these macrostructures and producing more elongated solids flow patterns, which, in turn, enhance solids mixing. Microscale dispersion was found to be primarily driven by bubble- and eddy-induced turbulence, rather than by random particle motions or collisions.

The investigation of frictional losses induced by solids crossflow (**RQ5**) revealed a nonlinear relationship between the normalized pressure gradient and the mean horizontal solids velocity (ranges of 15–485 Pa/m and 0–0.101 m/s, respectively, on an up-scaled basis). The wall

shear stress values were in the range of 10–140 Pa, with corresponding wall shear rates of 2×10^{-3}–0.45 s^{-1}, exhibiting shear-thinning behavior. The solids velocity decreased with increasing channel width, highlighting the significant impact of bed–wall friction on solids transport. Furthermore, frictional resistance, as characterized by the Fanning friction factor, decreased with increasing Péclet number, reflecting reduced viscous losses and lower energy demand as convective transport became dominant. Rheological analysis using the $\mu(I)$-constitutive model confirmed that the system operated within the dense flow regime, with inertial numbers in the range of 10^{-6}–10^{-2} and effective friction coefficients in the range of 0.03–0.3.

Analysis of lean-phase particle transport (**RQ6**) revealed a positive correlation between dispersion and convection. The dispersion coefficients for lean-phase particles were consistently higher than those for bulk-phase solids, and they remained similar across varying fluidization levels. Under high fluidization conditions, the lean-phase particles exhibited lower horizontal velocities than the bulk phase. In contrast, at low fluidization numbers, they formed a uniform layer above the dense bed and were transported at higher horizontal velocities than the solids crossflow. The trajectory analysis indicated that the majority (70%–85%) of the lean-phase particles resided above the dense bed surface, where increased bulk solids crossflow and bed height promoted forward movement.

6. Future work

This thesis focuses on the characterization of transport mechanisms for both bulk-phase and lean-phase solids in bubbling fluidized beds with solids crossflow, with particular emphasis on thermochemical conversion applications. The work was performed under non-reactive conditions, using established scaling laws to ensure industrial relevance. However, in many industrial systems, particle properties evolve over time due to chemical reactions, thermal effects, or processing steps. In thermochemical reactors, fuel particles undergo transformations, such as reductions in size and density, ash formation, fines generation, and increased cohesion at high temperatures, each of which can significantly impact mixing, hydrodynamics, and process stability. Similarly, during pharmaceutical manufacturing, dynamic changes in the particle size distribution, surface properties, and moisture content during operations, such as granulation or drying, also affect the mixing and product uniformity. Future research should investigate how changes in particle properties under reactive or processing conditions influence the mixing, solids circulation, and interactions between solid phases over time.

The modeling approach used in this thesis for the bulk-phase solids flow, specifically the Eulerian–Eulerian CFD model, enables detailed characterization of both macro- and micro-scale transport mechanisms. This approach provides insights into vortex structures, bubble-driven eddies, and the interplay between convective and dispersive transport across a range of operating conditions. However, these models do not fully resolve the detailed particle–bubble and particle–particle interactions that can influence local mixing behaviors. Fully particle-resolved simulations, such as the Discrete Element Method (DEM), could in principle provide this level of detail. However, DEM simulations of dense beds with millions of particles are currently computationally prohibitive. Future research could therefore pursue hybrid or coarse-grained modeling strategies in conjunction with advanced experimental diagnostics to resolve and validate fine-scale phenomena. For the lean-phase particles, the current modeling framework uses a decoupled Eulerian–Eulerian field with Lagrangian tracking for the secondary phase, assuming that the lean-phase solids do not influence the dynamics of the bulk-phase solids. While this assumption is appropriate at low concentrations of lean-phase solids, at higher loadings or in systems where stronger coupling is expected, two-way or four-way coupling may be necessary to capture interactions with greater accuracy.

Furthermore, the analysis presented in this work is conducted on a section of the transport zone located sufficiently downstream of the conveying zone, where the flow is assumed to be stabilized, and the resulting flow structures are characteristic of the overall transport loop. Although the fluidization velocity in the conveying zone is the primary parameter influencing the solids crossflow, it is systematically controlled, and the conveying zone constitutes only a minor fraction of the horizontal flow path. Therefore, a detailed investigation of its dynamics was not required to meet the objectives of this study. However, in actual industrial designs (e.g., for pharmaceuticals, chemical reactors, food processing) in which the conveying and transport regions are closely integrated, careful analysis of the configuration that introduces a solids crossflow can be crucial for understanding the flow patterns and overall process performance.

This study employs non-intrusive magnetic solids tracing, which is restricted to surface-resolved measurements and requires signal conversion via a calibration factor to estimate concentration profiles. Therefore, future work should consider advanced diagnostics. In particular, there is a need for high-resolution, simultaneous measurements of the velocity and solids concentration within the dense region of the bed, where conventional methods cannot capture the full three-dimensional complexity of solids transport. Advancements in this area would enable more precise characterization of local mixing, phase distribution, and mechanisms of solids transport. This knowledge will be essential for improving the mechanistic understanding and validating high-resolution CFD models of crossflow systems.

References

[1] J.G. Yates, P. Lettieri, Fluidized-bed reactors: processes and operating conditions, Springer, 2016.

[2] H. Yiannoulakis, A. Yiagopoulos, C. Kiparissides, Recent developments in the particle size distribution modeling of fluidized-bed olefin polymerization reactors, Chem Eng Sci 56 (2001) 917–925.

[3] K. Daizo, O. Levenspiel, Fluidization engineering, Stoneham, MA (United States); Butterworth Publishers, 1991.

[4] F. Winter, B. Schratzer, Applications of fluidized bed technology in processes other than combustion and gasification, in: Fluidized Bed Technologies for Near-Zero Emission Combustion and Gasification, Elsevier, 2013: pp. 1005–1033.

[5] D.S. Pawar, R.K. Surwase, S.B. Bhamare, S.P. Pagar, Fluidized bed granulation: a promising technique, Int. J. Pharm. Sci. Rev. Res. 64 (2020) 133–140.

[6] R. Turton, G.I. Tardos, B.J. Ennis, Fluidized bed coating and granulation, Fluidization, Solids Handling and Processing 1 (1999) 331–334.

[7] P. Basu, Combustion and gasification in fluidized beds, CRC press, 2006.

[8] N.C. Shilton, K. Niranjan, Fluidization and its applications to food processing, Food Structure 12 (1993) 8.

[9] C. Turchiuli, Fluidization in food powder production, in: Handbook of Food Powders, Elsevier, 2013: pp. 178–199.

[10] J.R. Grace, X. Bi, N. Ellis, Essentials of fluidization technology, John Wiley & Sons, 2020.

[11] X. Guan, N. Yang, Modeling of co-current and counter-current bubble columns with an extended EMMS approach, Particuology 44 (2019) 126–135. https://doi.org/https://doi.org/10.1016/j.partic.2018.07.009.

[12] R.H. Wilhelm, S. Valentine, The Fluidized Bed., Ind Eng Chem 43 (1951) 1199–1203.

[13] H. Thunman, B. Leckner, Co-current and counter-current fixed bed combustion of biofuel—a comparison☆, Fuel 82 (2003) 275–283. https://doi.org/https://doi.org/10.1016/S0016-2361(02)00289-2.

[14] T.A. Aldugman, M. Cui, A. Alzailaie, A. Alhareth, K. Langley, L. Alfilfil, K. Almajnouni, J. Gascon, S. Thoroddsen, P. Castaño, Comparative analysis of counter-current and co-current downer reactors using particle image velocimetry and computational particle-fluid dynamics, Chemical Engineering Journal Advances 21 (2025) 100687. https://doi.org/https://doi.org/10.1016/j.ceja.2024.100687.

[15] B. Leckner, Fluidized bed combustion: Achievements and problems, Symposium (International) on Combustion 26 (1996) 3231–3241. https://doi.org/https://doi.org/10.1016/S0082-0784(96)80169-X.

[16] P. Salatino, R. Solimene, Mixing and segregation in fluidized bed thermochemical conversion of biomass, Powder Technol 316 (2017) 29–40.

[17] B. Leckner, Fluidized bed combustion: mixing and pollutant limitation, Prog Energy Combust Sci 24 (1998) 31–61.

[18] F. Niklasson, H. Thunman, F. Johnsson, B. Leckner, Estimation of solids mixing in a fluidized-bed combustor, Ind Eng Chem Res 41 (2002) 4663–4673.

[19] E. Diez, K. Meyer, A. Bück, E. Tsotsas, S. Heinrich, Influence of process conditions on the product properties in a continuous fluidized bed spray granulation process, Chemical Engineering Research and Design 139 (2018) 104–115. https://doi.org/10.1016/j.cherd.2018.09.032.

[20] C. Neugebauer, E. Diez, L. Mielke, S. Palis, A. Bück, E. Tsotsas, A. Kienle, S. Heinrich, Dynamics of spray granulation in continuously operated horizontal fluidized beds, in: Dynamic Flowsheet Simulation of Solids Processes, Springer, 2020: pp. 67–107.

[21] G. Wang, Y. Chen, H. Zhou, Z. Fang, L. Lyu, J. Lu, Research on particle retention in continuous horizontal fluidized bed based on CFD-DEM method, Powder Technol 433 (2024) 119229.

[22] E. Diez, P. Kieckhefen, K. Meyer, A. Bück, E. Tsotsas, S. Heinrich, Particle dynamics in a multi-staged fluidized bed: Particle transport behavior on micro-scale by discrete particle modelling, Advanced Powder Technology 30 (2019) 2014–2031. https://doi.org/10.1016/j.apt.2019.05.025.

[23] S. Parvathaneni, B. Kodukula, M.W. Andrade, Iron-Ore Reduction in Fluidized Beds: Review of Commercial Technologies, Status, and Challenges, Ind Eng Chem Res 63 (2024) 18724–18733. https://doi.org/10.1021/acs.iecr.4c02282.

[24] P.U. Foscolo, A. Germanà, N. Jand, S. Rapagnà, Design and cold model testing of a biomass gasifier consisting of two interconnected fluidized beds, Powder Technol 173 (2007) 179–188.

[25] S.K. Wee, V.S. Chok, C. Srinivasakannan, H.B. Chua, H.M. Yan, Fluidization quality study in a compartmented fluidized bed gasifier (cfbg), Energy & Fuels 22 (2008) 61–66.

[26] W. Kong, B. Wang, J. Baeyens, S. Li, H. Ke, T. Tan, H. Zhang, Solids mixing in a shallow cross-flow bubbling fluidized bed, Chem Eng Sci 187 (2018) 213–222. https://doi.org/10.1016/j.ces.2018.04.073.

[27] S. Geng, Y. Qian, J. Zhan, H. Zhang, G. Xu, X. Liu, Prediction of solids residence time distribution in cross-flow bubbling fluidized bed, Powder Technol 320 (2017) 555–564. https://doi.org/10.1016/j.powtec.2017.07.085.

[28] E. Sette, D. Pallarès, F. Johnsson, Influence of bulk solids cross-flow on lateral mixing of fuel in dual fluidized beds, Fuel Processing Technology 140 (2015) 245–251. https://doi.org/10.1016/j.fuproc.2015.09.017.

[29] K. Vollmari, H. Kruggel-Emden, Numerical and experimental analysis of particle residence times in a continuously operated dual-chamber fluidized bed, Powder Technol 338 (2018) 625–637. https://doi.org/10.1016/j.powtec.2018.07.061.

[30] L. Hua, H. Zhao, J. Li, Q. Zhu, J. Wang, Solid residence time distribution in a cross-flow dense fluidized bed with baffles, Chem Eng Sci 200 (2019) 320–335. https://doi.org/https://doi.org/10.1016/j.ces.2019.01.054.

[31] L. Gan, X. Lu, Q. Wang, Q. Hu, Y. Chen, J. Xu, Experimental study on lateral mixing of particles in a quasi-slot-rectangular spouted bed, Powder Technol 243 (2013) 1–8. https://doi.org/10.1016/j.powtec.2013.03.021.

[32] K. Meyer, A. Bück, E. Tsotsas, Determination of particle exchange rates at over-flow weirs in horizontal fluidised beds by particle tracking velocimetry, Particuology 32 (2017) 1–9. https://doi.org/10.1016/j.partic.2016.09.007.

[33] P. Bachmann, A. Bück, E. Tsotsas, Investigation of the residence time behavior of particulate products and correlation for the Bodenstein number in horizontal fluidized beds, Powder Technol 301 (2016) 1067–1076. https://doi.org/10.1016/j.powtec.2016.07.045.

[34] K. Chen, P. Bachmann, A. Bück, M. Jacob, E. Tsotsas, Experimental study and modeling of particle drying in a continuously-operated horizontal fluidized bed, Particuology 34 (2017) 134–146. https://doi.org/10.1016/j.partic.2017.02.003.

[35] Y. Zhang, N. Abatzoglou, S. Hudon, P.P. Lapointe-Garant, J.S. Simard, Dynamics of heat-sensitive pharmaceutical granules dried in a horizontal fluidized bed combined with a screw conveyor, Chemical Engineering and Processing - Process Intensification 167 (2021). https://doi.org/10.1016/j.cep.2021.108516.

[36] Z. Zou, Y. Zhao, H. Zhao, L. Zhang, Z. Xie, H. Li, Q. Zhu, CFD simulation of solids residence time distribution in a multi-compartment fluidized bed, Chin J Chem Eng 25 (2017) 1706–1713. https://doi.org/10.1016/j.cjche.2017.02.010.

[37] F.A. Zenz, D.F. Othmer, Fluidization and fluid-particle systems, in: 1960. https://api.semanticscholar.org/CorpusID:93826163.

[38] J.R. van Ommen, R.F. Mudde, Measuring the gas-solids distribution in fluidized beds--a review, International Journal of Chemical Reactor Engineering 6 (2008).

[39] J.J. Burkell, J.R. Grace, J. Zhao, C.J. Lim, Measurement of solids circulation rates in circulating fluidized beds, in: Circulating Fluidized Bed Technology, Elsevier, 1988: pp. 501–509.

[40] T. Pugsley, D. Lapointe, B. Hirschberg, J. Werther, Exit Effects in Circulating Fluidized Bed Risers, Canadian Journal of Chemical Engineering 75 (1997) 1001–1010. https://doi.org/10.1002/cjce.5450750602.

[41] H. Taofeeq, S. Aradhya, J. Shao, M. Al-Dahhan, Advance optical fiber probe for simultaneous measurements of solids holdup and particles velocity using simple calibration methods for gas-solid fluidization systems, Flow Measurement and Instrumentation 63 (2018) 18–32. https://doi.org/https://doi.org/10.1016/j.flowmeasinst.2018.07.001.

[42] H. Zhu, J. Zhu, G. Li, F. Li, Detailed measurements of flow structure inside a dense gas–solids fluidized bed, Powder Technol 180 (2008) 339–349. https://doi.org/https://doi.org/10.1016/j.powtec.2007.02.043.

[43] C. Song, Q. Liu, J. Wang, A.D. Bragg, S. Wang, X. Gao, Y. Li, J. Wen, Z. Zhang, Estimation of Particle Dispersion Characteristics in a Fluidized Bed with the Binary Mixture of Geldart A and B Types Using the Optical Fiber Probe Method, Ind Eng Chem Res 63 (2024) 7807–7820. https://doi.org/10.1021/acs.iecr.3c04367.

[44] A. Gil, C. Cortés, L.M. Romeo, J. Velilla, Gas-particle flow inside cyclone diplegs with pneumatic extraction, Powder Technol 128 (2002) 78–91. https://doi.org/https://doi.org/10.1016/S0032-5910(02)00215-2.

[45] D. Westphalen, L. Glicksman, Lateral solid mixing measurements in circulating fluidized beds, Powder Technol 82 (1995) 153–167. https://doi.org/https://doi.org/10.1016/0032-5910(94)02909-8.

[46] M.H. Rahman, X.T. Bi, J.R. Grace, C.J. Lim, Measurement of solids circulation rate in a high-temperature dual fluidized bed pilot plant, Powder Technol 316 (2017) 658–669. https://doi.org/https://doi.org/10.1016/j.powtec.2017.01.073.

[47] D. Liu, X. Chen, Quantifying lateral solids mixing in a fluidized bed by modeling the thermal tracing method, AIChE Journal 58 (2012) 745–755. https://doi.org/https://doi.org/10.1002/aic.12627.

[48] H. Tsujimoto, T. Yokoyama, C.C. Huang, I. Sekiguchi, Monitoring particle fluidization in a fluidized bed granulator with an acoustic emission sensor, Powder Technol 113 (2000) 88–96. https://doi.org/https://doi.org/10.1016/S0032-5910(00)00205-9.

[49] Y. Zhou, L. Yang, Y. Lu, X. Hu, X. Luo, H. Chen, Flow regime identification in gas-solid two-phase fluidization via acoustic emission technique, Chemical Engineering Journal 334 (2018) 1484–1492. https://doi.org/https://doi.org/10.1016/j.cej.2017.11.050.

[50] J. Wang, C. Ren, Y. Yang, L. Hou, Characterization of Particle Fluidization Pattern in a Gas Solid Fluidized Bed Based on Acoustic Emission (AE) Measurement, Ind Eng Chem Res 48 (2009) 8508–8514. https://doi.org/10.1021/ie8018774.

[51] M. Kashyap, B. Chalermsinsuwan, D. Gidaspow, Measuring turbulence in a circulating fluidized bed using PIV techniques, Particuology 9 (2011) 572–588. https://doi.org/10.1016/j.partic.2011.06.007.

[52] J.A. Laverman, I. Roghair, M. van S. Annaland, H. Kuipers, Investigation into the hydrodynamics of gas–solid fluidized beds using particle image velocimetry coupled with digital image analysis, Can J Chem Eng 86 (2008) 523–535. https://doi.org/10.1002/cjce.20054.

[53] Y. He, S. Yan, T. Wang, B. Jiang, Y. Huang, Hydrodynamic characteristics of gas-irregular particle two-phase flow in a bubbling fluidized bed: An experimental and numerical study, Powder Technol 287 (2016) 264–276. https://doi.org/https://doi.org/10.1016/j.powtec.2015.10.012.

[54] A. Busciglio, G. Vella, G. Micale, On the bubbling dynamics of binary mixtures of powders in 2D gas-solid fluidized beds, Powder Technol 231 (2012) 21–34. https://doi.org/https://doi.org/10.1016/j.powtec.2012.07.033.

[55] G.M. Castilla, A. Larsson, L. Lundberg, F. Johnsson, D. Pallarès, A novel experimental method for determining lateral mixing of solids in fluidized beds–Quantification of the splash-zone contribution, Powder Technol 370 (2020) 96–103.

[56] M.J.A. de Munck, M. Dullemond, E.A.J.F. Peters, J.A.M. Kuipers, Experimental gas-fluidized bed drying study on the segregation and mixing dynamics for binary and ternary solids, Chemical Engineering Journal 465 (2023) 142756. https://doi.org/https://doi.org/10.1016/j.cej.2023.142756.

[57] H.R. Norouzi, N. Mostoufi, Z. Mansourpour, R. Sotudeh-Gharebagh, J. Chaouki, Characterization of solids mixing patterns in bubbling fluidized beds, Chemical Engineering Research and Design 89 (2011) 817–826. https://doi.org/10.1016/j.cherd.2010.10.014.

[58] N. Mostoufi, J. Chaouki, Flow structure of the solids in gas-solid fluidized beds, Chem Eng Sci 59 (2004) 4217–4227. https://doi.org/10.1016/j.ces.2004.06.006.

[59] S. Roy, H.J. Pant, S. Roy, Velocity characterization of solids in binary fluidized beds, Chem Eng Sci 246 (2021) 116883. https://doi.org/https://doi.org/10.1016/j.ces.2021.116883.

[60] D.C. Guío-Pérez, T. Pröll, H. Hofbauer, Solids residence time distribution in the secondary reactor of a dual circulating fluidized bed system, Chem Eng Sci 104 (2013) 269–284. https://doi.org/10.1016/j.ces.2013.08.047.

[61] D.C. Guío-Pérez, F. Johnsson, D. Pallarès, Experimental investigation of the lateral mixing of large and light particles immersed in a fluidized bed, Fuel 346 (2023) 128343. https://doi.org/10.1016/j.fuel.2023.128343.

[62] A. Köhler, A. Rasch, D. Pallarès, F. Johnsson, Experimental characterization of axial fuel mixing in fluidized beds by magnetic particle tracking, Powder Technol 316 (2017) 492–499. https://doi.org/https://doi.org/10.1016/j.powtec.2016.12.093.

[63] J.M. Weber, J.S. Mei, Bubbling fluidized bed characterization using Electrical Capacitance Volume Tomography (ECVT), Powder Technol 242 (2013) 40–50. https://doi.org/https://doi.org/10.1016/j.powtec.2013.01.044.

[64] G. Qiu, J. Ye, H. Wang, W. Yang, Investigation of flow hydrodynamics and regime transition in a gas–solids fluidized bed with different riser diameters, Chem Eng Sci 116 (2014) 195–207. https://doi.org/https://doi.org/10.1016/j.ces.2014.05.006.

[65] B.K. Singh, S. Roy, V. V Buwa, Bubbling/slugging flow behavior in a cylindrical fluidized bed: ECT measurements and two-fluid simulations, Chemical Engineering Journal 383 (2020) 123120. https://doi.org/https://doi.org/10.1016/j.cej.2019.123120.

[66] H. Wang, G. Qiu, J. Ye, W. Yang, Experimental study and modelling on gas–solid flow in a lab-scale fluidised bed with Wurster tube, Powder Technol 300 (2016) 14–27. https://doi.org/10.1016/j.powtec.2016.01.025.

[67] W.-C. Yang, Handbook of fluidization and fluid-particle systems, CRC press, 2003.

[68] D. Pallares, P.A. Díez, F. Johnsson, Experimental analysis of fuel mixing patterns in a fluidized bed, (2007).

[69] E. Sette, D. Pallarès, F. Johnsson, F. Ahrentorp, A. Ericsson, C. Johansson, Magnetic tracer-particle tracking in a fluid dynamically down-scaled bubbling fluidized bed, Fuel Processing Technology 138 (2015) 368–377. https://doi.org/10.1016/j.fuproc.2015.06.016.

[70] A. Köhler, E. Cano-Pleite, A. Soria-Verdugo, D. Pallarès, F. Johnsson, Modeling the motion of fuel particles in a fluidized bed, Fuel 305 (2021) 121424. https://doi.org/https://doi.org/10.1016/j.fuel.2021.121424.

[71] O. Levenspiel, Tracer technology: modeling the flow of fluids, Springer Science & Business Media, 2011.

[72] Y. Li, J. Rong, K. Zhang, X. Fan, Impact of solid and gas flow patterns on solid mixing in bubbling fluidized beds, Chemical Engineering Research and Design 132 (2018) 1037–1053. https://doi.org/10.1016/j.cherd.2017.12.014.

[73] V. Jiradilok, D. Gidaspow, R.W. Breault, Computation of gas and solid dispersion coefficients in turbulent risers and bubbling beds, Chem Eng Sci 62 (2007) 3397–3409. https://doi.org/10.1016/j.ces.2007.01.084.

[74] A. Köhler, D. Pallarès, Mixing of Large Solids in Fluidized Beds Semiempirical Modeling and Experiments with Application to Fuel Mixing, Chalmers Tekniska Hogskola (Sweden), 2021.

[75] A. Einstein, Investigations on the Theory of the Brownian Movement, Courier Corporation, 1956.

[76] K. Luo, F. Wu, S. Yang, J. Fan, CFD-DEM study of mixing and dispersion behaviors of solid phase in a bubbling fluidized bed, Powder Technol 274 (2015) 482–493. https://doi.org/10.1016/j.powtec.2015.01.046.

[77] S. Yang, K. Luo, M. Fang, K. Zhang, J. Fan, Parallel CFD-DEM modeling of the hydrodynamics in a lab-scale double slot-rectangular spouted bed with a partition plate, Chemical Engineering Journal 236 (2014) 158–170. https://doi.org/10.1016/j.cej.2013.09.082.

[78] M. Farha, H. Ström, D.C. Guío-Pérez, D. Pallarès, Spatially-resolved characterization of the flow structure in a bubbling fluidized bed with solids crossflow, (2025).

[79] D. Gidaspow, J. Jung, R.K. Singh, Hydrodynamics of fluidization using kinetic theory: An emerging paradigm 2002 Flour-Daniel lecture, in: Powder Technol, 2004: pp. 123–141. https://doi.org/10.1016/j.powtec.2004.09.025.

[80] J. Jung, D. Gidaspow, I.K. Gamwo, Measurement of Two Kinds of Granular Temperatures, Stresses, and Dispersion in Bubbling Beds, Industrial & Engineering Chemistry Research 44 (2005) 1329–1341. https://doi.org/10.1021/ie0496838.

[81] B. Chalermsinsuwan, P. Piumsomboon, D. Gidaspow, Kinetic theory based computation of PSRI riser: Part I—Estimate of mass transfer coefficient, Chem Eng Sci 64 (2009) 1195–1211. https://doi.org/10.1016/j.ces.2008.11.010.

[82] T. Samruamphianskun, P. Piumsomboon, B. Chalermsinsuwan, Computation of system turbulences and dispersion coefficients in circulating fluidized bed downer using CFD simulation, Chemical Engineering Research and Design 90 (2012) 2164–2178. https://doi.org/10.1016/j.cherd.2012.06.009.

[83] P.N. Rowe, B.A. Partridge, A.G. Cheney, G.A. Henwood, E. Lyall, Mechanisms of solids mixing in fluidised beds, Transactions of the Institution of Chemical Engineers and the Chemical Engineer 43 (1965) T271.

[84] I.N.M. Woollard, O.E. Potter, Solids mixing in fluidized beds, AIChE Journal 14 (1968) 388–391.

[85] J. Werther, Bubble chains in large diameter gas fluidized beds, International Journal of Multiphase Flow 3 (1977) 367–381.

[86] Y.F. Shi, L.T. Fan, Lateral mixing of solids in batch gas-solids fluidized beds, Industrial & Engineering Chemistry Process Design and Development 23 (1984) 337–341.

[87] R.P. Chhabra, S.A. Patel, Bubbles, drops, and particles in non-Newtonian fluids, CRC press, 2023.

[88] R.P. Chhabra, S.A. Patel, Non-Newtonian flow and applied rheology: engineering applications, Elsevier, 2025.

[89] P. Coussot, Rheometry of pastes, suspensions, and granular materials: applications in industry and environment, (2005).

[90] A. Bhattad, Review on viscosity measurement: devices, methods and models., J Therm Anal Calorim 148 (2023).

[91] W. Kozicki, C.H. Chou, C. Tiu, Non-Newtonian flow in ducts of arbitrary cross-sectional shape, Chem Eng Sci 21 (1966) 665–679. https://doi.org/10.1016/0009-2509(66)80016-7.

[92] W. Kozicki, C. Tiu, Non-newtonian flow through open channels, Can J Chem Eng 45 (1967) 127–134. https://doi.org/10.1002/cjce.5450450302.

[93] C. Tiu, W. Kozicki, T.Q. Phung, Geometric parameters for some flow channels, Can J Chem Eng 46 (1968) 389–393. https://doi.org/10.1002/cjce.5450460601.

[94] W. Kozicki, C. Tiu, Improved parametric characterization of flow geometries, Can J Chem Eng 49 (1971) 562–569. https://doi.org/10.1002/cjce.5450490503.

[95] F. Delplace, J.C. Leuliet, Generalized Reynolds number for the flow of power law fluids in cylindrical ducts of arbitrary cross-section, The Chemical Engineering Journal and the Biochemical Engineering Journal 56 (1995) 33–37. https://doi.org/10.1016/0923-0467(94)02849-6.

[96] M. Kostic, J.P. Hartnett, Predicting turbulent friction factors of non-newtonian fluids in noncircular ducts, International Communications in Heat and Mass Transfer 11 (1984) 345–352. https://doi.org/10.1016/0735-1933(84)90062-9.

[97] M. Ayas, J. Skocilas, T. Jirout, A practical method for predicting the friction factor of power-law fluids in a rectangular duct, Chem Eng Commun 206 (2019) 1310–1316. https://doi.org/10.1080/00986445.2018.1557153.

[98] A.B. Metzner, J.C. Reed, Flow of non-newtonian fluids—correlation of the laminar, transition, and turbulent-flow regions, AIChE Journal 1 (1955) 434–440. https://doi.org/10.1002/aic.690010409.

[99] F. da Cruz, S. Emam, M. Prochnow, J.-N. Roux, F. Chevoir, Rheophysics of dense granular materials: Discrete simulation of plane shear flows, Phys Rev E 72 (2005). https://doi.org/10.1103/physreve.72.021309.

[100] P. Jop, Y. Forterre, O. Pouliquen, A constitutive law for dense granular flows, Nature 441 (2006) 727–730. https://doi.org/10.1038/nature04801.

[101] F. Chevoir, J.-N. Roux, F. da Cruz, P.G. Rognon, G. Koval, Friction law in dense granular flows, Powder Technol 190 (2009) 264–268. https://doi.org/10.1016/j.powtec.2008.04.061.

[102] G.D.R. MiDi, On dense granular flows, The European Physical Journal E 14 (2004) 341–365. https://doi.org/10.1140/epje/i2003-10153-0.

[103] K. Myöhänen, T. Hyppänen, A Three-Dimensional Model Frame for Modelling Combustion and Gasification in Circulating Fluidized Bed Furnaces, International Journal of Chemical Reactor Engineering 9 (2012). https://doi.org/10.1515/1542-6580.2571.

[104] X.T. Li, J.R. Grace, C.J. Lim, A.P. Watkinson, H.P. Chen, J.R. Kim, Biomass gasification in a circulating fluidized bed, Biomass Bioenergy 26 (2004) 171–193. https://doi.org/10.1016/S0961-9534(03)00084-9.

[105] X. Ke, M. Engblom, L. Cheng, L. Chen, R. Cai, L. Hupa, J. Lyu, H. Yang, M. Zhang, Modeling and experimental investigation on the fuel particle heat-up and devolatilization behavior in a fluidized bed, Fuel 288 (2021). https://doi.org/10.1016/j.fuel.2020.119794.

[106] H. Luo, X. Wang, X. Wu, L. Niedzwiecki, H. Pawlak-Kruczek, X. Liu, Q. Xiong, Multi-fluid modeling of heat transfer in bubbling fluidized bed with thermally-thick particles featuring intra-particle temperature inhomogeneity, Chemical Engineering Journal 460 (2023). https://doi.org/10.1016/j.cej.2023.141813.

[107] H.. . K. Versteeg, W.. . Malalasekera, An introduction to computational fluid dynamics: The finite volume method, Second edition, Pearson Prentice Hall, 2007.

[108] J. Ding, D. Gidaspow, A bubbling fluidization model using kinetic theory of granular flow, AIChE Journal 36 (1990) 523–538. https://doi.org/10.1002/aic.690360404.

[109] V. Jiradilok, D. Gidaspow, S. Damronglerd, W.J. Koves, R. Mostofi, Kinetic theory based CFD simulation of turbulent fluidization of FCC particles in a riser, Chem Eng Sci 61 (2006) 5544–5559. https://doi.org/10.1016/j.ces.2006.04.006.

[110] R. Jackson, M.D. Shattuck, The Dynamics of Fluidized Particles, in: 2000. https://api.semanticscholar.org/CorpusID:121740919.

[111] S. Yuu, H. Nishikawa, T. Umekage, Numerical simulation of air and particle motions in group-B particle turbulent fluidized bed, 2001. www.elsevier.comrlocaterpowtec.

[112] N. Xie, F. Battaglia, S. Pannala, Effects of using two- versus three-dimensional computational modeling of fluidized beds. Part I, hydrodynamics, Powder Technol 182 (2008) 1–13. https://doi.org/10.1016/j.powtec.2007.07.005.

[113] B. Lu, W. Wang, J. Li, Searching for a mesh-independent sub-grid model for CFD simulation of gas-solid riser flows, Chem Eng Sci 64 (2009) 3437–3447. https://doi.org/10.1016/j.ces.2009.04.024.

[114] M.A. van der Hoef, M. van Sint Annaland, N.G. Deen, J.A.M. Kuipers, Numerical simulation of dense gas-solid fluidized beds: A multiscale modeling strategy, Annu Rev Fluid Mech 40 (2008) 47–70. https://doi.org/10.1146/annurev.fluid.40.111406.102130.

[115] N.G. Deen, E.A.J.F. Peters, J.T. Padding, J.A.M. Kuipers, Review of direct numerical simulation of fluid–particle mass, momentum and heat transfer in dense gas–solid flows, Chem Eng Sci 116 (2014) 710–724. https://doi.org/https://doi.org/10.1016/j.ces.2014.05.039.

[116] N.G. Deen, M. Van Sint Annaland, M.A. Van der Hoef, J.A.M. Kuipers, Review of discrete particle modeling of fluidized beds, Chem Eng Sci 62 (2007) 28–44. https://doi.org/10.1016/j.ces.2006.08.014.

[117] K. Takabatake, Y. Mori, J.G. Khinast, M. Sakai, Numerical investigation of a coarse-grain discrete element method in solid mixing in a spouted bed, Chemical Engineering Journal 346 (2018) 416–426. https://doi.org/https://doi.org/10.1016/j.cej.2018.04.015.

[118] J. Lin, K. Luo, S. Wang, C. Hu, J. Fan, An augmented coarse-grained CFD-DEM approach for simulation of fluidized beds, Advanced Powder Technology 31 (2020) 4420–4427. https://doi.org/https://doi.org/10.1016/j.apt.2020.09.014.

[119] Z.(赵振江) Zhao, L.(周岭) Zhou, L.(白玲) Bai, M.A. El-Emam, R. Agarwal, Modeling and validation of coarse-grained computational fluid dynamics–discrete element method for dense gas–solid flow simulation in a bubbling fluidized bed, Physics of Fluids 35 (2023) 043310. https://doi.org/10.1063/5.0146264.

[120] M.J. Andrews, P.J. O'Rourke, The multiphase particle-in-cell (MP-PIC) method for dense particulate flows, International Journal of Multiphase Flow 22 (1996) 379–402. https://doi.org/https://doi.org/10.1016/0301-9322(95)00072-0.

[121] N.A. Patankar, D.D. Joseph, Modeling and numerical simulation of particulate flows by the Eulerian–Lagrangian approach, International Journal of Multiphase Flow 27 (2001) 1659–1684. https://doi.org/https://doi.org/10.1016/S0301-9322(01)00021-0.

[122] J. Xie, W. Zhong, B. Jin, Y. Shao, Y. Huang, Eulerian–Lagrangian method for three-dimensional simulation of fluidized bed coal gasification, Advanced Powder Technology 24 (2013) 382–392. https://doi.org/https://doi.org/10.1016/j.apt.2012.09.001.

[123] K. Luo, J. Tan, Z. Wang, J. Fan, Particle-resolved direct numerical simulation of gas-solid dynamics in experimental fluidized beds, AIChE Journal 62 (2016) 1917–1932. https://doi.org/10.1002/aic.15186.

[124] N.G. Deen, S.H.L. Kriebitzsch, M.A. van der Hoef, J.A.M. Kuipers, Direct numerical simulation of flow and heat transfer in dense fluid–particle systems, Chem Eng Sci 81 (2012) 329–344. https://doi.org/https://doi.org/10.1016/j.ces.2012.06.055.

[125] Y. Tsuji, T. Kawaguchi, T. Tanaka, Discrete particle simulation of two-dimensional fluidized bed, 1993.

[126] B.P.B. Hoomans, J.A.M. Kuipers, W.J. Briels, W.P.M. Van Swaaij, DISCRETE PARTICLE SIMULATION OF BUBBLE AND SLUG FORMATION IN A TWO-DIMENSIONAL GAS-FLUIDISED BED: A HARD-SPHERE APPROACH, 1996.

[127] B.H. Xu, A.B. Yu, Numerical simulation of the gas-solid flow in a fluidized bed by combining discrete particle method with computational fluid dynamics, 1997.

[128] K.D. Kafui, C. Thornton, M.J. Adams, Discrete particle-continuum muid modelling of gas-solid uidised beds, 2002. www.elsevier.com/locate/ces.

[129] E. Sette, D. Pallarès, F. Johnsson, Experimental evaluation of lateral mixing of bulk solids in a fluid-dynamically down-scaled bubbling fluidized bed, Powder Technol 263 (2014) 74–80. https://doi.org/10.1016/j.powtec.2014.04.091.

[130] M. Syamlal, W. Rogers, T.J. OBrien, MFIX documentation theory guide, USDOE Morgantown Energy Technology Center (METC), WV (United States), 1993.

[131] D. Gidaspow, Computation of hydrodynamics using kinetic theory, Office of Scientific and Technical Information (OSTI), 1991. https://doi.org/10.2172/5686161.

[132] D. Gidaspow, Multiphase flow and fluidization: continuum and kinetic theory descriptions, Academic press, 1994.

[133] H. Arastoopour, D. Gidaspow, E. Abbasi, Conservation and Constitutive Equations for Fluid–Particle Flow Systems, in: Computational Transport Phenomena of Fluid-Particle Systems, Springer, 2016: pp. 9–44.

[134] M. Syamlal, MULTIPHASE HYDRODYNAMICS OF GAS-SOLIDS FLOW (MULTIPHASE, TWO PHASE, HYDRODYNAMICS), Illinois Institute of Technology, 1985.

[135] H. Arastoopour, D. Gidaspow, E. Abbasi, Computational transport phenomena of fluid-particle systems, Springer, 2017.

[136] R. Di Felice, M. Rotondi, Fluid-particle drag force in binary-solid suspensions, International Journal of Chemical Reactor Engineering 10 (2012).

[137] L.G. Gibilaro, K. Gallucci, R. Di Felice, P. Pagliai, On the apparent viscosity of a fluidized bed, Chem Eng Sci 62 (2007) 294–300.

[138] K. Zhao, H. Thunman, D. Pallarès, H. Ström, Control of the solids retention time by multi-staging a fluidized bed reactor, Fuel Processing Technology 167 (2017) 171–182.

[139] L.R. Glicksman, Scaling relationships for fluidized beds, Chem Eng Sci 43 (1988) 1419–1421. https://doi.org/10.1016/0009-2509(88)85118-2.

[140] L.R. Glicksman, M. Hyre, K. Woloshun, Simplified scaling relationships for fluidized beds, Powder Technol 77 (1993) 177–199. https://doi.org/10.1016/0032-5910(93)80055-f.

[141] P. Mirek, Influence of the model scale on hydrodynamic scaling in CFB boilers, Brazilian Journal of Chemical Engineering 33 (2016) 885–896.

[142] T. Djerf, D. Pallarès, F. Johnsson, Solids flow patterns in large-scale circulating fluidised bed boilers: Experimental evaluation under fluid-dynamically down-scaled conditions, Chem Eng Sci 231 (2021) 116309. https://doi.org/10.1016/j.ces.2020.116309.

[143] M. Farha, D.C. Guío-Pérez, F. Johnsson, D. Pallarès, Comparison of solids conveying mechanisms in fluidized bed systems – Alternatives to riser, Chem Eng Sci 317 (2025) 122000. https://doi.org/10.1016/j.ces.2025.122000.

[144] J. Chandler, H. Obermaier, K.I. Joy, Interpolation-based pathline tracing in particle-based flow visualization, IEEE Trans Vis Comput Graph 21 (2014) 68–80.

[145] M. Farha, Flow Characterization in Bubbling Fluidized Beds with Solids Crossflow, Chalmers Tekniska Hogskola (Sweden), 2024.

[146] T. Hirama, M. Ishida, T. Shirai, The Lateral Dispersion of Solid Particles in Fluidized Beds, Kagaku Kogaku Ronbunshu 1 (1975) 272–276.

[147] Y.F. Shi, M.X. Gu, Lateral mixing of solids in fluidized beds with partitions, in: World Congress III of Chemical Engineering, Tokyo, Japan, 1986: pp. 465–468.

[148] M. Farha, D.C. Guío-Pérez, F. Johnsson, D. Pallarès, Frictional losses in a bubbling fluidized bed with horizontal flow of solids, International Journal of Multiphase Flow 189 (2025) 105192. https://doi.org/10.1016/j.ijmultiphaseflow.2025.105192.

[149] D.C. Guío-Pérez, A. Köhler, E. Arango, J. Keller, K. Umeki, D. Pallarès, Biochar production in large-scale dual fluidized bed – mixing and char properties, in: 14th International Conference on Circulating Fluidized Bed Technology, Taiyuan, China, 2024: pp. 409–414.

[150] E. Sette, T. Berdugo Vilches, D. Pallarès, F. Johnsson, Measuring fuel mixing under industrial fluidized-bed conditions – A camera-probe based fuel tracking system, Appl Energy 163 (2016) 304–312. https://doi.org/https://doi.org/10.1016/j.apenergy.2015.11.024.

Nomenclature

A	Cross-sectional area	[m^2]
Ar	Archimedes number	[-]
a, b	Geometrical parameters, as defined by the Kozicki et al. model; see **Table 2-1**.	[-]
C	Geometrical constant	[-]
C_D	Drag coefficient	[-]
C_i	Concentration	[kg/m^3]
C_p	Specific heat capacity	[kJ/(kg·K)]
C_W, C_{H_b}	Geometrical parameters, as defined by the proposed rheological model	[-]
D	Dispersion coefficient	[m^2/s]
D_b	Equivalent bed diameter	[m]
D_h	Hydraulic diameter	[m]
d_p	Mean particle diameter Also denoted as d_s in some instances.	[m]
E	Energy flux	[W]
$E(t)$	Exit age distribution	[-]
e	Coefficient of restitution	[-]
F	Particle force Note: Superscripts B and D denote the buoyancy and drag components, respectively; see **Table 2-4**.	[kg·m/s^2]
FN	Fluidization number, u_0/u_{mf}	[-]
Fr	Froude number	[-]
$\bar{f}_{region}$	Fraction of particles in the specified region (either "dense" or "splash")	[-]
f_F	Fanning friction factor	[-]
G_s	Solids' circulation rate	[kg/(m^2·s)]
g	Gravity constant, 9.81	[m/s^2]
g_0	Radial distribution function	[-]
H	Bed height Note: The "b" in the subscript denotes the "expanded" bed height; see Eq.[8].	[m]
I	Inertial number	[-]
I_0	Constant, $\mu(I)$ constitutive law	[-]
I_{2D}	2nd invariant of the deviator of the rate of strain tensor	[s^{-2}]
i_d	Dead zone index	[-]

K	Flow consistency index constant; see **Table 2-1**.	[Pa·s$^{n^*}$]
k^*	Flow consistency index	[Pa·s$^{n^*}$]
L	Length	[m]
m	Mass	[kg]
N_{CSTR}	Number of reactors in the tank-in-series component of the compartment model	[-]
n^*	Flow behaviour index	[-]
P	Pressure	[Pa]
ΔP	Pressure drop	[Pa]
P_p	Particle pressure	[Pa]
PSD	Particle size distribution	[-]
Q	Volumetric flowrate	[m^3/s]
Re	Reynolds number Note: An asterisk in the superscript denotes a "generalized" Reynolds number; see **Table 2-1**.	[-]
T	Temperature	[K]
ΔT	Temperature difference	[K]
t	Time	[s]
u	Velocity	[m/s]
u_0	Fluidization velocity	[m/s]
u_{mf}	Minimum fluidization velocity	[m/s]
V	Volume	[m^3]
W	Channel width	[m]
x, y, z	Cartesian coordinate system axes: x/z lie in the horizontal plane, y is vertical	[m]
Greek letters:		
β	Geometrical parameter, as defined by the Delplace-Leuliet model; see **Table 2-1**.	[-]
β_{gs}	Inter-phase momentum exchange coefficient	[kg/(m^3·s)]
γ	Isentropic expansion factor	[-]
γ_{θ_s}	Granular collision energy dissipation	[kg/(m·s^3)]
$\dot{\gamma}_a$	Apparent shear rate	[s^{-1}]
$\dot{\gamma}_w$	Wall shear rate	[s^{-1}]
ε	Volume fraction	[-]
η	Solids conveying efficiency	[-]
θ_s	Granular temperature	[m^2/s^2]
κ_{θ_s}	Granular energy conductivity	[kg/(m·s)]
λ	Effective thermal tracing conductivity	[W/(m·K)]

μ	Viscosity Note: Superscripts c, f, and k denote the collisional, frictional, and kinetic parts, respectively, for solids shear viscosity; see **Table 2-3**.	[kg/(m·s)]
$\mu(I)$	Effective friction coefficient	[-]
μ_2	Friction coefficient at high inertial numbers, $\mu(I)$ constitutive law	[-]
μ_S	Static friction coefficient, $\mu(I)$ constitutive law	[-]
ξ	Bulk viscosity	[kg/(m·s)]
ρ	Density	[kg/m^3]
τ	Mean residence time	[s]
$\bar{\bar{\tau}}$	Stress tensor	[Pa]
τ_w	Wall shear stress	[Pa]
φ	Particle sphericity	[-]
φ_f	Angle of internal friction	[-]
ω	Geometrical parameter, as defined by the modified Kostic-Hartnett model; see **Table 2-1**.	[-]
Subscripts:		
$CSTR$	Continuous stirred tank reactor	
CZ	Conveying zone	
$fluid$	Fluidized state	
g	Gas phase	
lp	Lagrangian particle	
MZ	Measuring zone	
pf	Pseudo-fluid	
PFR	Plug flow reactor	
s	Solid phase	
TZ	Transport zone	

Appendix A

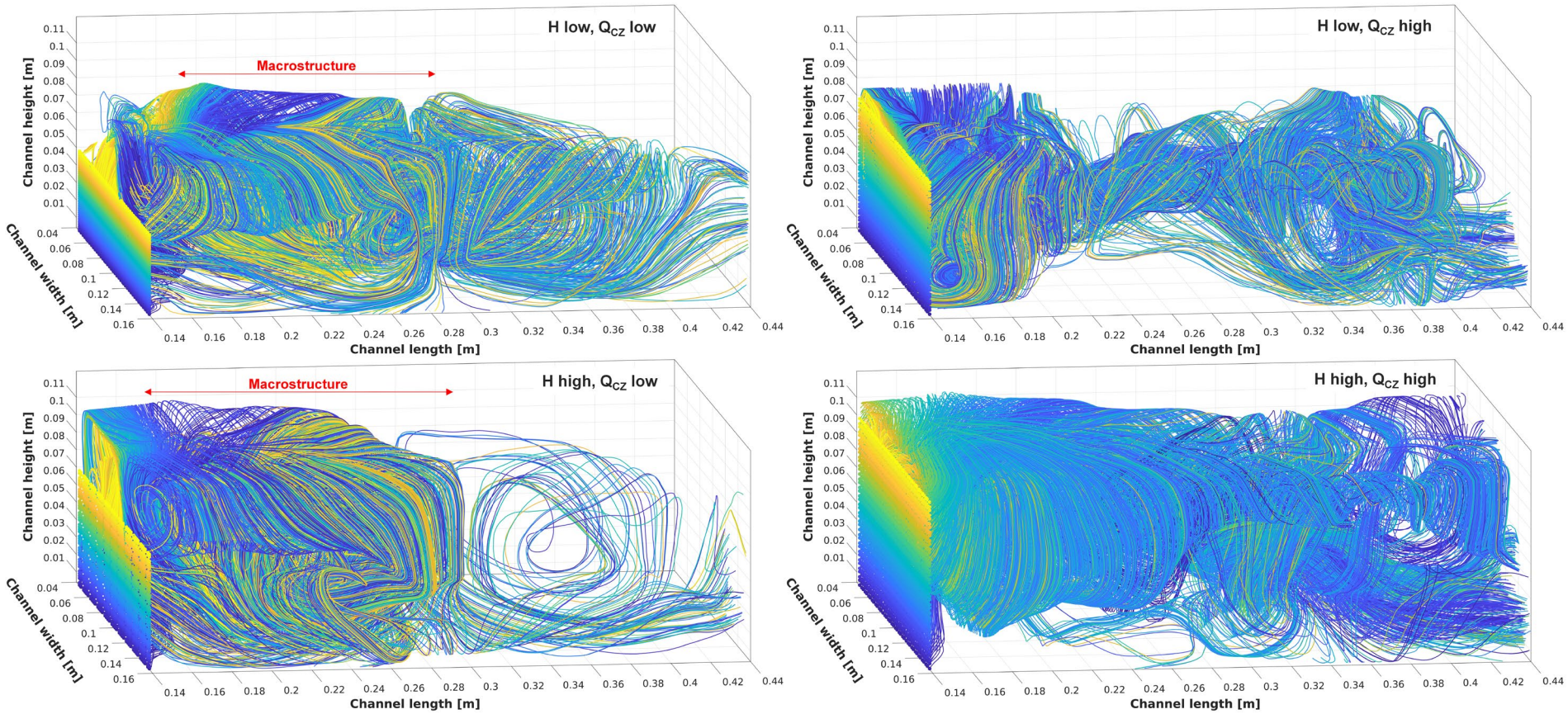

Figure A 1: Particle pathlines in the analysis region for low and high bed heights (H) and volumetric flow rates of air in the conveying zone (Q_{CZ}), at FN_{TZ} of 1.83.

Appendix B

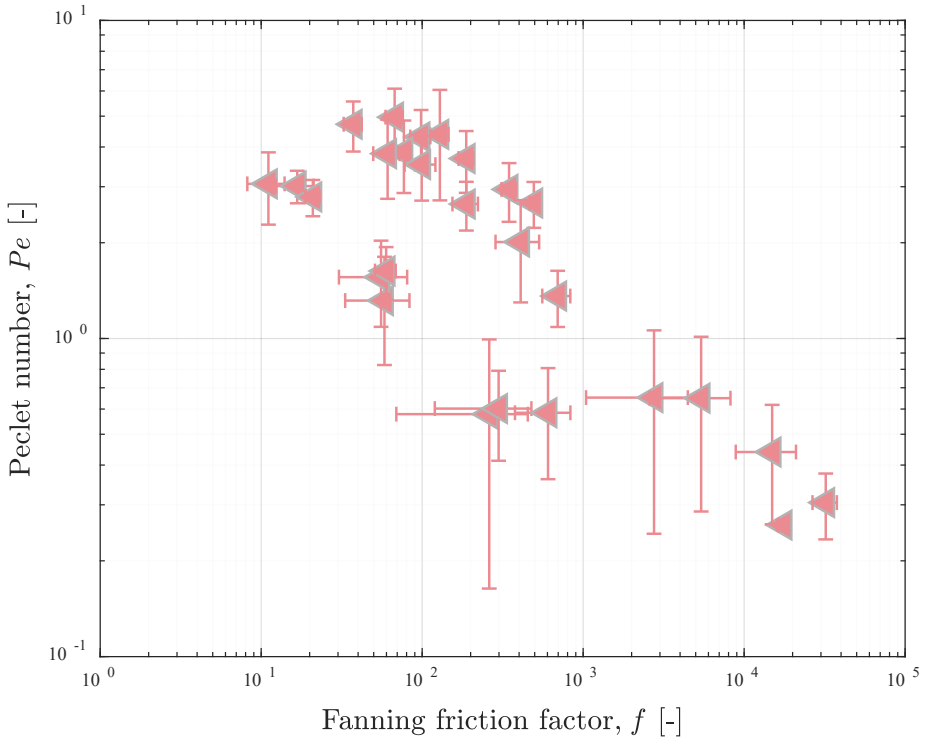

Figure A 2: Péclet number versus Fanning friction factor in the direction of the crossflow for the bed solids suspension studied.

Appendix C

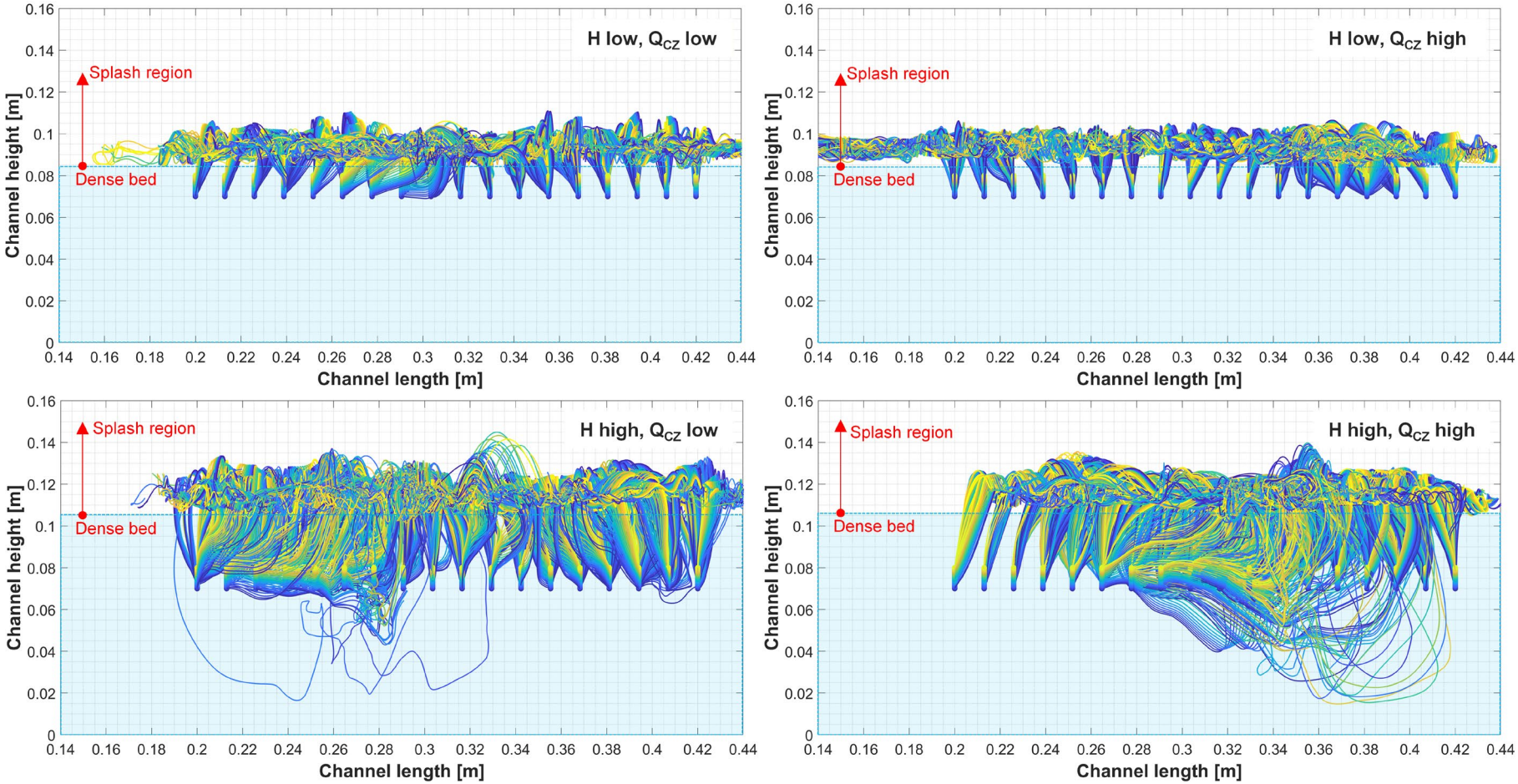

Figure A 3: Lagrangian particle trajectories in the analysis region for low and high bed heights (H) and volumetric flow rates of air in the conveying zone (Q_{CZ}), at FN_{TZ} of 1.83.

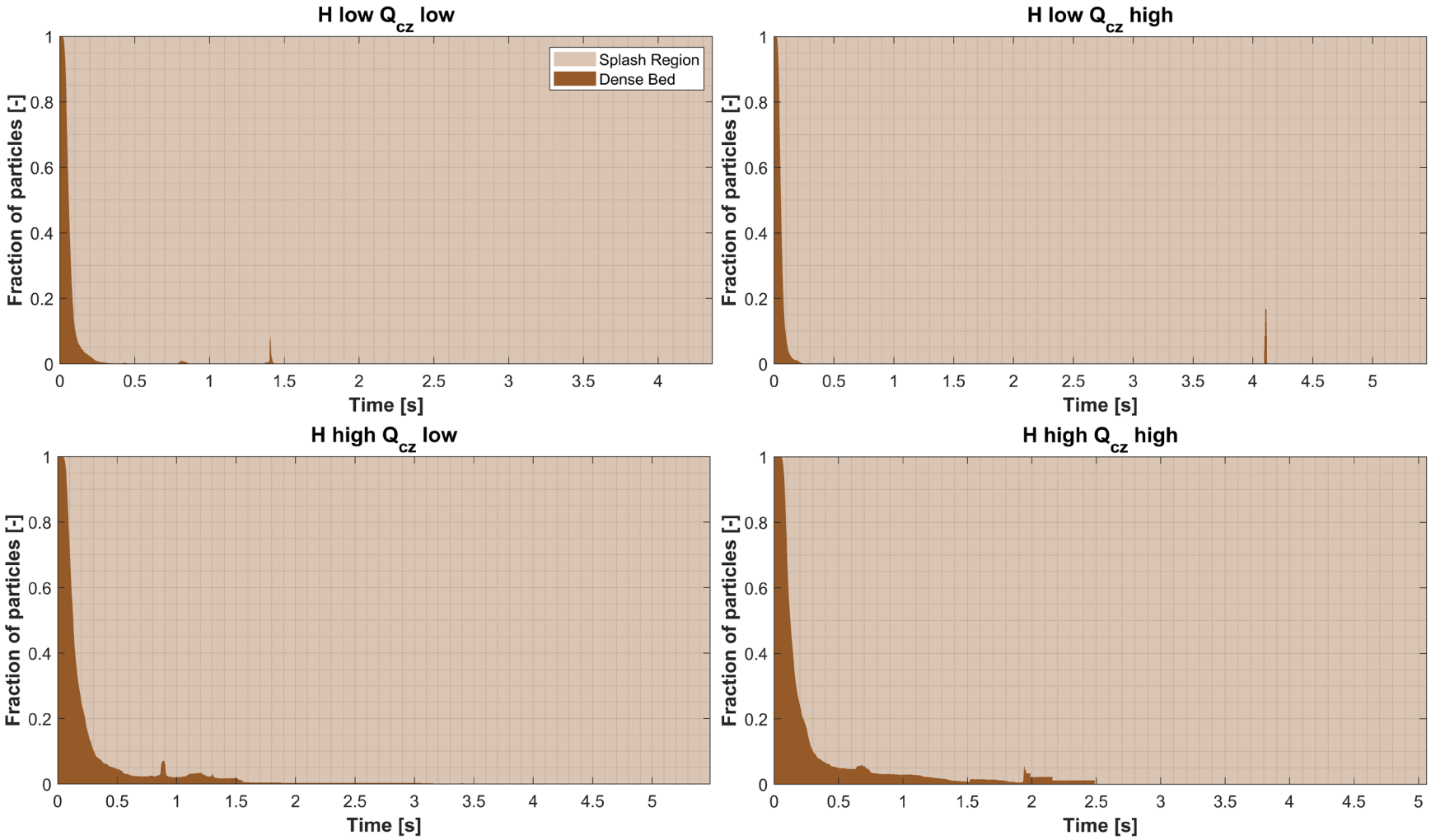

Figure A 4: Temporal evolution of the fraction of lean-phase particles in the dense bed and splash regions, based on particle trajectories obtained from the LPT simulation. Results are shown for low and high bed heights (H) and volumetric flow rates of air in the conveying zone (Q_{CZ}), at FN_{TZ} of 1.83.

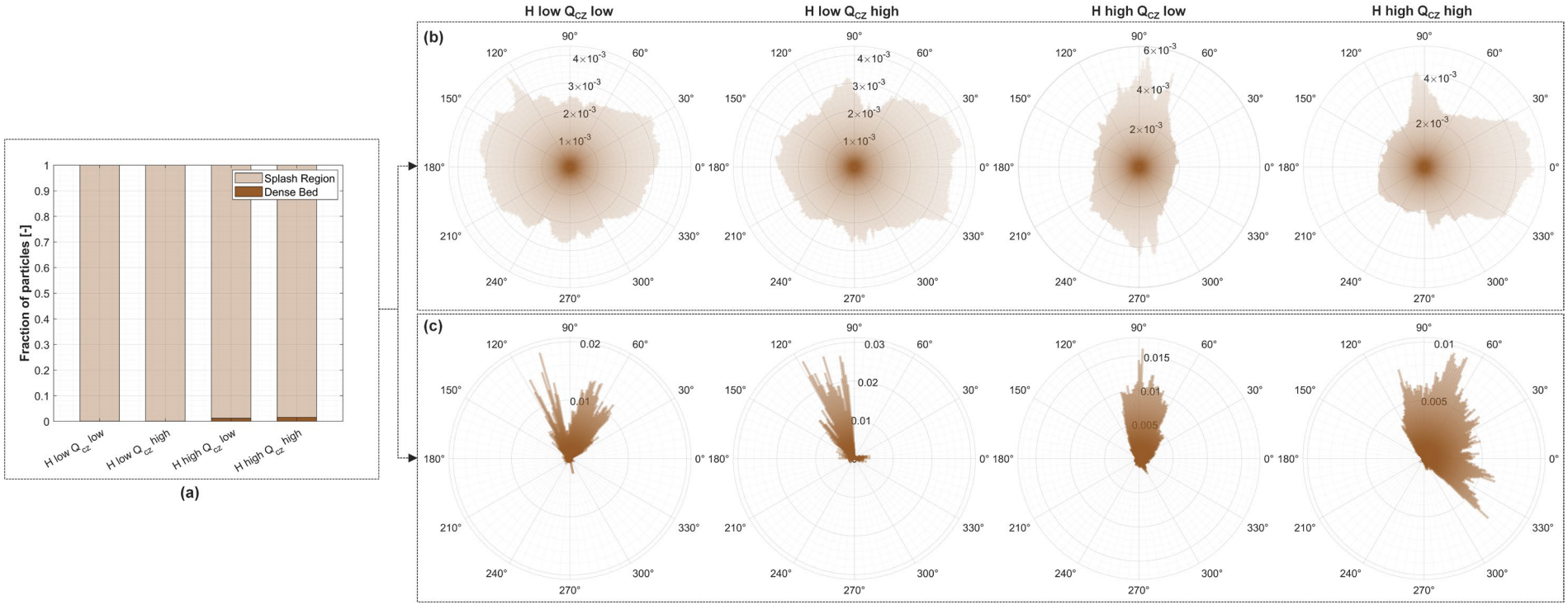

Figure A 5: (a) Time-averaged regional fractions and (b, c) normalized polar spike plots showing the angular distributions of the displacement directions for lean-phase particles in the dense bed and splash regions. Results are shown for low and high bed heights (H) and volumetric flow rates of air in the conveying zone (Q_{CZ}), at FN_{TZ} of 1.83.

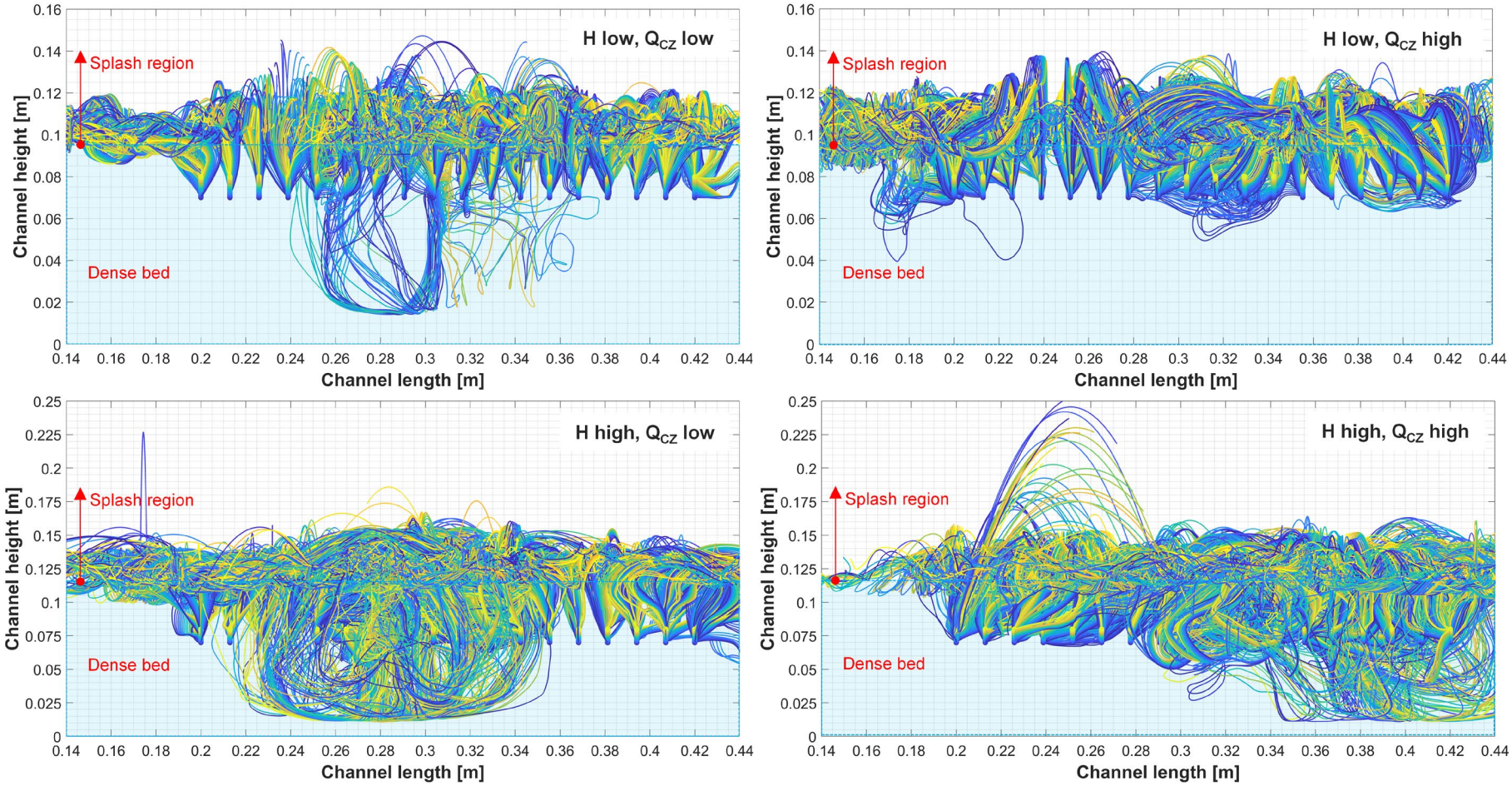

Figure A 6: Lagrangian particle trajectories in the analysis region for low and high bed heights (H) and volumetric flow rates of air in the conveying zone (Q_{CZ}), at FN_{TZ} of 3.

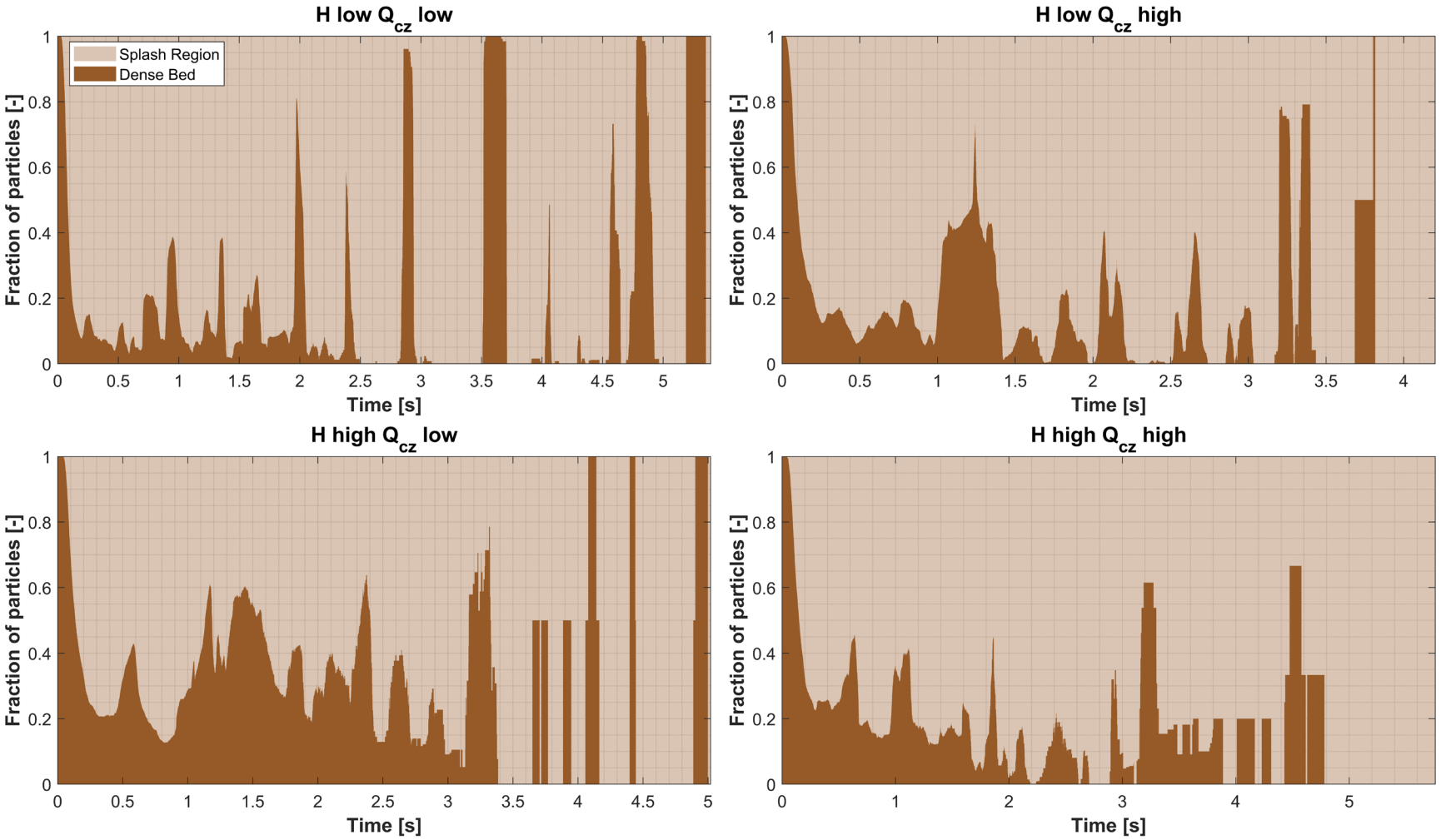

Figure A 7: Temporal evolution of the fraction of lean-phase particles in the dense bed and splash regions, based on particle trajectories obtained from the LPT simulation. Results are shown for low and high bed heights (H) and volumetric flow rates of air in the conveying zone (Q_{CZ}), at FN_{TZ} of 3.

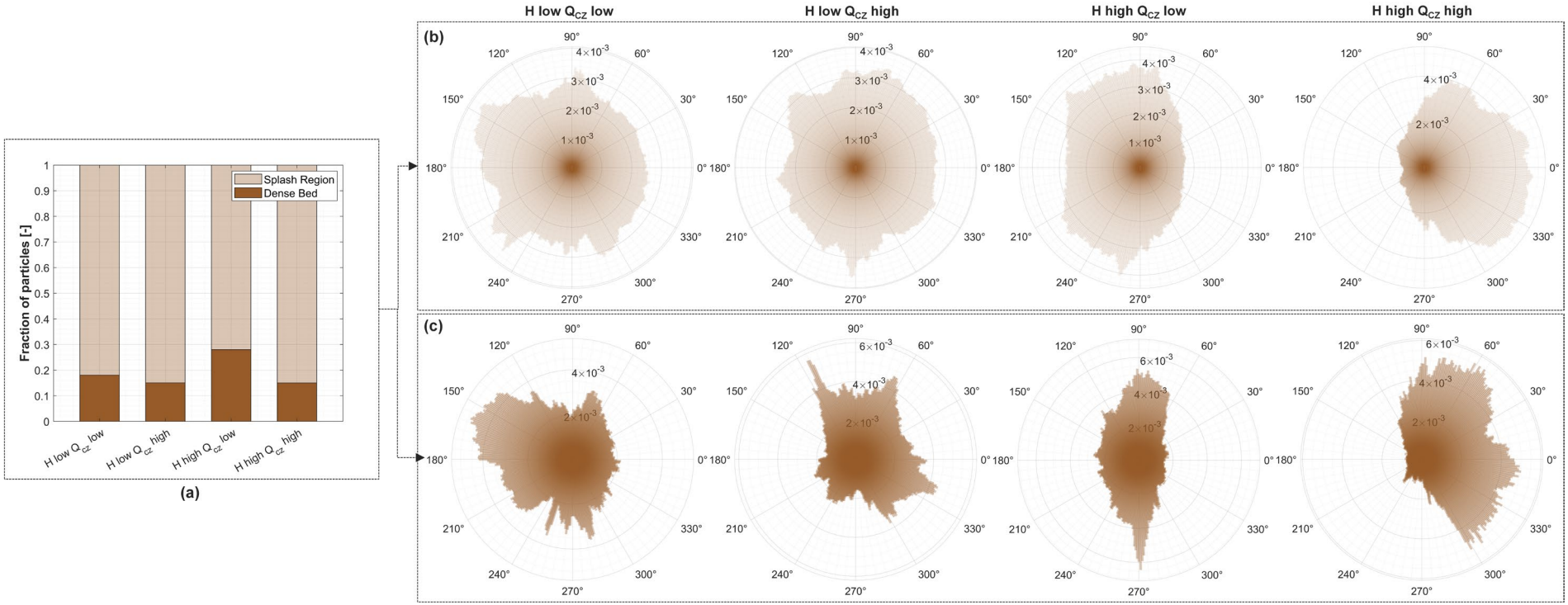

Figure A 8: (a) Time-averaged regional fractions and (b, c) normalized polar spike plots showing the angular distributions of displacement directions for lean-phase particles in the dense bed and splash regions. Results are shown for low and high bed heights (H) and volumetric flow rates of air in the conveying zone (Q_{CZ}), at FN_{TZ} of 3.

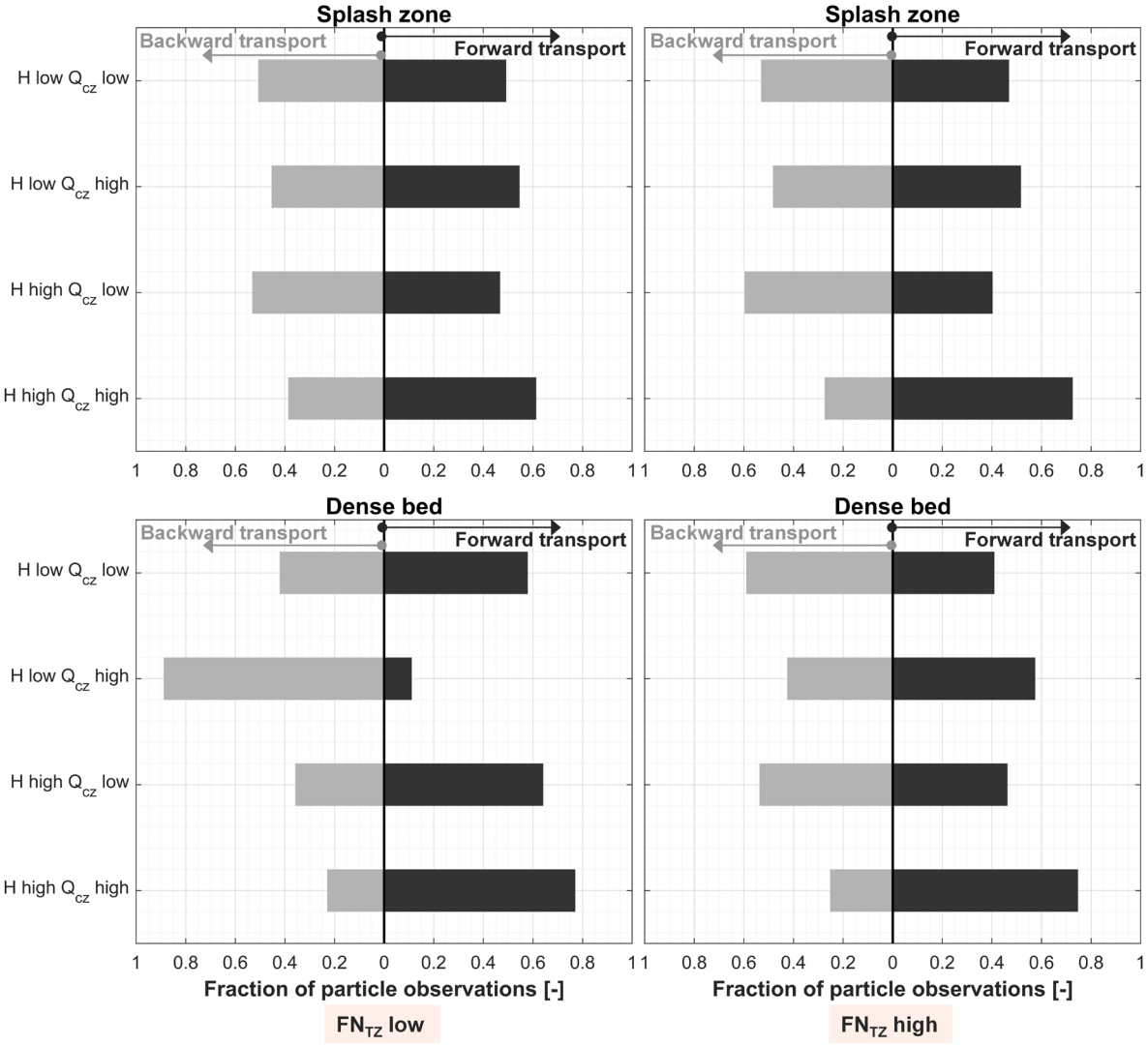

Figure A 9: Fractions of lean-phase particle observations classified as moving forwards (dark bars) and backwards (light bars) in the splash region and dense bed, under varying operating conditions.

The mean velocity in the streamwise (x) direction and the fractional sample count were determined separately for the splash (light-brown) and dense bed (dark-brown) regions. Results are shown in **Figure A 10** for a range of operating conditions at fixed bed height (H) and conveying zone velocity (Q_{CZ}), at two fluidization levels: FN_{TZ} of 1.83 (top panel) and FN_{TZ} of 3 (bottom panel). Regional contributions to net transport were calculated by summing all the x-velocity observations within each region and normalizing with the combined sum from both areas, thus quantifying the proportional influence of each region on the overall convective transport.

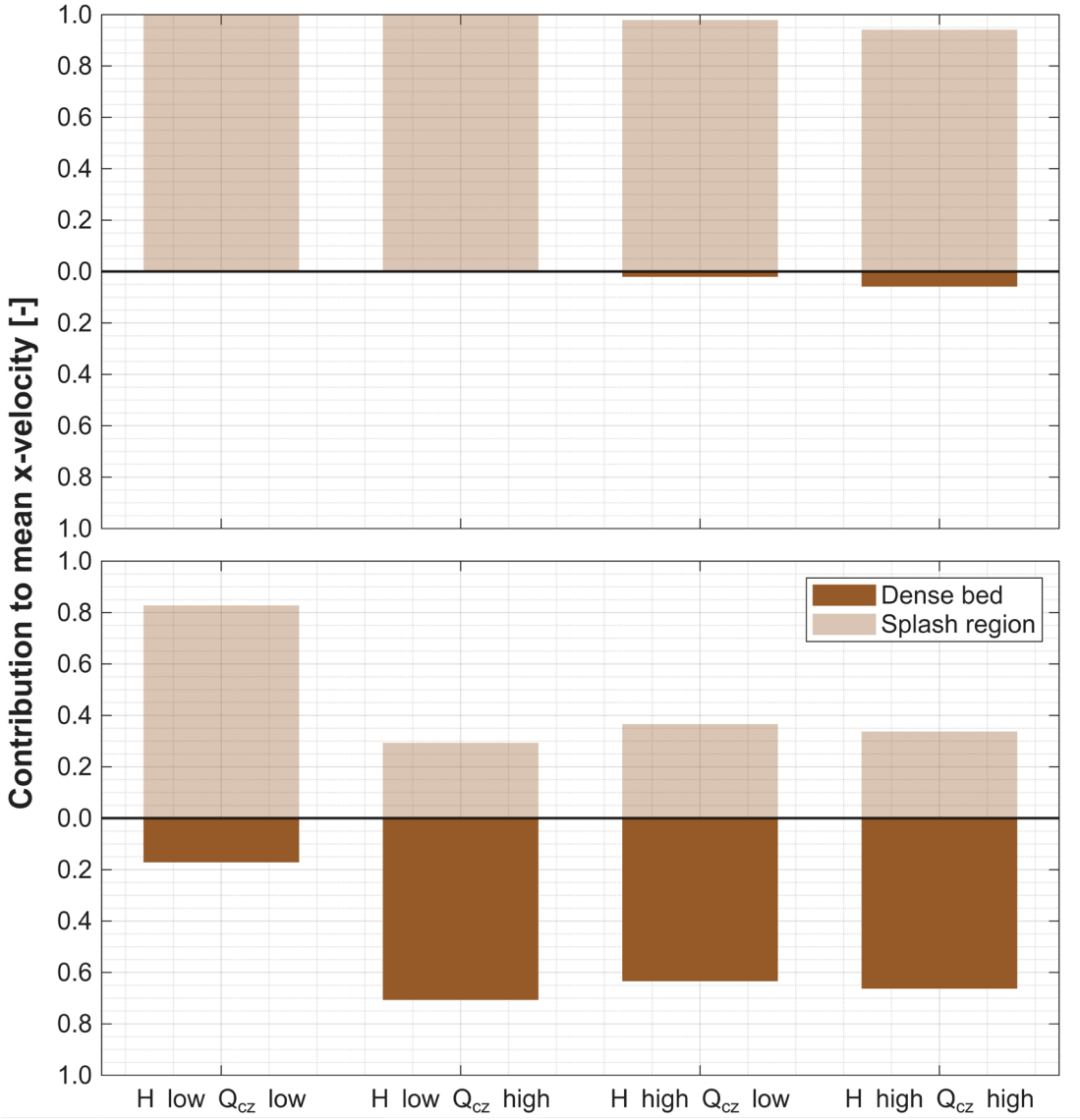

Figure A 10: Fractional sample counts in the splash (light-brown) and dense bed (dark-brown) regions for low and high bed heights and air-conveying zone velocities (Q_{CZ}), at two fluidization levels (FN_{TZ} of 1.83, top; FN_{TZ} of 3, bottom).

Appendix D

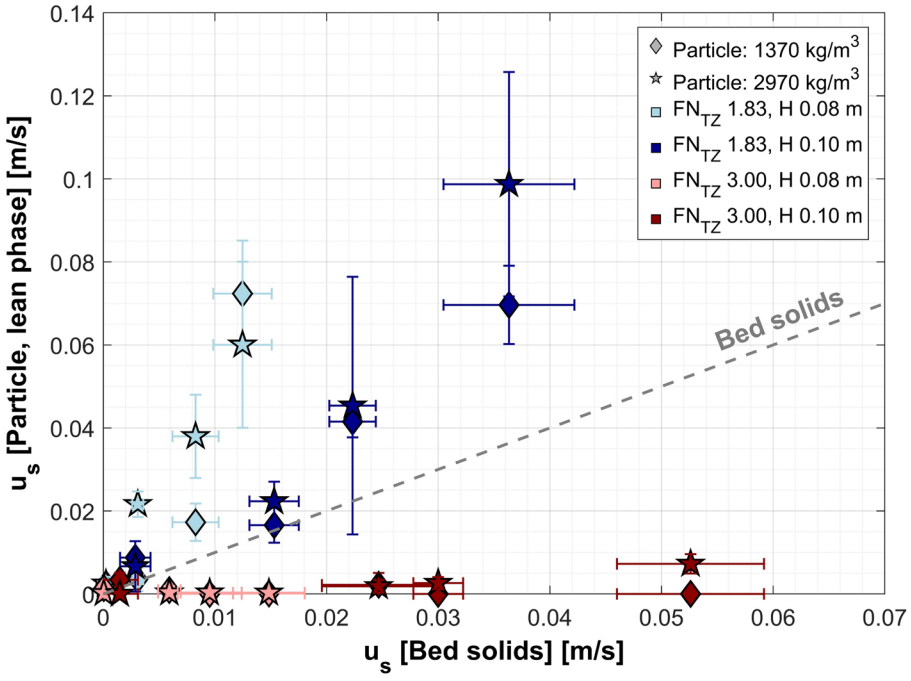

(a)

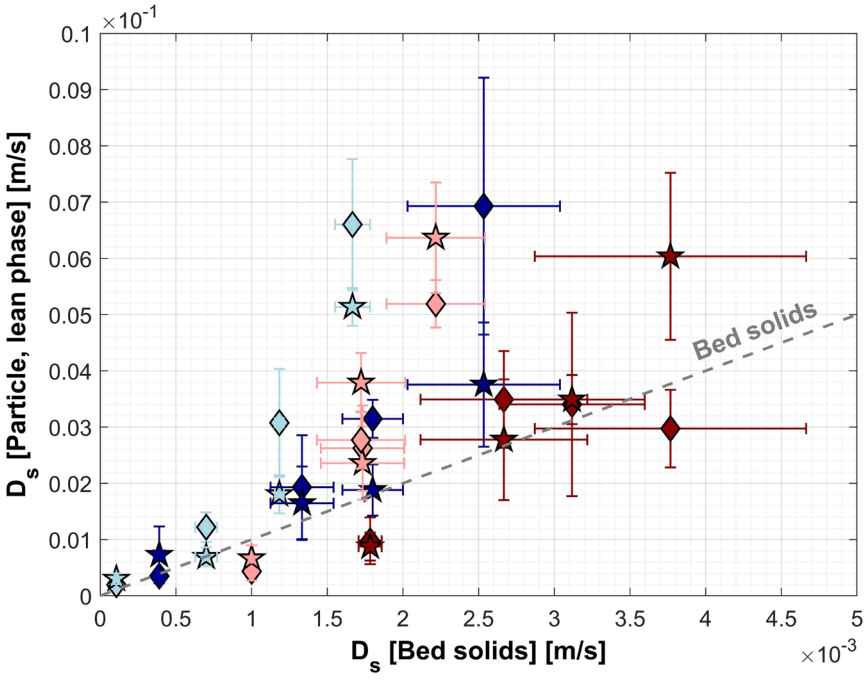

(b)

Figure A 11: Comparison of lean-phase and bulk-phase solids in relation to: (a) solids velocity; and (b) dispersion coefficient, both as functions of the corresponding bed solids parameter (*x*-axis). The dashed gray line represents the reference value for bed solids.

Appendix E

For the purpose of comparison, hot, large-scale experimental data from the dual fluidized bed (DFB) system at Chalmers University were considered (described by Guío-Pérez et al. [149]). This facility consists of a retrofitted 12-MW circulating fluidized bed (CFB) combustor connected to a 2–4-MW bubbling fluidized bed (BFB) pyrolyzer, in which indirect heating is achieved via external circulation of hot bed material from the CFB furnace. Only the BFB pyrolysis unit—where a solids crossflow is established—is considered for comparison. **Table A 1** lists the key operating conditions, geometric parameters, and material properties for both the Chalmers BFB module and the corresponding up-scaled values for the cold-scale unit used in this study (length-scaling factor of 0.12).

Table A 1: Summary of the main parameters for the industrial-scale fluidized bed and up-scaled cold-flow model ($[L]$=0.12).

Parameter	Unit	Cold-flow model	Cold-flow model (up-scaled)	Hot-scale fluidized bed
Cross-sectional area	m^2	0.11×1.24	0.92×10.35	1.44
Bed height	m	0.08–0.10	0.67–0.83	0.40
Temperature	℃	20	800	830
Fluidization velocity	[m/s]	0.14–0.23	0.39–0.65	0.097–0.155
Fluidization number	-	1.83–3.00	1.83–3.00	1.93–3.09
Fluidization medium	-	Air	Air	Steam
Bed material	-	Bronze	Silica sand	Silica sand
Mean particle size, bed material	μm	125	950	270
Particle density, bed material	kg/m^3	8,770	2,650	2,655
Particle size, fuel particle	mm	Ø2×3	Ø20×30	Ø4.15×10.95* Ø6×16.5**
Particle density, fuel particle	kg/m^3	1,370* 2,970**	415* 897.50**	654.5* 1,090.66**

* Devolatilized biomass
** Fresh biomass

Bed material was circulated in the BFB pyrolyzer such that solids entered at one corner of the reactor and exited through an overflow baffle at the opposite end of the unit, establishing a crossflow of solids over the bed. Batches of woody biomass pellets (85–130 g) were introduced for each run, with 5–6 repetitions performed for each combination of bed solids crossflow rate (0.004 and 0.01 m/s) and superficial gas velocity (0.027, 0.036, and 0.044 m/s). Fuel mixing was characterized by tracking pellet motion at the bed surface using a non-intrusive camera probe positioned above the bed, enabling time-resolved video capture of a good part of the bed surface [149,150]. Digital image analysis was applied to the video frames to segment and track the positions of individual biomass particles over time, using centroid detection and linking positions between consecutive frames, as described by Sette et al. [150].

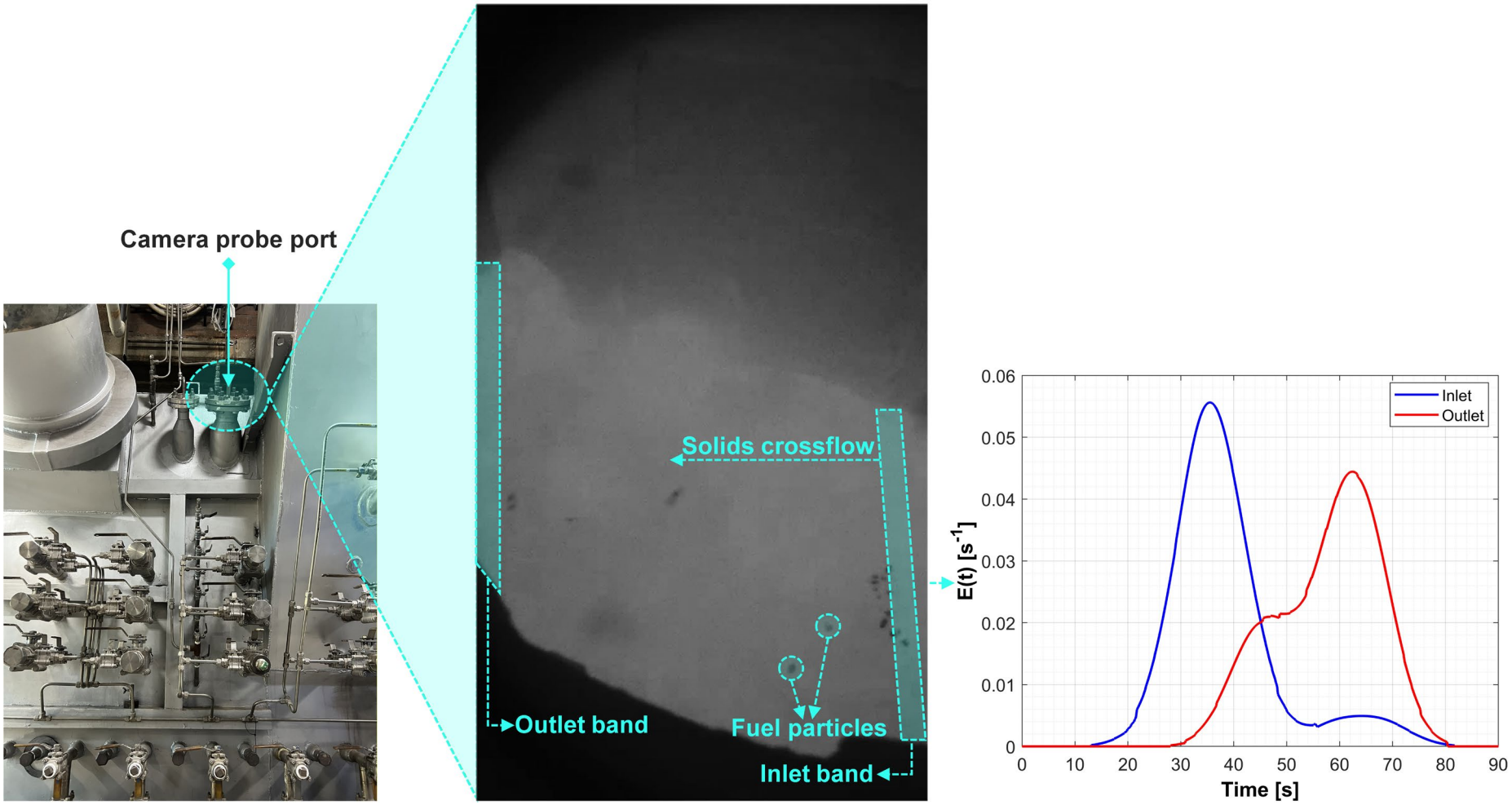

Figure A 12: *Left:* **Schematic showing the camera probe position within the retrofitted 2–4-MW BFB module.** *Center:* **Representative video frame from the digital image analysis, indicating the direction of the bulk-solids crossflow alongside the marked inlet/outlet bands.** *Right:* **Residence time distributions for observed fuel particles at the inlet and outlet bands, derived from image-based tracking.**

Horizontal dispersion was quantified from the distribution of particle observations in the inlet and outlet bands (see **Figure A 12**), enabling approximate construction of RTD profiles. Dispersion coefficients were estimated from the RTD data using Einstein's relation, assuming dispersion-dominated transport with negligible net convection [149]. The characteristic length was defined as the distance between the two bands (~1.2 m in this case) [149].

Figure A 13 presents the relationship between the fuel dispersion coefficient and bed solids crossflow, comparing results from the cold-flow model (up-scaled values reported in the figure) with those derived from the hot-scale experiments. In both cases, the data indicate that increasing the solids bed crossflow significantly enhances the fuel dispersion coefficient. The steepest trend is observed in the hot-scale experiment (0.4 m), while less-pronounced slopes of 0.67 m and 0.83 m are seen in the up-scaled cold-flow cases.

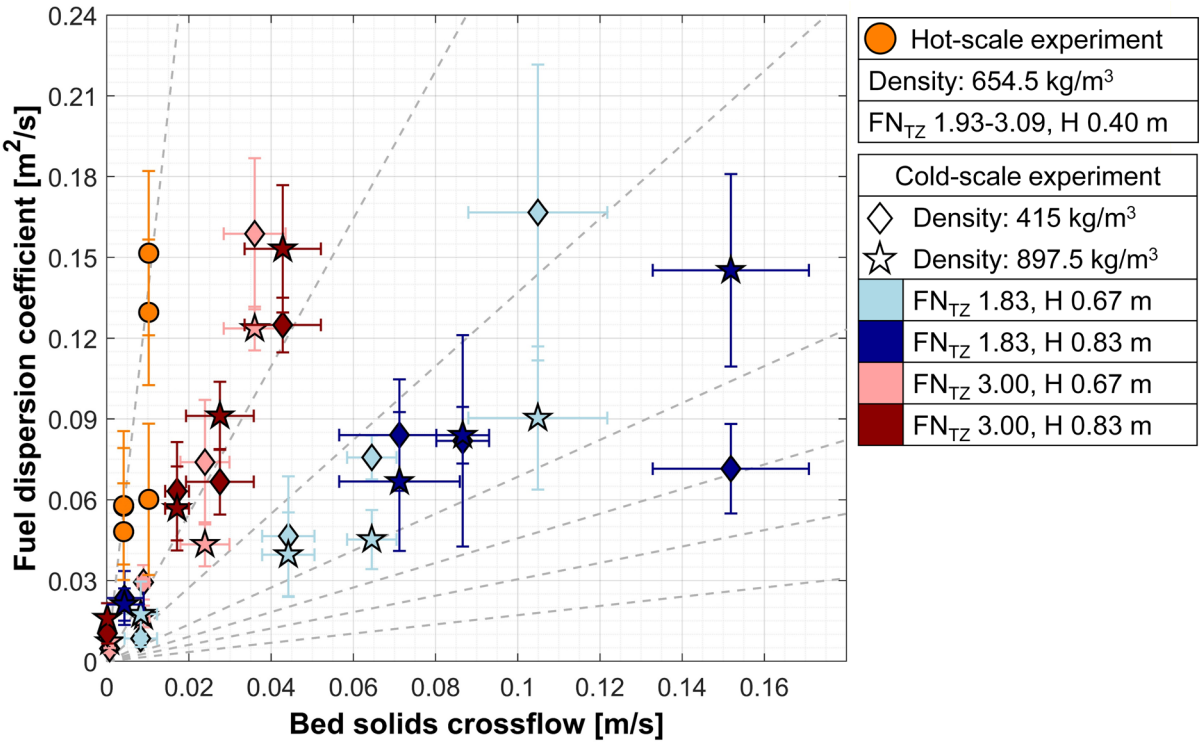

Figure A 13: Comparison of the fuel dispersion coefficients as a function of the bed solids crossflow in the cold-flow (up-scaled) and hot-scale experiments.